The logo features the text "Open Model" in a bold, grey, sans-serif font. The letter "O" is significantly larger and is contained within a blue circle. Above the text, a thin blue arc connects three colored circles: a green one on the left, a yellow one in the middle, and an orange one on the right. The entire graphic is set against a white background with blue curved decorative lines at the top and bottom.

Open Model

ANNA MATVEEVA (SISW)

SIEMENS INDUSTRY SOFTWARE NV, INTERLEUVENLAAN 68, 3001, LEUVEN, BELGIUM

D5.3 - PRELIMINARY USE CASES EXECUTION AND GAP ANALYSIS

DOCUMENT CONTROL

Document Type	Deliverable Report
Status	Final
Version	0.2
Responsible	Anna Matveeva (SISW)
Author(s)	All Success Stories partners, Welchy Leite Cavalcanti (FRAUNHOFER), Susanne Karamanc (FRAUNHOFER) and Anna Matveeva (SISW)
Release Date	Tentative 2023-04-28 (M27)

ABSTRACT

This document covers the final deliverable report *D5.3 – Preliminary use cases execution and gap analysis* with a due date in May 2023 (M27). The aim of this report is to capture the preliminary status of Use Cases execution at the OpenModel partners, identifying the gaps and sketching the path towards Success Story reporting.

More specifically, this deliverable report includes preliminary execution and gap analysis of each Success Story. A clear description of processes, workflows, input/output data provide insight into the required wrappers, that link data stored on the Open Innovation Platform (OIP) to other platform / software tools / marketplaces.

For each Success Story, the identified gaps in models, tools, workflows are summarized, including a root cause and effect analysis and its impact on the workflow's quality assurance. To provide understanding of the OIP platform' elements, this deliverable also includes an evaluation of the calculation capability and ease of use of the Success Stories. A dedicated section of the deliverable summarizes the outcome of each Success Story by comparing it with available experimental data and evaluating the achievement of Key Performance Indicators (KPI). A list of relevant dissemination activities is summarized in the end of the report.

CHANGE HISTORY

Version	Date	Comment
0.1	2023-02-28	First draft
0.2	2023-03-22	Merged with the input from all Success Stories. Submitted to the IP Board
1.0	Tentative 2023-04-28	Final Submission

DISSEMINATION LEVEL

PU	Public	x
PP	Restricted to other programme participants (including the Commission Services)	
RE	Restricted to a group specified by the consortium (including the Commission Services)	
CO	Confidential, only for members of the consortium (including the Commission Services)	

1 TABLE OF CONTENTS

WP5-D5.3: Preliminary Use Cases Execution and Gap Analysis..... 1

Document Control..... 1

Abstract..... 1

Change History 2

Dissemination level 2

List of Figures 5

List of Tables 9

2 Introduction..... 10

 2.1 Overview of the OpenModel project..... 10

 2.2 Overview of the Task 5.3: Preliminary Execution, Validation Methodologies and gap-analysis..... 11

3 Preliminary Use Case Execution 11

 3.1 SUCCESS STORY [1] – SYNAPTIC ELECTRONICS: FROM MATERIALS PROPERTIES TO NEXT-GENERATION MEMORY DEVICES (CNR, AMAT) 12

 3.1.1 Modelling and simulation workflow for off-line execution..... 14

 3.1.2 Input/Output/Backwards processes 19

 3.1.3 Challenges and Gaps analysis..... 21

 3.1.4 Validation against experimental data/ meeting KPI..... 21

 3.1.5 Benefits of OIP platform..... 24

 3.2 SUCCESS STORY [2] - COMPOSITE MANUFACTURING SIMULATION (SISW)..... 24

 3.2.1 Modelling and simulation workflow for off-line execution..... 24

 3.2.2 Input/Output/Backwards processes 29

 3.2.3 Challenges and Gaps analysis..... 32

 3.2.4 Validation against experimental data/ meeting KPI..... 32

 3.2.5 Benefits of OIP platform..... 36

 3.3 SUCCESS STORY [3] – CIVIL ENGINEERING – REINFORCED CONCRETE (HYDRO, SITEF, HEREON) 36

 3.3.1 Modelling and simulation workflow for off-line execution..... 37

3.3.2	Input/Output/Backwards processes	44
3.3.3	Challenges and Gaps analysis.....	45
3.3.4	Validation against experimental data/ meeting KPI.....	45
3.3.5	Benefits of OIP platform.....	45
3.4	SUCCESS STORY [4] – METAL FORMING: RESOURCE EFFICIENT PROCESSING AND MANUFACTURING (HEREON).....	46
3.4.1	Modelling and simulation workflow for off-line execution.....	46
3.4.2	Input/Output/Backwards processes	50
3.4.3	Challenges and Gaps analysis.....	51
3.4.4	Validation against experimental data/ meeting KPI.....	51
3.4.5	Benefits of OIP platform.....	51
3.5	SUCCESS STORY [5] – DIGITAL POWDER TESTING (CMCL).....	52
3.5.1	Modelling and simulation workflow for off-line execution.....	52
3.5.2	Input/Output/Backwards processes	58
3.5.3	Challenges and Gaps analysis.....	60
3.5.4	Validation against experimental data/ meeting KPI.....	60
3.5.5	Benefits of OIP platform.....	68
3.6	SUCCESS STORY [6] – FUEL CELL TECHNOLOGY (DCS, TOYOTA, HEREON)	69
3.6.1	Modelling and simulation workflow for off-line execution.....	70
3.6.2	Input/Output/Backwards processes	77
3.6.3	Challenges and Gaps analysis.....	79
3.6.4	Validation against experimental data/ meeting KPI.....	79
3.6.5	Benefits of OIP platform.....	79
4	Summary and Conclusions	79
5	Dissemination	82
6	Bibliography	84
7	Acknowledgment	86

LIST OF FIGURES

Figure 1: PCM working characteristics: (A) Typical R-T curve of chalcogenide films show that the resistivity of amorphous phase is 5 – 6 orders of magnitude higher than the polycrystalline phases. T_1 and T_2 are the temperatures where the phase transitions take place. (B) I-V curves observed for PCM devices show that in the on state, the device behaves like a non-linear resistor. In the off state, the devices undergo threshold switching at a critical bias (V_t). (C) Ideal thermal profiles generated within the cell during SET and RESET programming. Picture adapted from Ref. G. W. Burr et al. J. Vac. Sci. Technol. B, 28 (2010). 13

Figure 2: Scheme of material-device codesign. Support simulation of new/complex materials (missing parameters, better starting point of parameter optimization, etc.) that enter as input parameter of device modelling. 13

Figure 3: Scheme of REST-API interconnection among constituent codes within Success Story 1 16

Figure 4: AiiDA-quantumespresso plugin used to relax a diamond crystal. The input/output data are represented as nodes in a provenance graph connected by logical links. The code in input defines the executable to be launched. Additional input nodes specify parameters for the calculation. 17

Figure 5: a) Atomic structure of crystalline GST (cubic phase); b) bandstructure; and total (black-line) and projected DOS. 22

Figure 6: a) Formation energy plot as a function of the Fermi level position, for the Te(2) vacancy. X-axis energy scale corresponds to valence band top and conduction band minimum, respectively. b) summary of calculated defect transition states, c) band-alignment of transition state energy within GST bandgap. 23

Figure 7: a) Summary structural and materials (from DFT) parameters of simulated PCM; b) Current-voltage simulated characteristics along with the corresponding experimental data. 23

Figure 8: Schematic overview of the Success Story 2 24

Figure 9: Typical thermoset composite manufacturing steps enabled by simulations: drape, flow, cure 25

Figure 10: (a) Required input for draping simulation: mold geometry, rosette and draping strategy; (b) Schematic representation of the shear angle distortion on a piece of fabric; (c) Visualization of the shear angle distortion in the 60° -ply of a B-Pillar (in red). Ref. [8] 26

Figure 11: Permeability computation workflow 27

Figure 12: Illustration of the workflow for curing simulation and computation of residual stresses/deformations. 29

Figure 13: (a) Laser Doppler Vibrometer setup with a scanning grid mapped on the part ; (b) Different excitation sources and signal types for experimental modal analysis. The best excitation source and signal type highlighted. 33

Figure 14: Frequency response function of LDV vs accelerometers 33

Figure 15: (a) Visualization of the testing scanning grid overlaid with the FEM model; (b) Modal Assurance Criterion (MAC) of Experimental and Simulations results 34

Figure 16: Simulation sequence: draping simulation; mapping of fiber orientations and computation of local permeability tensor, and resin flow simulation. Reproduced from [9]. Reproduced from [8] 35

Figure 17: Time at which the flow front passes through each sensor location (symbols are experimental data; continuous lines are simulation results); on the right bottom corner, a scheme shows the sensor locations. Reproduced from [8]..... 35

Figure 18: Examples of aluminium reinforcements in concrete. Reproduced from [13]..... 37

Figure 19: Example of steel reinforcements corroding in conventional concrete. Reproduced from [13] 37

Figure 20: Example of aluminium reinforcements corroding in conventional concrete Reproduced from [13].. 38

Figure 21: Image of concrete and aluminum interface area. Cracks in the concrete due to sample preparation. Dark grey area close to the aluminum surface indicates a dense barrier formed during the initial curing phase [14]. 39

Figure 22: Different elemental distributions in the concrete-aluminum interface area. Top left: Visible light image of the area. Top Right: Magnesium concentration. Lower Left: Aluminum concentration Lower Right: Calcium concentration [14]. 39

Figure 23: Setup for four-point bending test. 40

Figure 24: Layers present in Micro-scale model 40

Figure 25: Example of aluminum extrusion profiles for reinforcement in concrete..... 41

Figure 26: Flow Diagram of envisioned workflow..... 41

Figure 27: Flow Diagram of current workflow. 42

Figure 28: Modelled tensile yield strength compared between linear regression of a 2nd order polynomial to the ensemble model..... 46

Figure 29: Tensile elongation at break based on ML over the extrusion speed for T=400, Gd=7.28. 47

Figure 30 Map showing the process-property mapping for 1% Gd for compressible elongation. 47

Figure 31: Map showing process parameters for which isotropic behavior (TYS/CYS=1) is predicted by the ML model with $2\sigma < 0.03$ and $TYS/CYS=1\pm 0.025$ 48

Figure 32: Use-case processes overview..... 52

Figure 33: Catalyst powder testing process overview. 53

Figure 34: A schematic diagram for Digital Engineering workflow for IC engine modelling 54

Figure 35: Inputs for the engine modelling, and the corresponding outputs..... 55

Figure 36: Inputs of the engine surrogate model need to cover the range of conditions that would occur during drive cycle testing. 56

Figure 37: Data/model dependency of the workflow. 59

Figure 38: A representative set of 19 operating points on the engine load-speed window. The case ID is presented as the number next to the operating point. The arrows indicate the increment direction of the case ID. 61

Figure 39: Calibrated pressure profiles for 9 pure gasoline load-speed points at 1200 rpm (top), 2000 rpm (mid), 2500 rpm (bottom), and increasing IMEP⁺ (in left to right direction). 61

Figure 40: Experiment vs SRM Engine Suite for NO_x and uHCs. 62

Figure 41: Experiment vs kinetics for TWC conversion at lean condition. 63

Figure 42: Experiment vs kinetics for TWC conversion at stoichiometric condition. 63

Figure 43: Experiment vs kinetics for TWC conversion at rich condition. 63

Figure 44: Conversion of various TWC samples at lean condition, literature experimental condition [2]. 64

Figure 45: Conversion of various TWC samples at stoichiometric condition, literature experimental condition [2]. 64

Figure 46: Conversion of various TWC samples at rich condition, literature experimental condition [2]. 64

Figure 47: Inputs of the TWC steady-state testing generated by the engine surrogate model. 65

Figure 48: results of TWC testing with engine test bed. 65

Figure 49: Simulated TWC temperature profile during drive cycle testing. 66

Figure 50: Cumulative emissions from TWC sample A during drive cycle test. Emissions are normalised by that of the reference catalyst. 67

Figure 51: Smoothed “instantaneous” emissions from TWC sample B during drive cycle test. Emissions are normalised by the maximum values of “instantaneous” emission of the reference catalyst. 67

Figure 52: Total emissions from TWC samples during WLTC. 68

Figure 53: Schematic of a fuel cell. 69

Figure 54: Example of a DEM-generated random particle packing and a CFD mesh generated from a region of the particle arrangement. 71

Figure 55: (a) Example of electric conductivity DEM simulation and (b) multiphase CFD simulation of water and air through porous media. 71

Figure 56: Fuel cell model schematic sum up. 72

Figure 57: Gas channel and macroporous substrate simulation. Left: Temperature field for particle and fluid. Right: Velocity magnitude contours on the middle plane of the simulation domain. 73

Figure 58: Microporous layer simulation. 73

Figure 59: example of calibration of electrical conductivity. 74

Figure 60: Comparison of the three methods. Left: Simulation domain used in the comparison. Green square: domain used to average the results. Red squares: RVE distribution along the domain. 75

Figure 61: Example of application. Left: particle mesh with arrow indicating the inlet for steam and oxygen. .. 76

Figure 62: Comparison of oxygen flux at the upper boundary of the domain. The three cases differ for the microporous layer porosity. 77

LIST OF TABLES

Table 1: Summary of input/output data for Success Story 1 19

Table 2: Summary of input/output data for Success Story 2 30

Table 3: Concrete formulation as used in this application. Reproduced from [13] 38

Table 4: Summary of input/output data for Success Story 3 44

Table 5: Summary of input/output data for Success Story 4 50

Table 6: Summary of input/output data for Success Story 6 78

Table 7 Summary of all Success Stories 80

Table 8 Summary of dissemination activities..... 82

D5.3 - PRELIMINARY USE CASES EXECUTION AND GAP ANALYSIS REPORT

2 INTRODUCTION

2.1 OVERVIEW OF THE OPENMODEL PROJECT

OpenModel will provide an Open Innovation Platform (OIP) for Integrated Materials Modelling, which offers 5 main ingredients: 1) EMMO based ontology extensions as basis for all developments, 2) An Interoperability layer, 3) An Open Simulation Platform based on standardised interfaces and semantic common application programming interfaces (API), to enable integration of third party physics based modelling codes, 4) Smart workflow builders that respond to semantic information and requirements and creates on the fly advanced workflows taking into account Key Business and Technical Performance Indicators (KPI) utilising the semantic power embedded in the platform, and 5) workflow executors and curators able to perform and manage the results making it readily and transparently available for further control and processing by other platforms.

OpenModel targets multiple use cases and materials with their processing in the fields of environment, aviation, and automotive industry, yet OpenModel's scope is generic and can thus address all materials modelling, processing, and characterization fields. OpenModel aims to become the platform for materials modelling Services in Europe.

Six Success Stories have been considered, covering a wide range of applications, and reflecting the generic scope of the project. These Success Stories include:

- Success Story [1] – Synaptic Electronics: From Materials Properties to Next-Generation Memory Devices (CNR, AMAT)
- Success Story [2] - Composite Manufacturing Simulation (SISW)
- Success Story [3] – Civil Engineering – Reinforced Concrete (HYDRO, SINTEF, HEREON)
- Success Story [4] – Metal Forming: Resource Efficient Processing and Manufacturing (HEREON)
- Success Story [5] – Digital Powder Testing (CMCL)
- Success Story [6] – Fuel Cell Technology (DCS, TOYOTA, HEREON)

The Success Stories execution and the demonstration of the OpenModel platform effectiveness in addressing industrial challenges is the focus of the WP5.

2.2 OVERVIEW OF THE TASK 5.3: PRELIMINARY EXECUTION, VALIDATION METHODOLOGIES AND GAP-ANALYSIS

This deliverable is part of the Task 5.3 which aims at assessing the required data flows between the OIP and the consumer through the preliminary execution of each Success Story. This task will provide insight in the required wrappers that link data stored on the OIP to usage on other platforms, including academic and commercial environments (as listed in Task 3.2) and marketplaces (e.g. VIMMP, MarketPlace, Market 4.0, etc.). For these tools and platforms, interface wrappers and plugins will be developed in Task 3.2. In this WP5, they will be further augmented based on the business case requirements of industrial end users and other stakeholders. More specifically, it will be ensured that the required data, models, workflow selection, etc. are in place for each specific Success Story. The preliminary execution will also help in finding gaps in current workflows that can be subsequently resolved to further improve their industrial applicability. If gaps are identified, a root cause and effect analysis can be considered, to analyse any failures or near-misses that occur in the preliminary execution and avoid that they will occur in Task 5.4. The elements of the platform, including calculation capability and ease of use, can be exhibited here to help the evaluation. For each Success Story, attention will be paid to meeting the KPIs and possibly validating the Success Story outcome based on experimental data, as this will increase the confidence in the outcome of the Success Story. SISW and other involved end users will carry out preliminary executions on the use cases to set a performance benchmark and to ensure all aspects of the OIP such as the required data, models and workflow are covered in each Success Story. Some key features of the OIP will be explained, such as the validation methodologies to evaluate the state of the platform. The deliverable will establish the gaps in the current modelling workflows to carry out further improvements. The deliverable includes on the one hand an overview of requirements for the wrappers developed in WP3 and, on the other hand, an execution status overview of all the Success Stories. As such, the deliverable represents a solid foundation for future dissemination efforts in the frame of WP6.

3 PRELIMINARY USE CASE EXECUTION

The preliminary execution of Success Stories refers to the initial steps taken to ensure that the cases are valid and feasible. It is an important step in the development of the OpenModel platform, as it helps to ensure that it can address a wide range of industrial challenges, meeting the requirements.

This section includes contributions from all partners involved in Success Story execution in the frame of the OpenModel project. Each section starts with a general description, identification of the desired outcomes and objectives of the Success Story and then is split into subsections:

1. Processes and workflows for off-line execution
 - Description of the flow of events, that take place to achieve the objectives
 - Summary of software, toolkits, models
2. Input/Output/Backwards processes

- Description of the processes starting from the output back to the input, that provide a high level guidelines for the OIP OpenModel
- 3. Gaps analysis
 - Description of the identified gaps in models/tools/workflows
- 4. Validation against experimental data/ meeting KPI
 - Validation of the Success Story to ensure that it is feasible and meets the requirements
- 5. Benefits of OpenModel platform
 - Description of the 'ease of use' and calculation capability of the Success Story

3.1 SUCCESS STORY [1] – SYNAPTIC ELECTRONICS: FROM MATERIALS PROPERTIES TO NEXT-GENERATION MEMORY DEVICES (CNR, AMAT)

Synaptic electronics for neuromorphic computing and AI development

Artificial intelligence (AI) is the most radical innovation of the last 20 years, becoming *the* game changer in industry, transport, communication, health, and culture as a whole, with an unprecedented impact on economy and society. At the same time, AI has a horrible energy footprint: it has been reported that the energy required for training a neural network involves the emissions of the same amount of carbon dioxide released by five average cars in their lifetime. The bad energy efficiency of AI is mainly due to the digital computers used for training and deploying AI models. Digital computers with the conventional von Neumann architecture are not designed to execute AI codes, generally consisting of deep neural networks (DNNs) handling large amounts of data (input, weights, activations) to be exchanged between the processing unit and the memory. Recently, in-memory computing (IMC) has been proposed as a more efficient paradigm for DNNs, thanks to the ability to accelerate AI operations within a crosspoint memory array mapping the synaptic weights. Among the novel technologies which are being explored for neuromorphic computing, the class of *emerging memory devices or storage-class memories (SCMs)*, such as the phase-change memory (PCM), the resistive-switching memory (RRAM), and the spin-transfer torque memory (STTRAM), are the most promising. This new class of memory technology has performance characteristics that fall between DRAM and flash characteristics and bridges the latency gap between server storage and external storage. In particular, the RRAM device, also known as memristor, has been deeply investigated for its key characteristics, such as full compatibility with CMOS technology, simple geometry, low-power operations, and scalability beyond the 10 nm node.

Phase Change Memories

In this Success Story we considered the case of PCM memory based on chalcogenide materials, such as $\text{Ge}_2\text{Sb}_2\text{Te}_5$ (GST). PCM is a non-volatile, solid-state memory technology which exploits the large electrical contrast between the highly resistive amorphous and highly conductive crystalline states in so-called phase change materials, usually chalcogenides. The main working steps of PCM (READ, SET, and RESET) are schematized in Figure 1. Experimental data indicate that the electrical performances, the power efficiency, and the endurance of these devices depend critically on the microscopic properties of the active material.

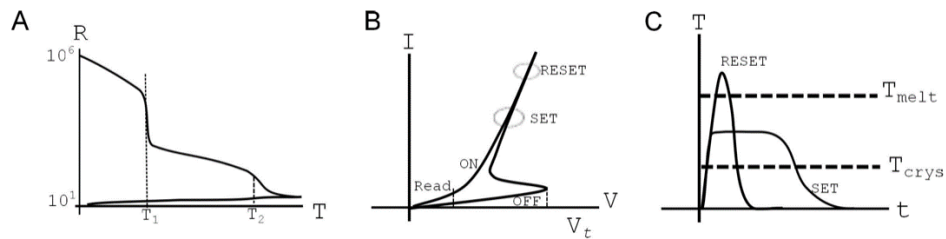


Figure 1: PCM working characteristics: (A) Typical R-T curve of chalcogenide films show that the resistivity of amorphous phase is 5 – 6 orders of magnitude higher than the polycrystalline phases. T_1 and T_2 are the temperatures where the phase transitions take place. (B) I-V curves observed for PCM devices show that in the on state, the device behaves like a non-linear resistor. In the off state, the devices undergo threshold switching at a critical bias (V_t). (C) Ideal thermal profiles generated within the cell during SET and RESET programming. Picture adapted from Ref. G. W. Burr et al. *J. Vac. Sci. Technol. B*, 28 (2010).

Material-device codesign approach

The development of these new nanodevices (not based on standard CMOS technology) requires the deep understanding of the interplay between the parameters that characterize the not standard materials (e.g. structure, composition, doping, stability, electrical and thermal response) and the influence they have on the device (e.g. data retention, power consumption, interconnection, switching time). Yet this is hard to determine, especially from experimental side. *The aim of this Success Story is to provide a solid, interoperable and industry-oriented software protocol for an easier exploration of the material workspace from an electronic device perspective.* We propose a material-device codesign approach that fosters the optimization of PCM capabilities starting from the material properties and fabrication process effects. A critical aspect in modelling PCM devices is the capability of treating/controlling/understanding systems with a high degree of *structural disorder*, including, amorphous states, defects, traps, impurities and boundaries. This calls for a joint materials-device codesign, able to unravel the interplay between material traps/local-structures and the influence they have on the electrical properties of the device. In the specific case of Success Story 1 we aim to study the effect of Ge-stoichiometry on the crystalline-amorphous phase transition temperature on the electrical response of chalcogenide-based PCMs.

For this reason, we setup a multi-physics, multi-model, multi-equation, hierarchical model that combines microscopic characterization of materials, based on quantum mechanical first principles calculations, and device modelling, based on advanced continuum electrical models. The conceptual scheme at basis of Success Story 1 is summarized in Figure 2.

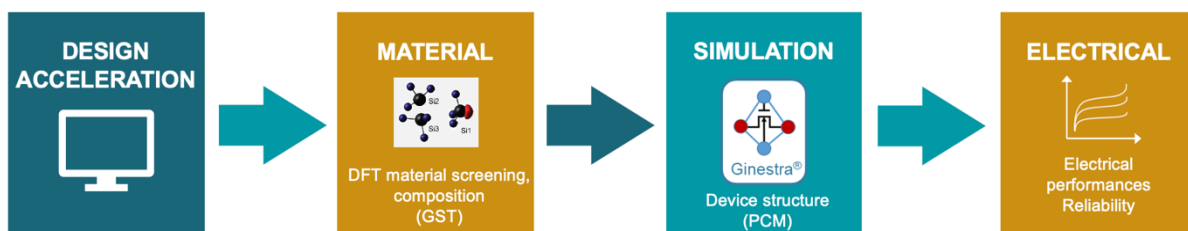


Figure 2: Scheme of material-device codesign. Support simulation of new/complex materials (missing parameters, better starting point of parameter optimization, etc.) that enter as input parameter of device modelling.

3.1.1 MODELLING AND SIMULATION WORKFLOW FOR OFF-LINE EXECUTION

Components and interconnections

The off-line execution of Success Story 1 (SS1) required the re-use and the integration of existing state-of-the-art codes for the quantum mechanical materials modelling (namely QuantumEspresso suite) and for device modelling (Ginestra®) through the AiiDA infrastructure. This implied: i) the upscaling of the initial codes and the development of new features for the description of complex physical properties such as the defect formation energy and thermodynamics in the materials codes, as well as the implementation of the PCM module in Ginestra®; ii) the development and the test of simulation protocols and implementation of postprocessing tools for the analysis of highly disordered and amorphous systems; iii) the development/optimization of workflows for the preparation/execution of materials simulations and the interoperable interconnection between codes and/or databases.

The principal stand-alone code used in this Success Story are:

- **Quantum Espresso** - Quantum ESPRESSO (QE, www.quantum-espresso.org) is an open-source suite, under a GPL license, for quantum mechanical modelling of solids, interfaces and nanostructures. QE provides ab initio modelling of electronic, optical, and vibrational properties. QE deals with both electrons and atoms model entities. For electron model, QE implements Density Functional Theory (DFT). The Schrodinger equation in the Kohn-Sham approximation is the fundamental model physics equation, used to calculate electron wavefunctions, electron density and total energies. Material relations include local (Hartree) and non-local (exchange-correlation) potential from electron density, pseudopotential for implicit core electrons, Hubbard-like potential for highly correlated electrons. Local, hybrid exchange-correlation functionals, norm-conserving, ultrasoft pseudopotential, and plane-wave basis sets are the main physical quantities implemented for these material relations.
 - *pw.x* is the main DFT engine of QE that implements total-energy-and-forces algorithms to obtain the ground state of the systems under investigation. Within SS1, this code is used to evaluate:
 - total energy (E_T)
 - optimized crystal and atomic structure
 - single particle electron energies
 - Fermi level (E_F)
 - energy band structure and bandgap (E_g)
 - *projwfc.x* is a postprocessing tool that reads the output of *pw.x* and evaluate the total and pseudo-atomic wave-function projected Density of State (DOS)
 - *pp.x* is a postprocessing tool that reads the output of *pw.x* and provides for 3D representation of electronic properties analysis. Within SS1, this code is used to evaluate:
 - single particle charge density
 - inverse participation ration (IPR)
 - electrostatic potential (V_{es})
 - *ph.x* is a major postprocessing code that, starting from the electron density evaluated with *pw.x*, implements the density functional perturbation theory (DFPT) for the evaluation of dielectric and vibrational properties. Within SS1, this code is used to evaluate:
 - zero-frequency dielectric tensor (ϵ_0)
 - phonon band structure.

- **Ginestra**[®] - is a commercial software (property of Applied Material Italia – AMAT, www.appliedmaterials.com/us/en/semiconductor/ginestra-software.html), designed to simulate the electrical characterization measurements performed on semiconductor devices for an easy interpretation of the experimental data and for the prediction of device reliability. The software package relies on a novel material-related microscopic approach for the description of the physical mechanisms governing charge-transport and degradation. Ginestra[®] accounts in a self-consistent fashion for charge trapping and transport, power dissipation, generation diffusion and recombination of defects and mobile ions. For the atomic physical entity Ginestra[®] implements a kinetic MonteCarlo for defects and ion diffusion/recombination at finite temperature. At the device simulation level, the software describes carrier transport across the material stack accounting for drift-diffusion, Fowler-Nordheim (FNT) and direct tunnelling (DT), and the defect-assisted charge transport, dominated by the Trap-Assisted Tunnelling (TAT) mechanisms. The FNT/DT currents from the substrate are calculated by adopting the semi-classical approximation, while the electron FNT/DT current from the metal gate is computed through the Tsu-Esaki formula. The TAT current is calculated by including charge carrier-phonon coupling and lattice relaxation processes that are directly related to the material-specific atomic nature of the defect. Spatial correlation of the defect generation process is also included. Within SS1, Ginestra[®] is used to evaluate:
 - electrical characteristics: I-V, C-V
 - trap band diagrams
 - virtual lab for device characterization
 - reliability and variability analysis.
- AiiDA (www.aidata.net) is the open-source environment that allows to integrate the open-source codes and modules, archive all the data, establish multi-scale and multi-physics workflows, manage submission to clusters or the cloud, and provide links to the proprietary solutions through open-data standards that will be shared by both. AIDA is mostly developed within the EPFL group, notably using a joint open-source license (MIT BSD) shared by Bosch and EPFL. It is based on an agnostic framework currently supporting both Django and SQLAlchemy, provides Python modules both on the server and on the client side, authenticated APIs for programmatic submission of new calculations or data search/retrieval, and supports multiple back-ends (MySQL, PostgreSQL, etc) including schema-less data. It is currently used to organize, store and execute complex high-throughput workflows involving Quantum ESPRESSO (to name a few - also SIESTA, VASP, FLEUR, Yambo, Wannier90, and others are supported) and can be easily extended to any other computational code. Within SS1, AiiDA is used to:
 - interconnect Ginestra[®] with external databases and/or QE codes
 - manage the input/output and execution of workflows for the evaluation of materials properties on demand by using QE
 - data management, storage and curation.

The code interconnection scheme behind the SS1 execution is summarized Figure 3: a Graphical User Interface (GUI), namely Ginestra[®] API allows for the access to Ginestra[®] functionalities and to the internal material library. The GUI allow also the user to access external material databases and the DFT simulation ambient. The connection to external world is managed by different functionalities of AiiDA. In particular, OPTIMADE API allows user to retrieve material data from external databases on the basis of the OPTIMADE protocol; AiiDA-POST API manage the inward/outward connection with Quantum Espresso. AiiDA-POST is a plugin that extends the functionalities of the AiiDA's web interface that conforms to the RESTarchitecture. The REST API allows for querying the

database through a web service, exposing the underlying database where AiiDA is running, for their node properties and relationships. AiiDA-POST acts like a bridge to convey information to and from AiiDA through HTML communication. It deals with the submission of workflows, retrieval and query of data, material structure import, status checking of ongoing calculations, and more. All of that can be done locally or remotely through HTTP calls.

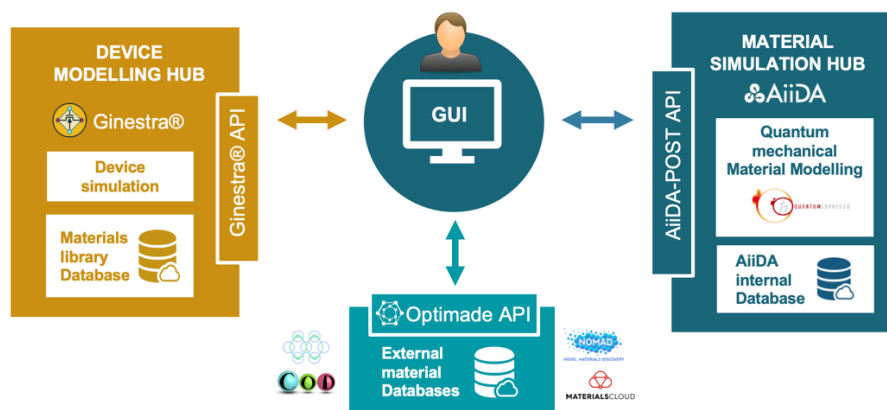


Figure 3: Scheme of REST-API interconnection among constituent codes within Success Story 1

Conceptually the use steps are the following:

- Device setup: select the device type (e.g. PCM), device structure (e.g. thickness, geometry, contacts, etc), and materials (e.g. GST chalcogenide).
- Materials data setup: search materials parameters within internal Ginestra® materials library. If not available, search in external databases and/or (if not available) launch a set of DFT calculations to generate missing data.
- Device modelling: by using the materials properties as input, launch the simulation of the electrical device problem.

Materials property on demand and implemented workflows

In the spirit of SS1, we first identified the minimum set of material parameters that Ginestra® uses as input (along with other structural and environmental data) to simulate the electrical response of a selected devices:

- Ground state atomistic structure
- Energy band-gap (crystal) / mobility gap (amorphous)
- DOS and defect/trap energy levels
- Effective mass (crystal)
- Permittivity ϵ_0
- Defect formation energy and defect type analysis (acceptors vs donors)
- Defect transition energies.

Based on this requirement, we achieved robust and ready-to-use AiiDA workflows for materials properties. They are: total energy, band structure, band gap, geometry optimization, projected density of states, effective masses,

dielectric constant, defect formation energy, barrier energy for defect diffusion, thermal transport, coupled electron-phonon transport. With the development and use of a specific plugin (repository at <https://github.com/aiidateam/aiida-quantumespresso>), AiiDA offers the possibility to access and automatically control the execution of complex quantum mechanical calculations performed with the QE suite. In general terms, the AiiDA workflows/workchains cover the whole process from the retrieval of the initial structure of the system under investigation to, e.g., the determination of the ground state, band structure, and all the needed steps in order to access the final physical quantity of interest, as shown in Figure 4 for the case of relaxation of diamond crystalline structure.

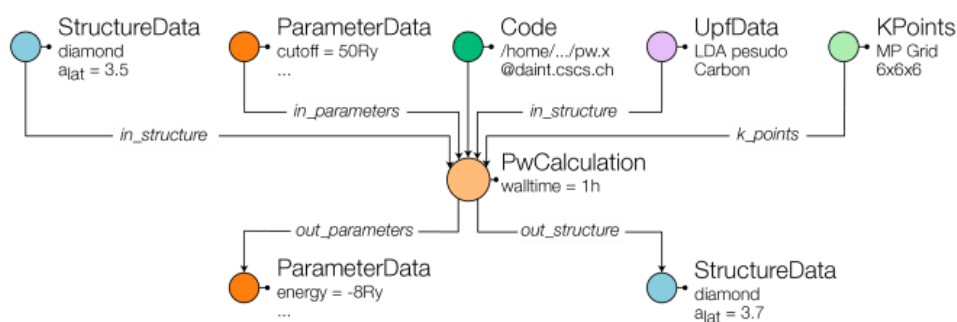


Figure 4: AiiDA-quantumespresso plugin used to relax a diamond crystal. The input/output data are represented as nodes in a provenance graph connected by logical links. The code in input defines the executable to be launched. Additional input nodes specify parameters for the calculation.

Ground-state structure is obtained via the relaxation of the atomic structure, through total-energy-and-force minimization procedure. A workchain for this property was implemented in the *aiida-quantumespresso* package:

aiida_quantumespresso/workflows/pw/relax (PwRelaxWorkChain)

It handles the atom position and unit cell volume relaxation. Also, it provides error checking, such as sanity checks for the volume change between iterations, restart capabilities, and the option for a final self-consistent-field calculation. The relaxation workchain is based on the basic workchain for Quantum ESPRESSO pw.x calculations:

aiida_quantumespresso/workflows/pw/base (PwBaseWorkChain)

which allows for the basic generation of the input file and its main parameters, such as atomic pseudopotential, k-point mesh, planewave cutoff, etc.

Bandstructures of the materials are calculated with the *PwBandStructureWorkChain*:

aiida_quantumespresso/workflows/pw/band_structure (PwBandStructureWorkChain)

This workchain firstly determines the calculation inputs based on the specified protocol. Then it employs the relaxation workchain. It then determines the symmetry of the crystal structure and generates a standardized high-symmetry path through the Brillouin zone using the SeeKPath analyzer available in AiiDA. Finally, it computes the band structure, which is stored as node objects in the AiiDA database.

The **band gap** is determined through the analysis of the band structure. Therefore, the band-gap workchains are based on the *aiida_post/workflows/bandgap (PwBandGapWorkChain)*.

A workflow, *PdosWorkChain*, was implemented to calculate the total and partial **density of states** (DOS) within the AiiDA-QuantumESPRESSO package by using the *projwfc.x* postprocessing code.

The **effective mass** is also extracted from the analysis of the band structure and it is also based on the *PwBand-StructureWorkChain*. We perform a quadratic fitting of the band structure near the top/bottom of the valence/conduction bands, typically at the centre of the Brillouin zone. From the band curvature, the effective mass for electrons or holes is inferred. It was implemented as an extra calculation in the bandgap workflow:

aiida_post/workflows/bandgap (get_effective_mass).

The **dielectric constant** is calculated through Density Functional Perturbation Theory (DFPT) with the *ph.x* phonon code of the QE suite. The workflow was implemented in the *aiida-defects* package, as it is an input for other workflows in that package. The present implementation supports advanced solutions for correction of the electronic structure (e.g., DFT+U), beyond standard DFT accuracy.

The **defect formation energy** is evaluated from first principles by using the *AiiDA-defects* plugin, that uses QE, as a DFT engine. AiiDA-defects consists of several modules allowing the creation, exploration, and manipulation of pristine and defective cell/supercell structures and containing AiiDA workflows to automatically calculate defect formation energies according to different correction schemes. The alpha version of the AiiDA-Defects plugin is available on GitHub (repository at <https://gitlab.cc-asp.fraunhofer.de/intersect/aiida-defects>), an improved beta version is currently being developed. This is most advanced and computationally demanding workflow implemented in SS1.

Following the approach proposed by Freysoldt and Van de Walle, the formation energy of a defect X in the charge state q is defined as

$$E^f[X^q] = E_{tot}[X^q] - E_{tot}[bulk] - \sum_i n_i \mu_i + q[E_F + E_v + \Delta V_{corr}].$$

$E_{tot}[X^q]$ is the total energy derived from a supercell calculation –performed at the DFT level – of the system containing the defect X relaxed in the charge state q , and $E_{tot}[bulk]$ is the total energy for the pristine crystal (host, generally bulk) using an equivalent supercell. The integer n_i indicates the number of atoms of type i (host or impurity atoms) that have been added to (or removed from) the supercell to form the defect, and the μ_i are the corresponding chemical potentials. E_F is the Fermi energy, referenced to the valence band maximum in the host, E_v . The last term, $E_{corr} = q\Delta V_{corr}$, is a correction term to align the reference potential in the defective supercell with that in the host system. This accounts for finite-size corrections within the supercell approach, such as electrostatic and/or elastic interactions between supercell replicas, or finite k-point sampling, as in the case of shallow defects. Once the defect formation energies are calculated for different charged states, the **defect transition energies** are straightforwardly evaluated from a linear intersection.

AiiDA-defect consists of several modules allowing the creation, exploration and manipulation of pristine (bulk) and defective supercell structures starting from the conventional/unit cell of a selected material through AiiDA (*aiida_defects/tools*) and containing AiiDA workflows to calculate defect formation energies according to correction schemes (*FormationEnergyWorkchainQE*) automatically. The latter includes workflows for the automated calculation of the DFT ground-state electronic structure, electrostatic potential V_{es} and charge densities (*aiida_defects/pp*), the macroscopic bulk dielectric constant ϵ_0 (*formation_energy_qe(get_permittivity)*) and the

component elemental chemical potentials (*formation_energy/chemical_potential*), which can be used independently from the other modules of the package.

3.1.2 INPUT/OUTPUT/BACKWARDS PROCESSES

The description of key inputs and outputs per simulation step is summarized in Table 1, also describing the backward process starting from the desired output propagating back to the required input.

Table 1: Summary of input/output data for Success Story 1

	Input [IN] / Output [OUT]	Value type/ File extension	Description
Ground State simulation			
OUT	Minimum energy lattice and atomic geometry	.txt	Standard output of the total-energy-and-force optimization cycle based on DFT, from which optimized geometry and lattice crystal can be extracted.
	Charge density	.xml	Results of self-consistent DFT cycle
	To perform total-energy-and-force optimization		
IN	Initial lattice and atomic positions of primitive cell	.cif/.xyz	File with the initial geometrical parameters extracted from experimental data or materials databases.
	Initial DFT parameters	.txt	Numerical parameters (pseudopotentials, k-point mesh, threshold parameters, energy cut-off, XC functional) for the definition of the DFT cycle
Bandstructure simulation			
OUT	Bandstructure, bandgap, and effective masses	.txt	Log file containing the single particle energy values as a function of the k-point resulting from a non-self-consistent DFT calculation. Bandgap and Effective masses results from the same numerical data
	To compute the electronic properties of materials		
IN	k-point path	.txt	Crystalline position of k-point path across the Brillouin zone
	Charge density	.xml	Results of self-consistent DFT cycle

Electrostatic potential simulation			
OUT	Electrostatic potential	.xsf/.cube	3D grid file with the V_bare+V_Hartree contribution resulting from postprocessing.
	To compute Ves in supercell (with and/or without defects)		
IN	Periodically repeated supercell, hosting (in case) diluted (i.e. not interacting) defect	.txt/.xml	Extended cell atomic position resulting from DFT optimization in the presence of (charged) defect
	Charge density	.xml	Results of self-consistent DFT cycle
Dielectric constant simulations			
OUT	Dielectric constant	Real number	Electronic contribution to the dielectric
	Simulation of e0 through DFPT simulation		
IN	Optimized geometry	.txt	Results of the optimization DFT problem
	Charge density	.xml	Results of self-consistent DFT cycle
	Initial PHonon parameters	.txt	Numerical parameters (q-point mesh, threshold parameters, atomic masses) for the definition of the DFPT cycle
Device modelling			
OUT	Electrical Characteristics	.txt/.dat	Log file with the I-V and C-V characteristics
	Defect/Trap map	.txt/.dat	Map file of the defect energy distribution as a function of the material thickness
	Device electrical modelling		
IN	Device structure	.cad	3D description of the device type and structure
	Materials parameters	.txt	Data resulting from all previous DFT calculations and related post-processing
	Ambient conditions	.txt	List of values such as working temperature, applied voltage, metal contacts

3.1.3 CHALLENGES AND GAPS ANALYSIS

The main challenges of Success Story 1 are:

- Weak stability of complex workflows, especially of AiiDA-defect. The defect formation energy and, more generally, the thermodynamics of defects in solids are advanced properties that cannot be straightforwardly extracted by the output of a single DFT calculation. Rather, this requires a more refined theoretical framework and the definition of a multistep post-processing procedure that requires decision processes from expert in the field that are difficult to automatize (e.g. the definition of the proper chemical potential, or the symmetry of the local charge model).
- Lack of further materials properties. For the complete material characterization, Ginestra® code would require further advanced properties (e.g. relaxation energy, thermal conductivity, electron-phonon scattering rates, defect diffusion barriers) that are very high-level tasks, whose theoretical models and their code implementation are still top challenges in current scientific research. The corresponding workflows have not yet been implemented.
- Atomic model of amorphous systems. In the absence of direct experimental results about the atomic structure of the amorphous phase, the identification of a reliable geometry is a major challenge for DFT simulations. To solve this problem we are experimenting an original approach which combines classical Molecular dynamics (MD) and DFT simulations. This multi-scale approach is based on 4 steps:
 - Classical MD model on large cell (thousands of atoms). Melting-and quenching cycles for system amorphization (LAMMPS code)
 - Cell reduction. Extraction of portion of system (hundreds of atoms) from the large MD cell with the constrain -to be check a posteriori- that the selected sub-cell has the same structural properties of the original one.
 - Relaxation with MD to adjust broken bonds at the border of the reduced cell
 - Relaxation with DFT to adjust atomic distances.

This approach has been recently implemented and tested on a few chalcogenide cases including GST [see e.g. A. Slassi et al Adv. Elect. Mater. 2201224 (2023)], yet it requires further optimization step to allows for the implementation of an automatic workflow.

3.1.4 VALIDATION AGAINST EXPERIMENTAL DATA/ MEETING KPI

To validate the main steps of Success Story 1 we applied the procedure described above on the case of PCM device based on $\text{Ge}_2\text{Sb}_2\text{Te}_5$ chalcogenide (GST). As a first attempt, we evaluate the electrical properties of the PCM device in high-conduction state, where the active material is in the crystalline form, starting from the material properties resulting from DFT simulation.

DFT simulations

We considered in particular GST in the cubic phase. The unit cell is composed of 27 atoms distributed in three 9-plane layers connected by Van der Waal interactions, as shown in Figure 5a. The correct description of the inter-layer coupling and of the electronic bandgap required the use of rrv10 exchange-correlation functional (rPW86 exchange + PBE correlation + van der Waals), and the inclusion of Hubbard-like atomic corrections, evaluated

self-consistently by using the ACBN0 implementation of the DFT+U problem ($U(\text{Ge})=0.04$ eV, $U(\text{Te})=2.06$ eV, $U(\text{Sb})=0.10$ eV). Ultrasoft pseudopotentials are used to describe electron-ion interaction. Single particle wavefunction (charge) are expanded in plane wave up to an energy cutoff of 30 Ry (300 Ry), respectively. A uniform $24 \times 24 \times 4$ k-point mesh is used to sample the 3D Brillouin Zone.

The initial atomic stack follows the following sequence: (Te-Sb-Te-Ge-Te-Ge-Te-Sb-Te)- (Te-Sb-Te-Ge-Te-Ge-Te-Sb-Te)- (Te-Sb-Te-Ge-Te-Ge-Te-Sb-Te). After crystal lattice optimization the dimension of the simulation cell result $a=4.26\text{\AA}$, $b=4.26\text{\AA}$, $c=53.86\text{\AA}$, $\gamma=120^\circ$.

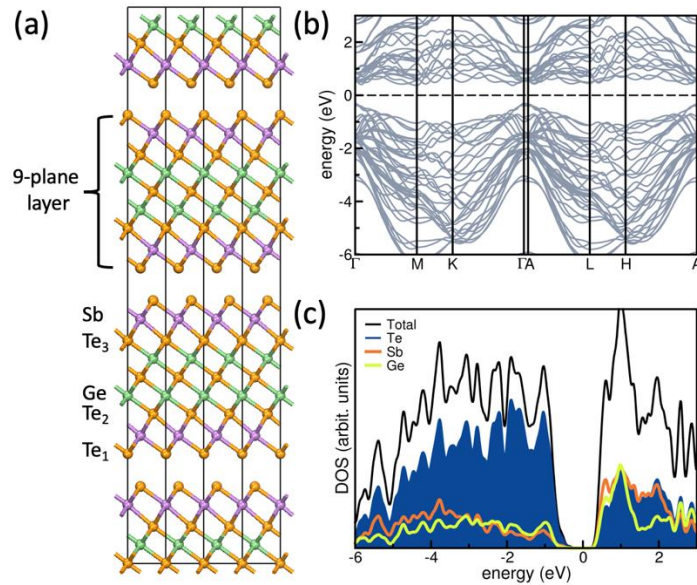


Figure 5: a) Atomic structure of crystalline GST (cubic phase); b) bandstructure; and total (black-line) and projected DOS.

The ground state electronic properties are summarized in panels b and c, that show the bandstructure and the DOS spectra of GST. The system is semiconducting, with a direct band gap at Γ equal to $E_g=0.83$ eV, in excellent agreement with the experimental data ($E_g=1.0$ eV). The calculated dielectric tensor has two inequivalent diagonal term $\epsilon_{xy}=29.19$ and $\epsilon_z=17.2$, whose average gives the value $\epsilon_0=25.2$.

The defect formation energy for the atomic vacancies [5 inequivalent sites (3Te, 1Ge, 1Sb)] are calculated in the Te-rich conditions, this imparts condition on the atomic chemical potentials:

$$\mu(\text{Te}) = \mu_0(\text{Te}) = \frac{1}{3} E_{\text{bulk}}(\text{Te}),$$

$$\mu(\text{Te}) = \mu_0(\text{Te}) = \frac{1}{3} E_{\text{bulk}}(\text{Te}),$$

$$\mu(\text{Sb}) = \mu_0(\text{Sb}) + \Delta\mu = [E_{\text{bulk}}(\text{Sb}_2\text{Te}_3) - 3\mu(\text{Te})]/2.$$

The summary of the defect formation energy and the corresponding defect transition states are summarized in Figure 6.

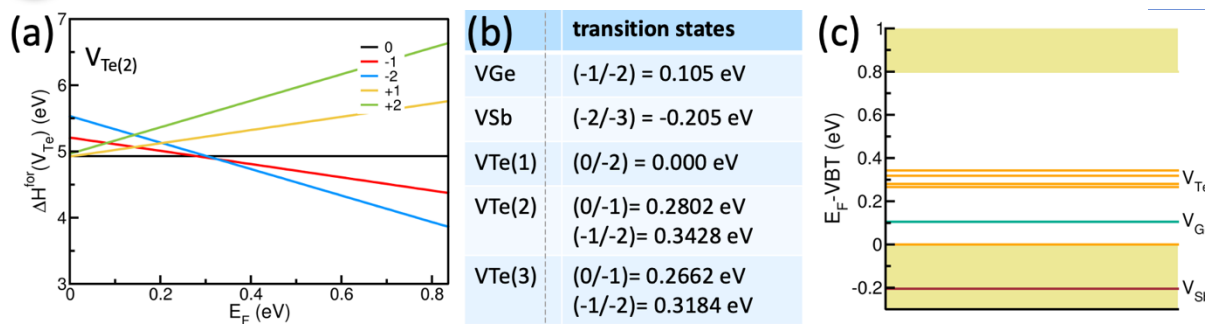


Figure 6: a) Formation energy plot as a function of the Fermi level position, for the Te(2) vacancy. X-axis energy scale corresponds to valence band top and conduction band minimum, respectively. b) summary of calculated defect transition states, c) band-alignment of transition state energy within GST bandgap.

Device simulation

By using the materials data from DFT simulation, we evaluated the electrical response of the PCM device in the high-conduction state, by using the Ginestra[®] code.

The used parameters are summarized in Figure 7a, while the resulting I-V characteristics are shown in panel b, along with the experimental data. The excellent agreement between the simulated and the measured data, poses the basis for the application of this approach to further and less explored cases, such as GST with different stoichiometries.

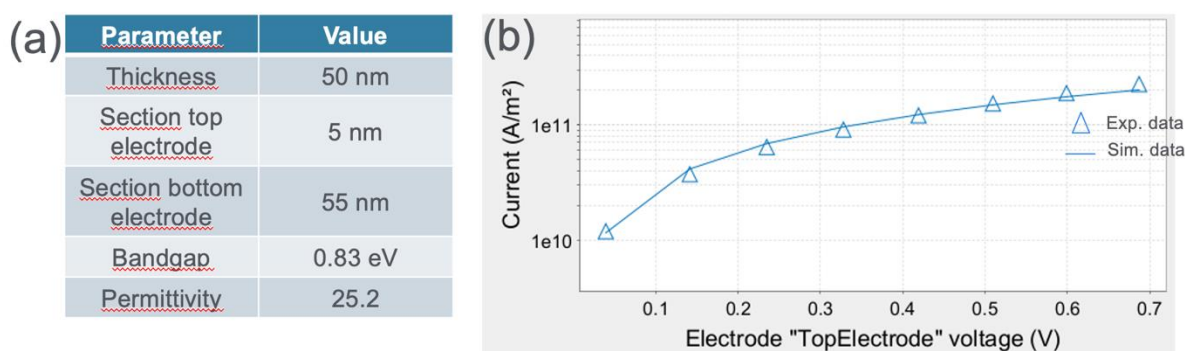


Figure 7: a) Summary structural and materials (from DFT) parameters of simulated PCM; b) Current-voltage simulated characteristics along with the corresponding experimental data.

The case of Ge-rich GST as well as the amorphous phase are ongoing. In particular, the need of characterization of the amorphous phase fostered us to developed a multi-analysis approach for the evaluation of the short and medium range order in disordered systems. The approach has been tested on simpler binary chalcogenide systems (GeSe). The results have been summarized in a scientific paper [A. Tavanti, A. Calzolari ACS Omega 7, 23255 (2022).]

3.1.5 BENEFITS OF OIP PLATFORM

The realization of the OIP would have a dramatic impact on the market of the semiconductor, especially in terms of reduction of the development time, reduction of resources and of the R&D staff costs. The realization of interoperable and automated software solution could help in accelerating the innovation of frontier technology, whose development requires giant investments. In particular the unique DFT capability in describing complex materials would allow for high-throughput material screening and the discover of “materials on design” that are the foundation of the so called “PPACT (Power, Performance, Area Cost and Time-to-Market) acceleration, an essential paradigm for industrial competitiveness.

Furthermore, the high automation level of IOP would allow to manage automatic workflows and to adapt the front-end complexity to the knowledge of the user, satisfying a common industrial need related to the lack of expertise (i.e., high impact).

3.2 SUCCESS STORY [2] - COMPOSITE MANUFACTURING SIMULATION (SISW)

This use case involves virtual manufacturing for an automotive woven reinforced composite B-pillar of a car-body as shown in Figure 8, using Resin Transfer Molding (RTM) as manufacturing technique. The main goal of the preliminary execution of this Success Story is to extend the multi-scale and multi-physics workflow of the manufacturing simulation of the fiber reinforced thermoset polymers with the performance simulations.

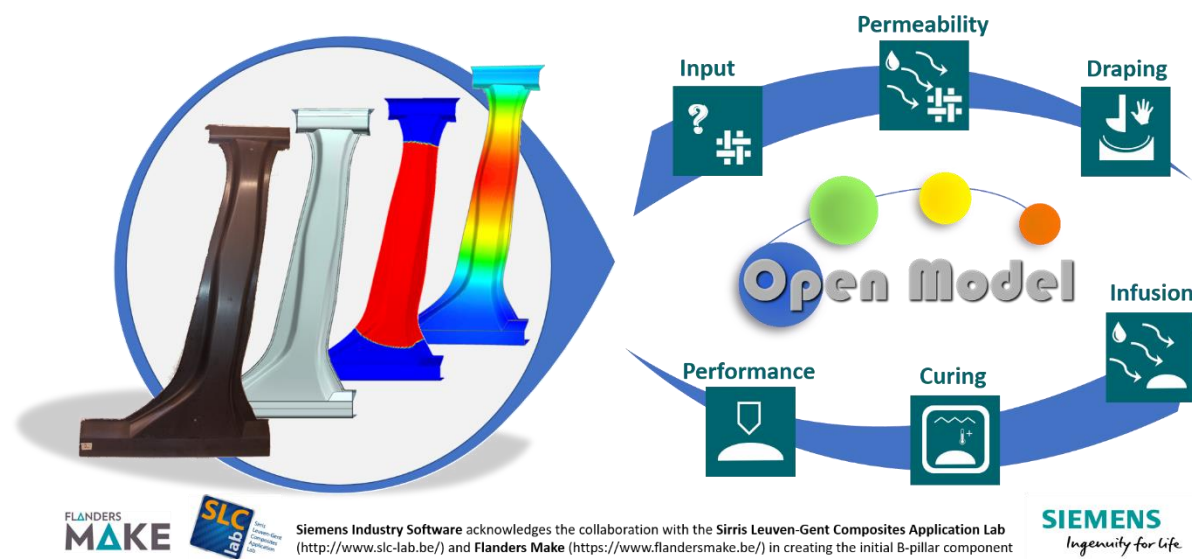


Figure 8: Schematic overview of the Success Story 2

3.2.1 MODELLING AND SIMULATION WORKFLOW FOR OFF-LINE EXECUTION

RTM is a commonly used composite manufacturing process that involves injecting liquid resin into a preform (a dry reinforcement material such as fibers) placed in a closed mold under pressure to manufacture composite

parts of complex shapes in a large quantity. The main manufacturing steps include draping of the dry reinforcement onto the mold, resin infusion, curing at elevated temperatures, following by a cooling down and releasing the part from the mold (see Figure 9) [1].

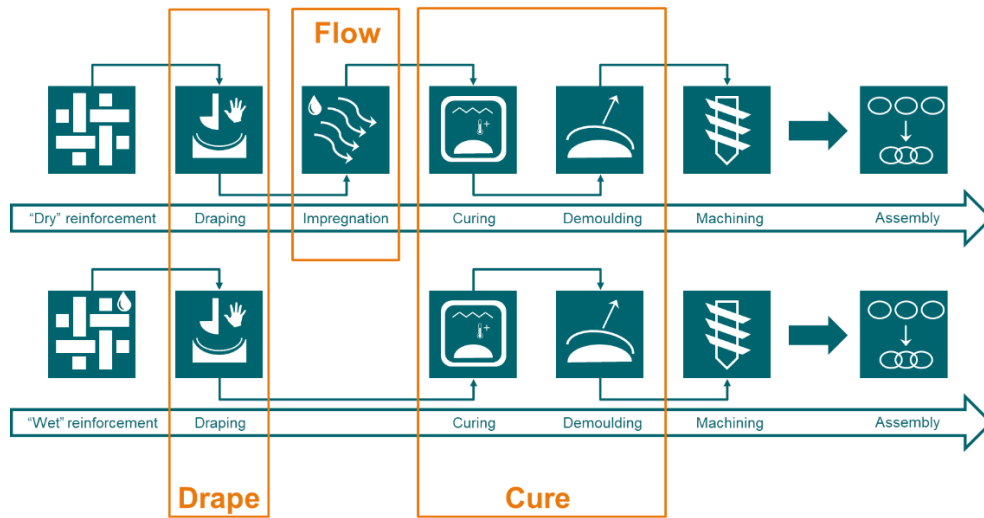


Figure 9: Typical thermoset composite manufacturing steps enabled by simulations: drape, flow, cure

The manufacturing steps can lead to defects as porosities/voids, dry spots, local fiber re-orientation, residual deformations, and residual stresses in the final part. To minimize trials and error and understand the impact on the part performance, one can rely on Computer Aided Engineering (CAE) software to determine optimal process-to-performance parameters. Siemens Digital Industries Software offers leading simulation tools for draping, infusion and curing modeling, allowing to virtually optimize the composite product performance.

An overview of the products used in the R&D work underlying this Success Story:

- **Simcenter 3D** - is a unified, scalable, open and extensible environment for geometry-based (3D) CAE simulation, enabling validation and optimization of products [2]
 - **Simcenter 3D Materials Engineering** enables virtual design and performance testing of new materials as part of complex products, drastically speeding up the design while reducing costs as compared to a fully test-based approach [3]
 - **Simcenter 3D Laminate Composite** speeds up laminate composite materials simulations with seamless connection to composites design, accurate solvers and adequate postprocessing [4].
 - **Simcenter Samcef** is a general-purpose finite element (FE) software for structural & thermal analysis, widely applied in mechanical, electrical, aeronautic, nuclear and naval engineering industries as well as in the fields of transport, civil and offshore engineering [5]
 - **Simcenter HEEDS** is a powerful design space exploration and optimization software package, accelerating product development by automating analysis workflows, efficiently exploring the design space for innovative solutions, visualizing trade-offs and optimizing designs [6].
- **Simcenter Star-CCM+** is a multiphysics computational fluid dynamics (CFD) software for the simulation of products operating under real-world conditions. It provides capabilities for Computer Aided Design (CAD), automated meshing, multiphysics CFD, postprocessing and design exploration [7].

Draping simulation with Simcenter 3D Laminate Composites

Draping of woven materials onto a mold involves laying out pre-woven fabric sheets in a specific pattern or orientation onto a mold to create a composite part. Several approaches exist to simulate such **draping process**. Simcenter 3D Laminate Composites offers a widely used **kinematic approach**, computing local fiber orientation based on the mold geometry, rosette, and draping strategy (Figure 10a). The **woven solver** computes fiber orientation for cloth woven with 2 sets of fibers at an angle to each other. As fibers are assumed non-stretchable, the angular change produces shear distortion. Figure 10b shows a shear angle distortion on a piece of fabric with a 90° weft fiber angle. The warp lengths (1) and weft fibers (2) do not change, but the yarn angle (3) in between does change. The shear angle is the difference between the original yarn angle and the distorted yarn angle. Quantification based on simulation allows identifying potential issues: if the shear angle becomes too large w.r.t. the fabric, the ply begins to wrinkle. Elements with large(r) shear angle shown in red color in Figure 10c.

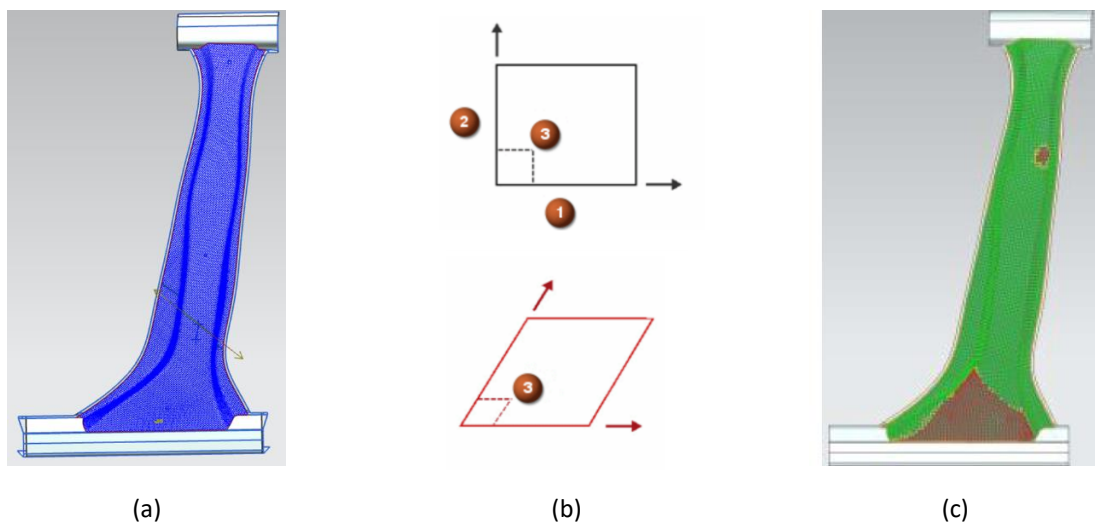


Figure 10: (a) Required input for draping simulation: mold geometry, rosette and draping strategy; (b) Schematic representation of the shear angle distortion on a piece of fabric; (c) Visualization of the shear angle distortion in the 60° -ply of a B-Pillar (in red). Ref. [8]

Such simulation-based quantification provides an **assessment** of the manufacturability of the part. Areas with a shearing problem can be addressed by taking measures at the design stage.

Draping simulation workflow with Simcenter 3D Laminate Composites include the following steps [4]:

- Creation of a 3D (three-dimensional) CAD model of the part with Simcenter 3D CAD Modelling tools
- 2D (two-dimensional) mesh generation of the part with Simcenter 3D FEM meshing tools
- Extrusion of 2D mesh to a 3D laminate, specifying layup with Simcenter 3D Laminate Composites
- Definition of woven ply material
 - The fiber properties of the warp and weft fibers – incl. fiber volume fraction
 - The balance coefficient, that specifies the number of fibers that run in the warp direction compared to the amount that run in the weft direction
 - (Optional) Nominal yarn angle (angle between warp and weft fibers); default is 90°

- The matrix properties
- Specification of the draping solver parameters
 - Draping Path: the method to define the primary direction for the woven
 - Starting Point: the starting point for fiber orientation calculations
 - (Optional) the Lock Angle – the shear angle, at which the fabric starts to wrinkle.
- Visualization of the fiber orientation. The red zones in Figure 10c indicate fiber shearing, as the change in the angle between the warp and weft directions exceeds the specified lock angle.

Permeability computation with Simcenter 3D Materials Engineering

An important parameter for the infusion simulation is the nominal **permeability**: the ability of a fluid (e.g., epoxy resin) to flow through a fibrous reinforcement when subject to an external force (pressure). This is unique to fiber reinforcement. An automated workflow for saturated permeability (steady-state permeability when the reinforcement is fully saturated with a test liquid, and flow is in the steady state) computation has been investigated and implemented as part of the Simcenter 3D Materials Engineering product (Figure 11)[9].

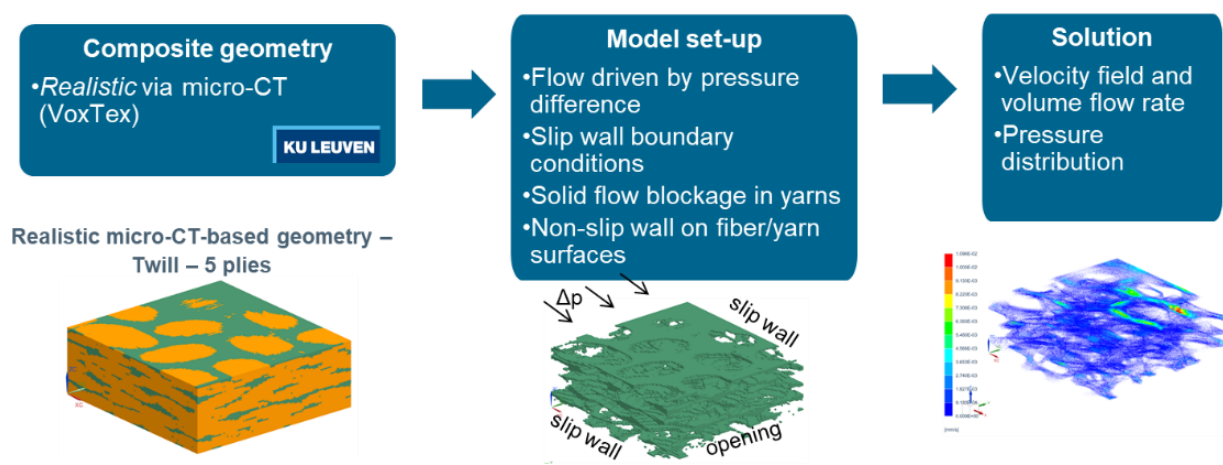


Figure 11: Permeability computation workflow

The following steps must be executed by the user to compute saturated permeability of a composite unit cell.

- Determination of the composite material small-scale geometry based on micro-CT measurements
- Model set-up using *Permeability Pre-processing* tab of the Simcenter 3D Materials Engineering
 - Selection of the finite element (FE) mesh in which the flow will be simulated
 - Specifying the fluid (resin) dynamic viscosity and its pressure at the inlet (from the resin provider)
- Solution execution with Simcenter 3D Thermal/Flow solver. As a result, the solver computes pressure and velocity fields which are used in the next step to compute the saturated permeability
- Permeability homogenization using *Permeability Homogenization* tab of the Simcenter 3D Materials Engineering.

Infusion simulation with Simcenter STAR-CCM+

Infusion Simulation with Simcenter STAR-CCM+ can help composite engineers to simulate and optimize the resin flow during RTM. It can provide insights into the filling pattern, process-induced defects such as void formation and suggest process improvements to reduce the manufacturing cycle time and cost.

Simcenter Star-CCM+ offers a general computational fluid dynamics solver approach, solving Navier-Stokes equations. This assumes the fluid is incompressible and preserves a lot of the physics of the flow in the solution sequence, so physical phenomena can be predicted more accurately.

The infusion simulation workflow involves the following steps:

- Execution of the draping simulation workflow (previous workflow). For infusion simulation, a finer mesh is required to ensure a good convergence. The modeling continuity is ensured by importing the mesh into Simcenter STAR-CCM+.
- Definition of the local permeability map based on the local fiber orientation and nominal permeability value of non-sheared fabric (using Demaria et al.[10] analytical formulation)
 - Permeability computation workflow
 - Assignment of permeability map to the B-Pillar model in Simcenter Star-CCM+
- Definition of the infusion channels and flow boundary conditions
- Definition of the solution of fluid mechanics to predict the resin flow in Simcenter STAR-CCM+
 - Finite Volume solver
 - Resin/air interface tracked with the Volume of Fluid approach
 - Time-step control based on flow speed
- Post-processing of the simulation results to analyze the flow front progression

Simcenter STAR-CCM+ allows to model infusion and curing processes in parallel. This is especially relevant for fast-curing resins, that start to harden during the infusion process. For the B-Pillar, the part was first fully impregnated before it started to cure. Therefore, in this Success Story, decoupled infusion and curing workflow is considered.

Curing Simulation with Simcenter Samcef

Curing simulations for thermoset composites use numerical methods to simulate the curing or hardening of the resin matrix that occurs when it is heated to a specific temperature for a certain amount of time. These simulations can predict the degree of cure, temperature distribution, residual stresses, and residual deformations in the composite material during and after the curing process. With Simcenter 3D and Simcenter Samcef software, curing predictions (thermal and mechanical) can be performed as a two-step solution, by sequentially coupling a thermal and a mechanical model, with the workflow in Figure 12.

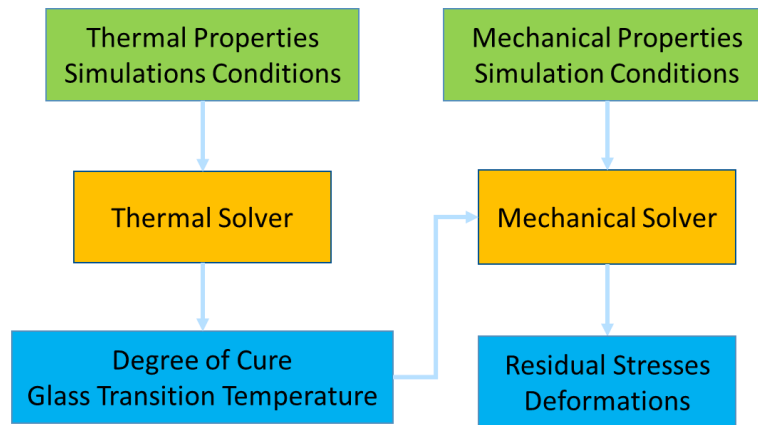


Figure 12: Illustration of the workflow for curing simulation and computation of residual stresses/deformations.

Curing simulations are key to optimize the curing process, by predicting the ideal temperature and time required to achieve a desired degree of cure and minimize residual stresses and deformations. One can identify upfront potential defects/weaknesses and apply updates to reducing the risk of failure in the final product.

Modal analysis with Simcenter Samcef

The final step in this multi-scale and multi-physics workflow of composite manufacturing simulation is **closing the loop** with performance simulation. Functional performance includes the product stiffness, strength, impact, durability, noise and vibration. A modal analysis was performed on the manufactured composite B-Pillar part. Natural mode shapes (i.e. shapes of natural vibration under excitation) provide insight in dynamic behavior of the part. Tuning the design can alter the mode shapes and corresponding resonance frequencies, which is an important instrument for engineers to understand and optimize the part and assembly behavior. Modal analysis for a composite part requires performing the following steps:

- Execution of the draping and curing simulation workflows described above
- Setting up a solution for modal analysis and chaining it with the thermo-mechanical solution
- Postprocessing the results. Visualization of frequencies and mode shapes

This entire process can be captured in a process integration and design space exploration tool as Simcenter HEEDS, to allow subsequent optimization of process and product parameters, finding feasible and most optimal design realizations, with improved efficiency, reduced costs, and higher quality processes and products.

3.2.2 INPUT/OUTPUT/BACKWARDS PROCESSES

The composite part of a car B-Pillar was designed and manufactured with Resin Transfer Molding [8]. Chomarar C-WEAVE™ 285T 3K HS woven sheets were cut and layered with a lay-up of $[60^\circ/-60^\circ/0^\circ/-60^\circ/60^\circ]$ on both sides of the structure. A foam insert Airex T92.100 is used to separate the inner and outer side of the B-Pillar. The resin system is epoxy-based Sicomin SR1710 with hardener SD8731. Nominal thickness of the top and bottom laminates is 2 mm with a thickness of 0.4mm of each ply. Nominal fiber volume fraction within the ply is 40%.

The description of key inputs and outputs per simulation step is summarized in Table 2, also describing the backward process starting from the desired output propagating back to the required input.

Table 2: Summary of input/output data for Success Story 2

	Input [IN] / Output[OUT]	Value type/ File extension	Description
Draping simulation			
OUT	Local fiber orientation. Shearing of the fabric	.fem/.dat/.txt	Local fiber orientation per mesh element and visualization of shearing of the fabric in Simcenter 3D mesh file (extraction to .dat/.txt is possible)
	To perform Draping Simulation Steps		
IN	Geometry CAD and meshed composite part	.prt .fem	Simcenter 3D part file Simcenter 3D mesh file with a laminate created with Simcenter 3D Composite Laminate
	Draping parameters	Real numbers	Coordinates of a starting point and Directional vector for draping
Infusion simulation			
OUT	Flow front distribution	.hdf5/.xml	Transient flow front during impregnation. The outcome from Simcenter STAR-CCM+
	To compute a flow front distribution during the resin infusion through the dry reinforcement		
IN	Geometry CAD Meshed composite part Simulation file with simulation objects and solutions	.prt .fem .sim	Simcenter 3D part file, mesh and simulation files. Laminate created with Simcenter 3D Composite Laminate and with executed draping simulation
	Viscosity	Real scalar	The viscosity of the resin
	Local fiber orientation	.txt/ .csv	File with fibers orientation from draping
	Permeability of non-sheared fabric	.txt	File with permeability tensor of non-sheared fabric from permeability homogenization
Permeability simulation			
OUT	Permeability	.log	Log file that contains permeability values

↓	To compute homogenized permeability of the composite unit cell based on pressure distribution and flow velocity fields		
IN	Meshed composite unit cell Option 1: microCT based	.dat	Files containing the segmented micro-CT image
	Meshed composite unit cell Option 2: CAD based	.mic	File containing woven materials information
	Viscosity	Real scalar	The viscosity of the resin
Curing simulations – degree of cure			
OUT	Degree of cure	.des	Map of transient degree of cure. The outcome from Simcenter Samcef thermal solver
	Glass Transition Temperature (Tg)	.des	Glass transition temperature (Tg) changing with the degree of cure. The outcome from Simcenter Samcef thermal solver
↓	Simulation of component heating and resin solidification to compute the degree of cure and the glass transition temperature.		
IN	Part material properties	.xml	Matrix thermal material properties (e.g. Specific heat, Curing heat, Cure kinetic Model, Tg of uncured and fully cured resin); Composite thermal material properties (Composite thermal conductivity)
	Mold material properties	.xml	Thermal expansion coefficient
	Temperature field	.txt or .csv	List of values (time, temperature)
Curing simulations – residual stresses/deformations			
OUT	Residual deformations and residual stresses	.des	Map of local stress/strain states obtained with Simcenter Samcef mechanical solver
↓	Series of simulations for curing, demolding and relaxations, to predict the residual stress and deformation		
IN	Part material properties	.xml	Matrix elastic material properties Fiber elastic material properties Composite elastic material properties
	Mold material properties	.xml	Mold elastic material properties
	Pressure field	.txt or .csv	List of values (time, pressure)
	Friction coefficient	.txt or .csv	List of values (time, friction)
Modal analysis			
OUT	Natural frequencies and mode shapes	.res	Table with natural frequencies and mode shapes from the result file of Simcenter Samcef.

↓	Modal analysis step to compute natural frequencies and mode shapes. Subsequent thermal-structural analysis to predict residual deformation		
Input	Geometry CAD Meshed composite part Simulation file with simulation objects and solutions	.prt .fem .sim	Simcenter 3D part file, mesh and simulation files. Laminate created with Simcenter 3D Composite Laminate and with executed draping simulation
	Eigenvalue extraction method	String	Method for eigenvalue extraction
	Range of frequencies	Real scalar	The range of frequencies

3.2.3 CHALLENGES AND GAPS ANALYSIS

The main challenge of this Success Story is its **complexity** covering different length scales and different physics. When executing a composite manufacturing simulation workflow, the following aspects need special attention:

- **Material characterization and Data management:** Composite manufacturing simulations require the use of large amounts of data, including material properties, geometry information, and manufacturing process parameters. Collecting all input data involves experimental campaigns and subsequent parameter identification (PI) for specific material models. For instance, to get all parameters for curing simulation, experiments must be run to measure viscosity vs. degree of cure, thermal expansion coefficient, shrinkage coefficient, pure elastic response, followed by PI for specific material models in the solver. Managing this data is challenging, especially for complex materials, parts and assemblies.
- **Computation time:** Composite manufacturing simulations can be computationally expensive, especially when using detailed models of the manufacturing process. The time required to perform these simulations can be a significant challenge.
- **Modeling accuracy:** Achieving the required accuracy with an affordable calculation time requires expertise, especially considering the complexity of materials, manufacturing processes and products.
- **User expertise:** Composite manufacturing simulation requires specialized knowledge of materials science, manufacturing processes and simulation software.
- **Model validation:** Validating simulation models against real-world data is an essential part of the simulation workflow, yet a challenge in its own (see next subsection).

The challenges presented in this Success Story are real, but they are not considered blocking points.

3.2.4 VALIDATION AGAINST EXPERIMENTAL DATA/ MEETING KPI

Validation against experimental data is crucial in design, manufacturing, and performance assessment of parts. Verification and refinement of models are key to understand and optimize the material & part behavior.

Modal analysis validation

The noise & vibration performance of the B-Pillar part was experimentally analyzed with Laser Doppler Vibrometry (LDV), a well-established technique for modal testing (Figure 13a). Experimental modal analysis (EMA) is then performed to calculate the modal parameters using Simcenter Testlab software [11], an integrated solution combining data acquisition with testing and analytics tools.

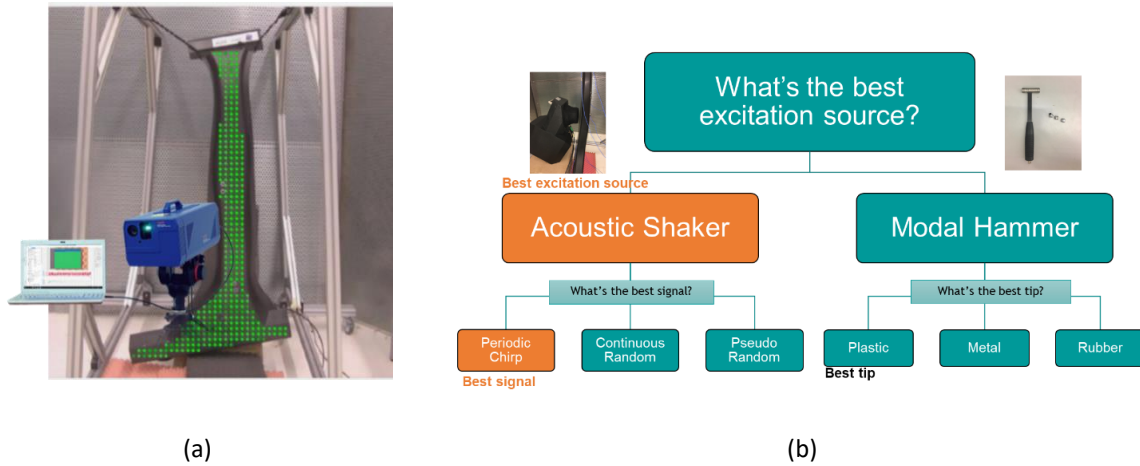


Figure 13: (a) Laser Doppler Vibrometer setup with a scanning grid mapped on the part ; (b) Different excitation sources and signal types for experimental modal analysis. The best excitation source and signal type highlighted.

Main challenge for industrial structural parts as the B-Pillar is to understand the modes in frequencies lower than 1000 Hz and update/mitigate them to avoid resonance issues elsewhere in the assembly. Typically used Piezo patches can't excite enough the component at this frequency range. Figure 13b summarizes the excitation sources and signal types that were evaluated to select the best option for excitation below 1000 Hz.

Selection criteria include signal noise, analyzing coherence functions, ease of use, level of energy provided to the system, possible impact on the structure. The Acoustic Shaker Q-LMF was selected, with the Periodic Chirp as the signal type. LDV results were compared against conventional accelerometer measurements. 10 accelerometers were glued to the B-Pillar: 6 at the front and 4 at the back side of the B-Pillar. Frequency response function (FRF) between LDV and accelerometers is presented in Figure 14. The difference between LDV and measurements with accelerometers is less than 1% in frequencies per mode.

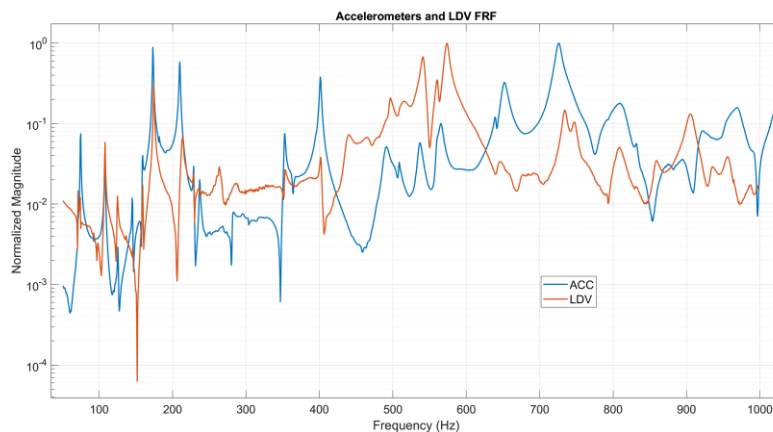


Figure 14: Frequency response function of LDV vs accelerometers

LDV measurements are chosen as reference for further validating of the simulation results. This experimental finding will be presented in the conference “Measuring by light. International meeting on optical measurement techniques and industrial applications. Delft, Netherlands, 28-30 March 2023”.

A comparison of the results obtained with experimental measurement techniques and a correlation with the simulation results is presented in Figure 15.

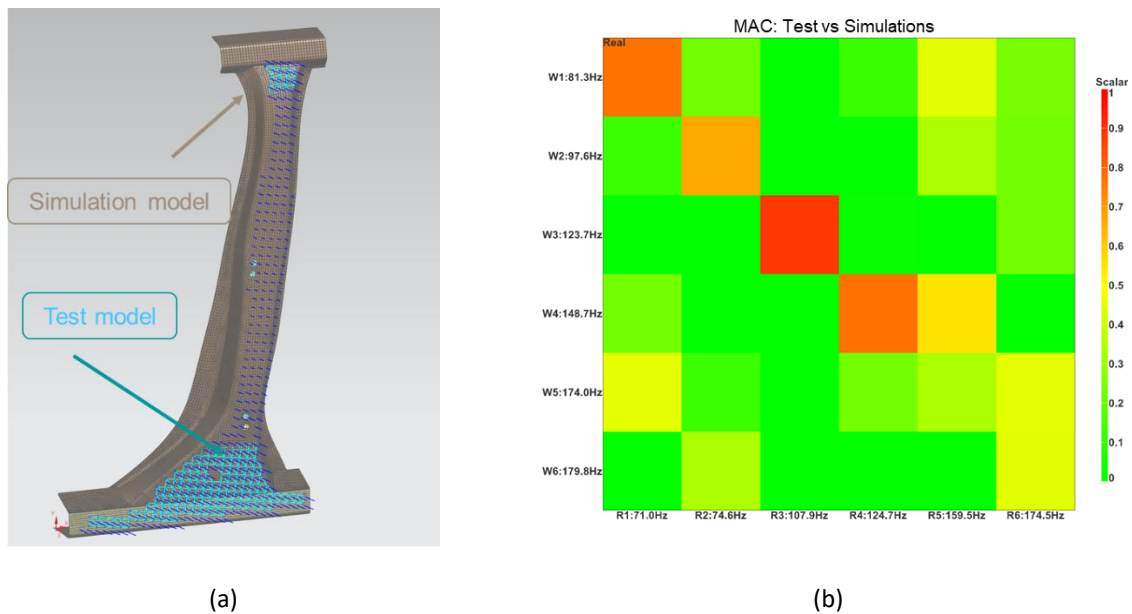


Figure 15: (a) Visualization of the testing scanning grid overlaid with the FEM model; (b) Modal Assurance Criterion (MAC) of Experimental and Simulations results

Good correlation between mode shapes and corresponding natural frequencies has been achieved especially at lower frequency range. Further improvement can be achieved by including manufacturing-induced effects to the model. This is an ongoing work:

- Master Thesis. Experimental and numerical modal analysis of a composite B-Pillar. Eduardo Marques, Instituto Superior Tecnico, 2023. Ongoing
- Master Thesis. Effect of curing on the part performance of a composite B-Pillar. Joao Viera, Instituto Superior Tecnico, 2023. Ongoing

Permeability and infusion simulation validation

Validation of the permeability computation for the B-Pillar was done using micro-CT-based numerical validation prior to the project. The results presented in [12] show a good agreement with the permeability map computed based on the draping simulations and verified against experimental data of the flow front progression in the B-Pillar according to Figure 16. A good agreement between simulation and test is shown in Figure 17.

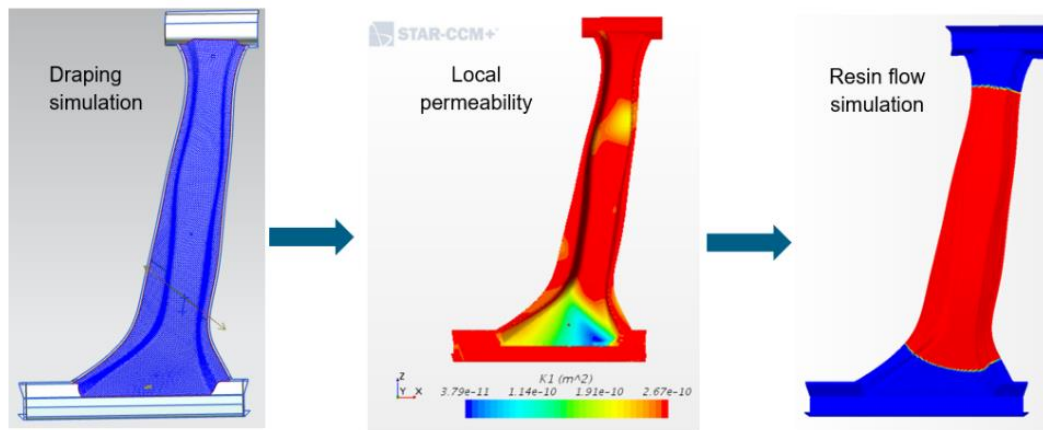


Figure 16: Simulation sequence: draping simulation; mapping of fiber orientations and computation of local permeability tensor, and resin flow simulation. Reproduced from [9]. Reproduced from [8]

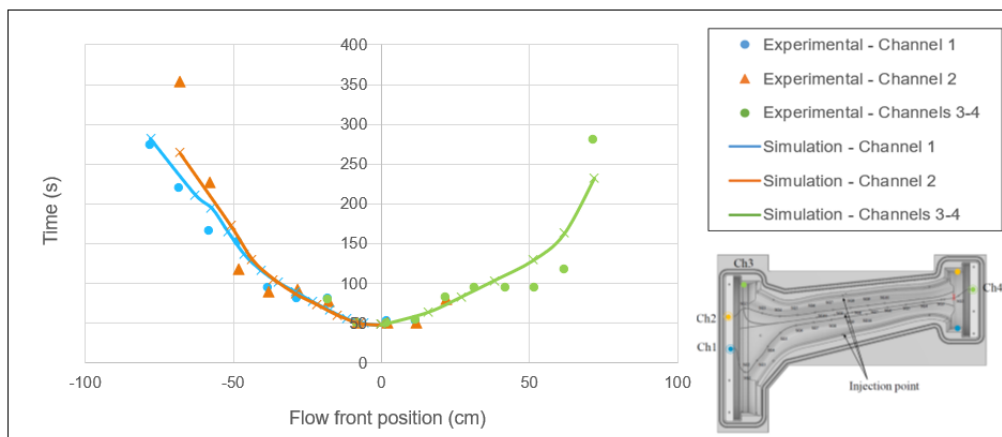


Figure 17: Time at which the flow front passes through each sensor location (symbols are experimental data; continuous lines are simulation results); on the right bottom corner, a scheme shows the sensor locations. Reproduced from [8]

Key Performance Indicators

Such material manufacturing digital twin can help industrial product manufacturers to **reduce design & manufacturing costs** by 20-30% and **time-to-market reduction** by 5% as less design iterations will be necessary. Decreasing the time-to-market often has a positive effect on the company as earlier product release translates in a higher revenue, since the products can be launched earlier than expected and meet the momentary market needs. Moreover, by optimizing simultaneously the manufacturing and performance aspects, smaller safety factors can be used, which will further allow to **reduce the component weight** – a target of 10% is proposed due to the innovative methodology. In addition to this extra reduction in weight, the productivity will increase (+10%) and the mold design **cost will decrease** (-15%) as the simulation workflow will minimize the trial-and-error approach. **Scrap rates can also be reduced** (-5-10%, depending on the application).

Given numbers provide an indicative assessment, their validation is beyond the offline execution of this Success Story and will be done later, during/after the online execution phase of this Success Story. Once the integration with the OIP OpenModel is in place as well as a full automation of the complete workflow, then exact quantification and KPI validation will become possible.

3.2.5 BENEFITS OF OIP PLATFORM

Composite manufacturing simulation workflow consist of many steps using multiple software tools, different pre/post-processing techniques, various scripts for data conversion. The seamless connection is challenging due to differences in file formats, modeling techniques, and user interfaces, thus adding an extra complexity to the full workflow execution. But the impact of having the full workflow available as 'one peace' is enormous. All KPI values described above can be achieved only once the full automation is in place.

Connecting composite manufacturing workflow with OIP OpenModel offers more value beyond an efficient workflow by automation. It can offer several benefits, including access to a wider range of expertise; collaboration and knowledge sharing; acceleration of product development - working faster together in an industrial value chain; reduce costs and risk for R&D. By leveraging external expertise and collaboration within the OIP OpenModel, organizations can quickly adapt their composite manufacturing simulation workflows to meet new challenges and opportunities. The platform can facilitate the sharing of best practices and the validation of simulation models, leading to improved quality in composite manufacturing processes.

3.3 SUCCESS STORY [3] – CIVIL ENGINEERING – REINFORCED CONCRETE (HYDRO, SITEF, HEREON)

Reinforced concrete is one of the most important structural materials currently used for buildings and infrastructure, in which corrosion of the reinforcement is vital in the design, lifetime, and cost (Figure 18). Replacing steel with aluminium reinforcements is interesting from both a design and environmental stand-point. Conventional cement causes damage to aluminium due to the high PH environment, hence a novel cement based on clay is used in this study. Ultimately the longevity of a structure depends on the performance of the barrier formed on the aluminium during concrete curing. Modelling the in-service behavior is a multi-scale process, making it difficult to accurately model. Hence, a systematic workflow simplifying the use of respective computational models enables model-based optimization.



Figure 18: Examples of aluminium reinforcements in concrete. Reproduced from [13]

3.3.1 MODELLING AND SIMULATION WORKFLOW FOR OFF-LINE EXECUTION

The lifetime of infrastructure and buildings depends largely on the corrosion behavior of the used steel reinforcements. A failure of the barrier properties of the used concrete quickly results in water intrusion and damage to the reinforcements. Leading first to cracks in the concrete than spalling and finally structural failure (see Figure 19).



Figure 19: Example of steel reinforcements corroding in conventional concrete. Reproduced from [13]

For unprotected aluminium embedded in conventional concrete the situation is even more precarious. As can be seen in Figure 20, it will easily corrode due to a chemical reaction with the alkaline environment of the concrete. This reaction, known as an alkaline attack, causes the concrete to produce hydroxide ions, which attack the protective oxide layer on the surface of the aluminum. As a result, the aluminum begins to dissolve, producing hydrogen gas and aluminum hydroxide. This process can lead to the formation of voids in the concrete, compromising its strength and durability.



Figure 20: Example of aluminium reinforcements corroding in conventional concrete Reproduced from [13]

The rate of corrosion of aluminum in concrete depends on several factors, including the pH level, the presence of chloride ions, the moisture content of the concrete, and the thickness and composition of the oxide layer on the surface of the aluminum. To prevent aluminum corrosion in concrete, measures such as coating the aluminum with a protective layer or using a corrosion inhibitor.

Another way is to use a concrete formulation with a much lower pH level (see Table 3), which is the way that is used in this application.

Table 3: Concrete formulation as used in this application. Reproduced from [13]

Component	Fresh water	Seawater
Cement (Anlegg SR)	186.9	186.5
Calcined clay	228.4	228.0
Free water	178.5	178.2
0-8 mm Årdal sand	974.8	974.8
8-16 mm Årdal gravel	676.7	676.7
SIKA Viscocrete 6225	8.3	14.8
SIKA Airpro V5 1:9	2.1	6.6
CaCl ₂	16.6	16.6

While the pH level is much lower there still exists the opportunity for corrosion due to the presence of calcium chloride, which is used to accelerate the setting time and increase the strength of the concrete.

Calcium chloride is hygroscopic, which means it attracts moisture from the air and can increase the moisture content of the concrete. When the moisture content of the concrete is increased, it can increase the rate of corrosion of the reinforcement. Furthermore, chloride ions present in the calcium chloride penetrate the concrete and come into contact with the reinforcement. The chloride ions react with the metal, causing it to corrode.

At this point the barrier performance of the concrete becomes essential to prevent corrosion by preventing or slowing down the movement of free chloride ions to the substrate surface. Based on initial testing a dense layer is formed during the initial curing phase of the reinforced concrete (see Figure 21).

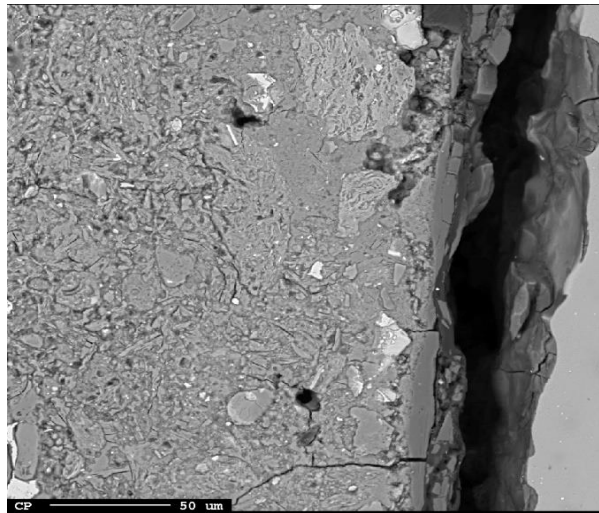


Figure 21: Image of concrete and aluminum interface area. Cracks in the concrete due to sample preparation. Dark grey area close to the aluminum surface indicates a dense barrier formed during the initial curing phase [14].

This dense layer is composed of aluminum, magnesium and calcium compounds as can be seen on Figure 22 showing the elemental composition of the interface area.

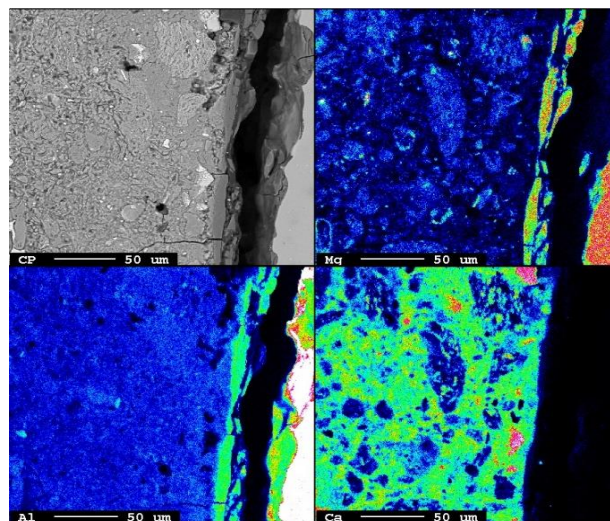


Figure 22: Different elemental distributions in the concrete-aluminum interface area. Top left: Visible light image of the area. Top Right: Magnesium concentration. Lower Left: Aluminum concentration Lower Right: Calcium concentration [14].

To characterize the mechanical behavior of aluminum reinforced concrete four-point bending tests are performed. A four-point bending test is a mechanical test that measures the flexural strength and stiffness of a material under bending. In this test, a specimen is supported by two lower supports and loaded by two upper supports that are equally spaced from the center (see Figure 23). The specimen experiences a constant bending moment and no shear stress between the two upper supports. This test is suitable for both brittle and ductile materials, as it avoids high stress concentrations at the loading points. The performed test are replicated by using simulations in Abaqus an example mesh can be seen in Figure 23. This is the macro-scale level used in this model. Critical strain rates are extracted from this simulation and then used in the micro-scale model.

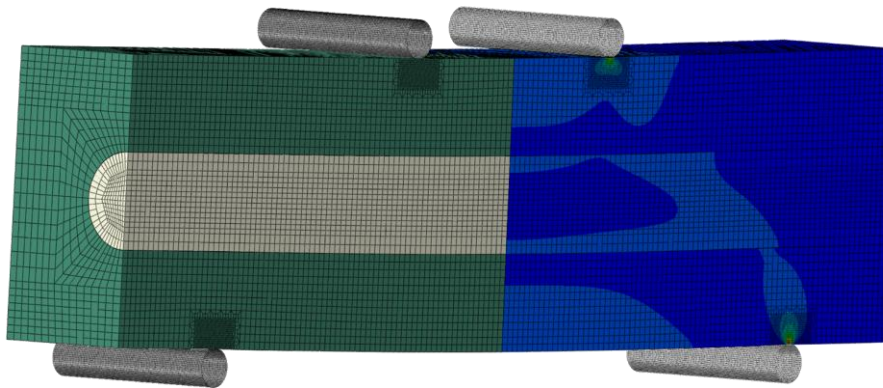


Figure 23: Setup for four-point bending test.

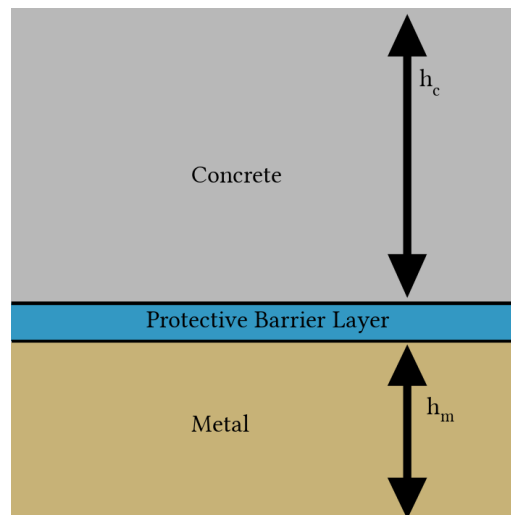


Figure 24: Layers present in Micro-scale model

A micro-scale model is used to reduce the mesh-size in the four-point bending test simulation, which would make the simulation prohibitively expensive. As shown in Figure 24 the micro-scale model captures not only the metal-concrete interface but also models the concrete-barrier layer and metal-barrier interface. Furthermore, experiments are performed to obtain the material properties of the barrier layer, which are the key to simulate the barrier performance. Additional testing is then required to calibrate the cracking probability in the micro-scale model.

Aluminum can be extruded in a variety of different shapes (see Figure 25), which could be beneficial for the mechanical performance and amount of reinforcement needed to reach the mechanical requirements. As such this basic simulation using a round bar is to be expanded by a shape optimization step. Combined with the macro-scale and micro-scale one can envision a workflow as shown in Figure 26. Which integrates a shape optimization loop into the model.

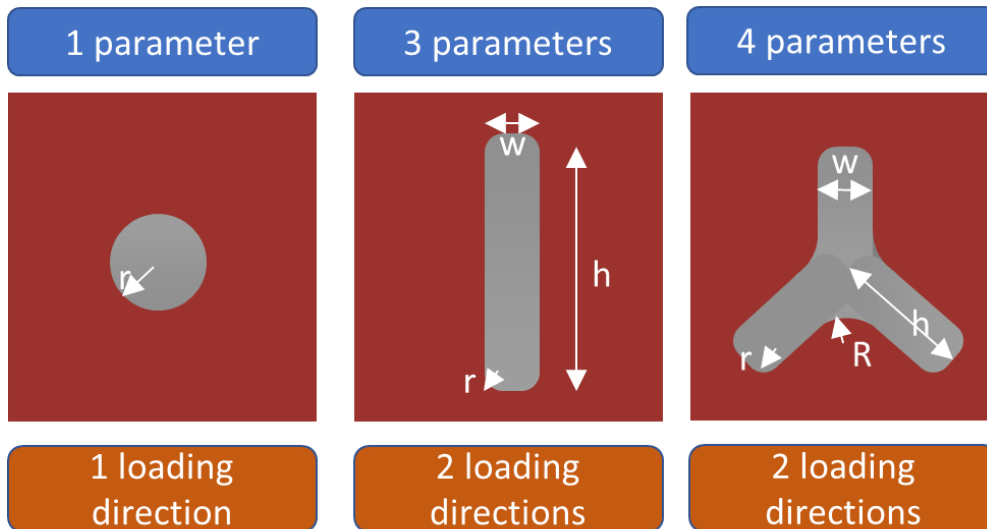


Figure 25: Example of aluminum extrusion profiles for reinforcement in concrete.

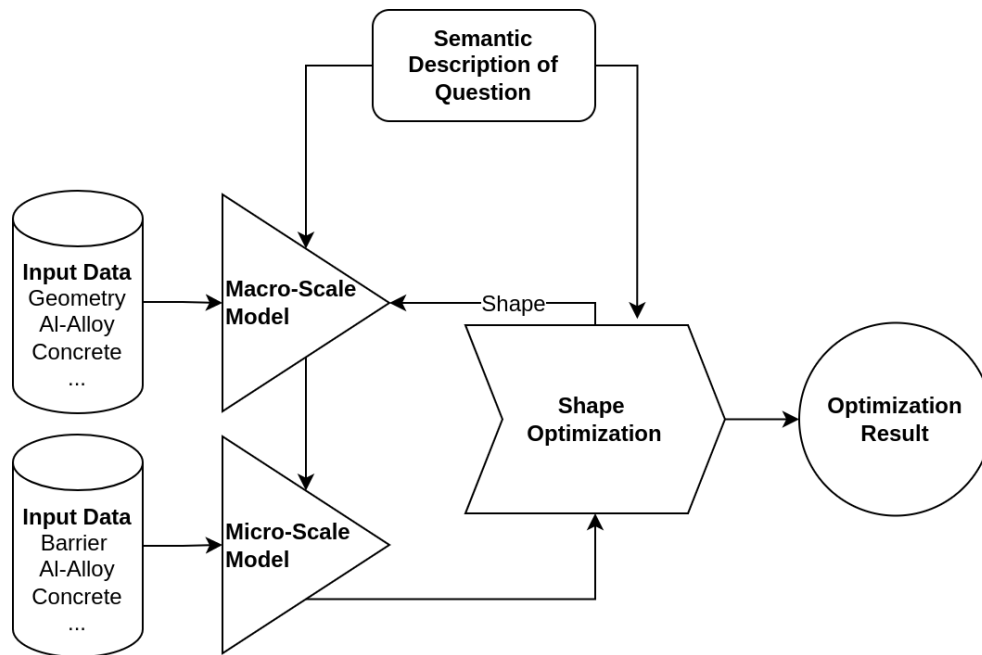


Figure 26: Flow Diagram of envisioned workflow.

This shape optimization capabilities are currently not available in OpenModel and can not be implemented in the given timeframe. Especially, since our modeling approach currently assumes symmetry, which in this case no longer be given, which would require much larger meshes. Furthermore, complex shapes that would appear in the shape optimization require more complex modelling since the interfaces can no longer be assumed to be perfectly attached to the substrate and voids are much more of an issue, which cannot be easily predicted. This would further require additional verification and calibration experiments, which cannot be justified in this project.

As such we have limited ourselves for the first version of this application to the workflow shown in Figure 27. This will be applied to a round and flat bar to demonstrate this application.

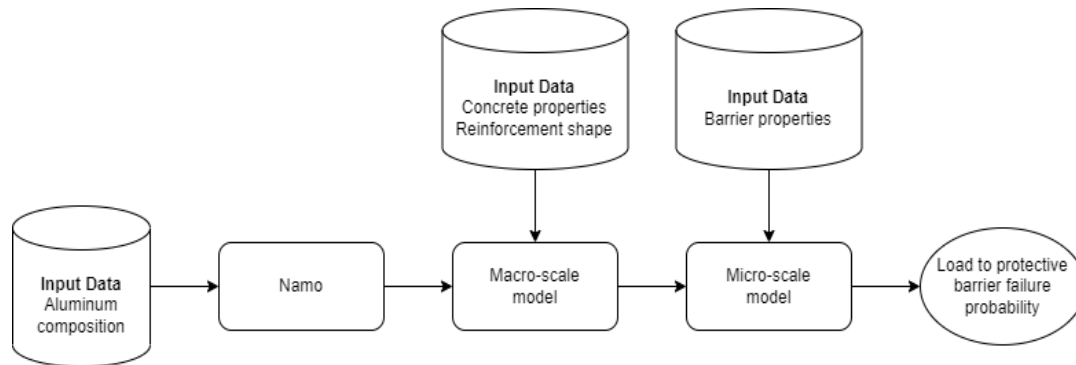


Figure 27: Flow Diagram of current workflow.

3.3.1.1 MODELS

NaMo a software developed by Hydro is used to predict the material properties of the aluminum reinforcements.

Two models a macro- and micro-scale are used to perform the mechanical simulation in an efficient way. Since the scales between the barrier and concrete layer thickness are vastly different, which would lead to a very expensive simulation.

NaMo

NaMo is a combined classical Kampmann-Wagner numerical precipitation model combined with yield strength and work hardening models for industrial aluminium alloys, focusing on the 6xxx alloy series[15–17]. The input to NaMo is the chemical composition and the heat treatment temperature profile. It predicts the evolution of the particle size distribution of the main hardening β'' and β' precipitates. From the state of the microstructure after heat treatment the yield strength and work hardening sub-models can predict the Yield strength and stress-strain curves of the final alloy.

Macro-scale model

The macro-scale model is used to simulate the experimental setup of the four-point bending test. This test is used to measure the flexural strength and stiffness of the reinforced concrete material consisting of an aluminum rebar and concrete. The macro-scale model is implemented in Abaqus, a finite element software that can handle complex geometries and nonlinear material behaviors. The model outputs the stress and strain distributions along the length of the rebar under different loading conditions. The critical strain values on the rebar are then identified as the ones that correspond to the onset of damage or failure in the barrier. These strain values are then used as inputs for the micro-scale model, which zooms in on a model that also models the barrier performance of the rebar and investigates its damage mechanics on the barrier.

Micro-scale

One of the objectives of this study is to develop a micro-scale model of the layer construction that accounts for the interaction between the concrete and the aluminum rebar. The model is implemented in FEniCS, a finite element software package that allows for complex geometries and nonlinear material behavior. The model considers both the interface between the concrete and the barrier layer, which prevents moisture ingress, and the interface between the barrier layer and the aluminum rebar. The material properties of the barrier layer are obtained from experimental tests and used to calibrate a damage model that captures its fracture behavior under different loading conditions. The micro-scale model can then be used to simulate the response of the layer construction under various environmental and mechanical scenarios and to evaluate the probability of barrier failure, which would trigger corrosion of the aluminum rebar.

3.3.1.2 SOFTWARE TOOLS

Abaqus

Abaqus is a powerful finite element analysis software that offers a wide range of capabilities in the field of mechanics. With Abaqus, users can perform simulations of mechanical systems and structures, including static and dynamic analyses, nonlinear material behavior, and complex geometries. The software is able to simulate a variety of loading conditions, such as thermal, electrical, and fluid flow, allowing for the accurate prediction of system behavior. Abaqus also has advanced capabilities for modeling contact, fatigue, and fracture mechanics, as well as multiphysics simulations that enable the analysis of coupled phenomena.

Fenics

FEniCS is a powerful open-source software suite for solving partial differential equations (PDEs) numerically. Its capabilities include the ability to define and solve complex PDEs using a variety of numerical methods, including finite element and finite difference methods. FEniCS supports a range of high-level programming languages, including Python, making it an accessible and flexible tool for researchers and practitioners alike. Additionally, FEniCS offers advanced features for automating the process of discretization, allowing users to easily specify and solve problems involving complex geometries, non-linear material properties, and multi-physics interactions.

Namo

NaMo is an in-house model developed by Hydro Aluminium over the last 25 years. It has both a graphical user interface and a command-line interface suitable for running calculations in batch mode. For OpenModel wrapper will utilise the command-line interface.

3.3.2 INPUT/OUTPUT/BACKWARDS PROCESSES

The description of key inputs and outputs per simulation step is summarized in Table 4, also describing the backward process starting from the desired output propagating back to the required input

Table 4: Summary of input/output data for Success Story 3

	Input [IN] / Output[OUT]	Value type/ File extension	Description
Material properties simulation (Namo)			
OUT	Yield strength	Text	The yield strength (single number)
	True stress – true strain curve	Text	File with tabular data
↓	Numerical precipitation model combined with yield strength and work hardening models for industrial aluminium alloys		
IN	Alloy composition	Text	
	Heat treatment temperature profile	Text	
Macro-scale simulation			
OUT	Critical strain area	.json	File containing the strain and stress values interpolated to the surface of the rebar in which a critical strain has been reached
↓	Mechanical simulation to obtain critical area for barrier damage		
IN	Aluminum properties	From Namo	Aluminum properties are obtained from Namo.
	Concrete properties		
	Geometry	stl	Geometry of the aluminum rebar
Micro-scale simulation			
OUT	Load to barrier failure probability	csv	
↓	Micro-scale simulation to evaluate the probability of barrier failure		
IN	Aluminum properties	From Namo	Aluminum properties are obtained from Namo.

	Concrete properties	Script	Mechanical and geometrical properties of the barrier c
	Critical strain area	Json	From macro-scale simulation
	Barrier properties	Script	Mechanical and geometrical properties of the barrier from measurements

3.3.3 CHALLENGES AND GAPS ANALYSIS

The original envisioned workflow cannot be implemented during this project:

- Missing shape optimization capabilities in OpenModel
- Missing experimental data
- Model extension outside of scope of OpenModel

The simplified workflow is missing:

- Composition of barrier layer from measurements
- Material properties of barrier layer – in progress.
- Validation data.

3.3.4 VALIDATION AGAINST EXPERIMENTAL DATA/ MEETING KPI

Currently no validation data is available.

Original KPI cannot be obtained using the simplified workflow. Reduced KPI will only predict the barrier failure probability for round and flat bars.

3.3.5 BENEFITS OF OIP PLATFORM

One of the challenges in developing complex systems is to integrate different models that operate at different levels of abstraction and granularity. To simplify the coupling between the different models, the OIPs provided wrappers can be used in concert with an ontologized description of the key performance indicators (KPIs). This enables a common understanding and communication between the different models and stakeholders. By using wrappers and a ontologized description of the KPIs, we can reduce the complexity and increase the interoperability of the system modeling process.

3.4 SUCCESS STORY [4] – METAL FORMING: RESOURCE EFFICIENT PROCESSING AND MANUFACTURING (HEREON)

The aim of advanced machine learning (ML) techniques is to speed up evaluation, correlation discovery, and optimization processes. We present a ML-based model that can link the properties of indirectly extruded Mg-Gd alloys to the alloy content and process parameters. This model enables us to predict various factors such as anisotropy and strength of Mg-Gd alloys based on objective functions. We validate our model against experimental data and show that it outperforms linear regression-based models in prediction accuracy. This model can also provide a rough estimation of how process parameters, alloy content, and properties are related in this alloy system or similar Mg systems. This can help reduce trial-and-error efforts or enable online quality monitoring in future alloy development. Our approach is promising and applicable to other systems with more data.

3.4.1 MODELLING AND SIMULATION WORKFLOW FOR OFF-LINE EXECUTION

The workflow is composed of four steps hyperparameter tuning, training, validation and generation of maps that identify suitable process parameter to material property mappings. To compare the ML based model to a more classical regression approach it is compared against the linear regression of a 2nd order polynomial. This order was chosen since it resulted in the lowest mean squared error (MSE) between first and tenth order polynomials for the current data.

As can be seen in Figure 28 the ML based model delivers both a more accurate description within the training data as well as for the test data. Overall reaching a much lower MSE of 26.71 compared to 278.66 for the classical regression approach.

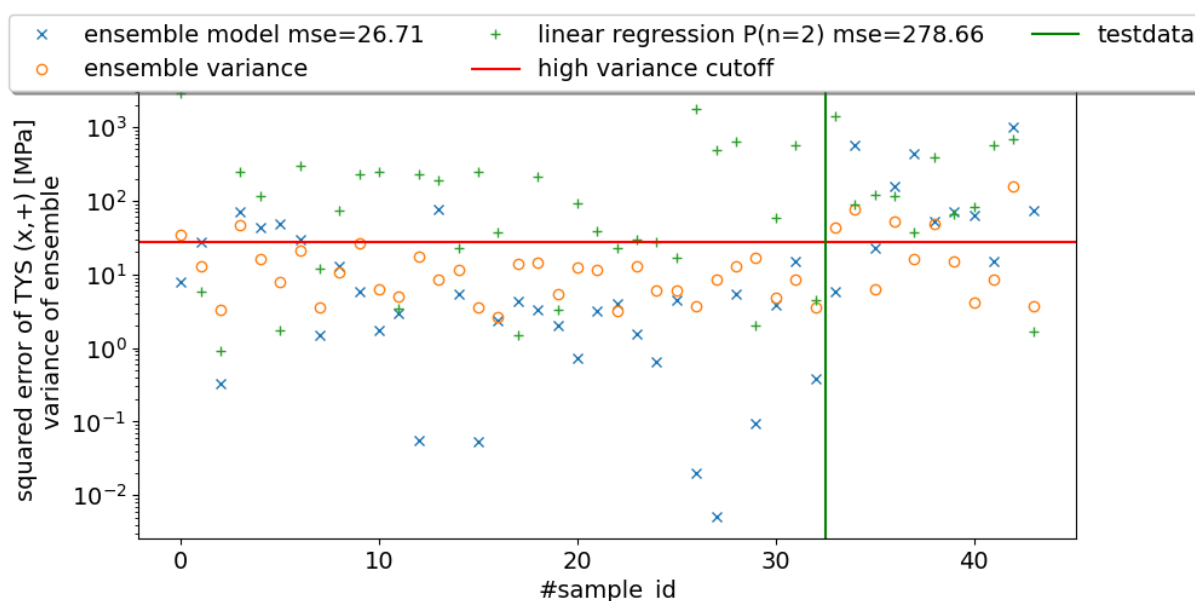


Figure 28: Modelled tensile yield strength compared between linear regression of a 2nd order polynomial to the ensemble model.

As an example of the ensemble model process, you can see the separate models in Figure 29 and the obtained ensemble average. As can be seen the single models vary widely due to randomness in the training process. While the obtained ensemble average only varies marginally between model trainings on the same data.

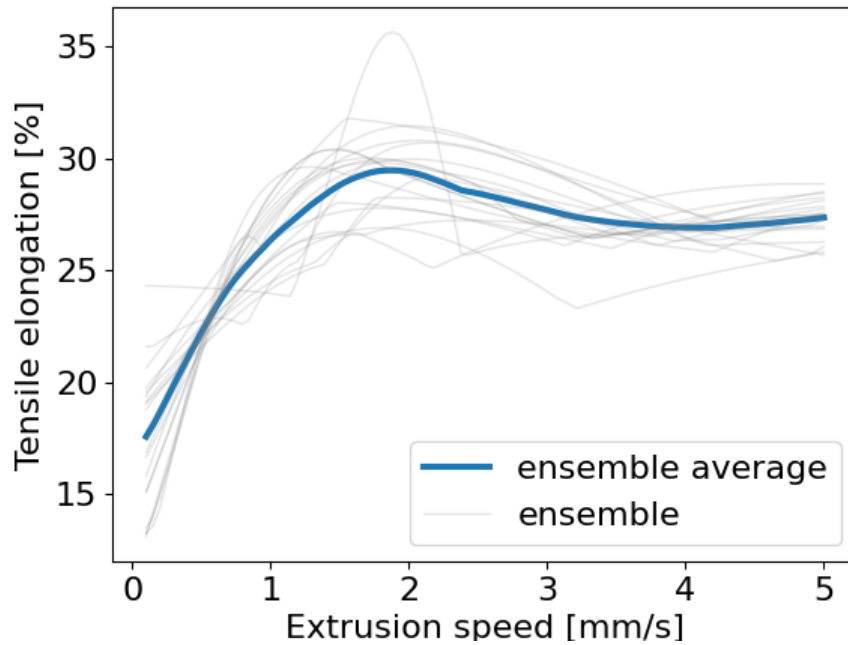


Figure 29: Tensile elongation at break based on ML over the extrusion speed for T=400, Gd=7.28.

The ML model then allows us to map the material properties over the process-parameter space resulting, for example, in the map shown in Figure 30. The surface shown is the compressible elongation for the magnesium 1%-gadolinium alloy over the extrusion speed and temperature.

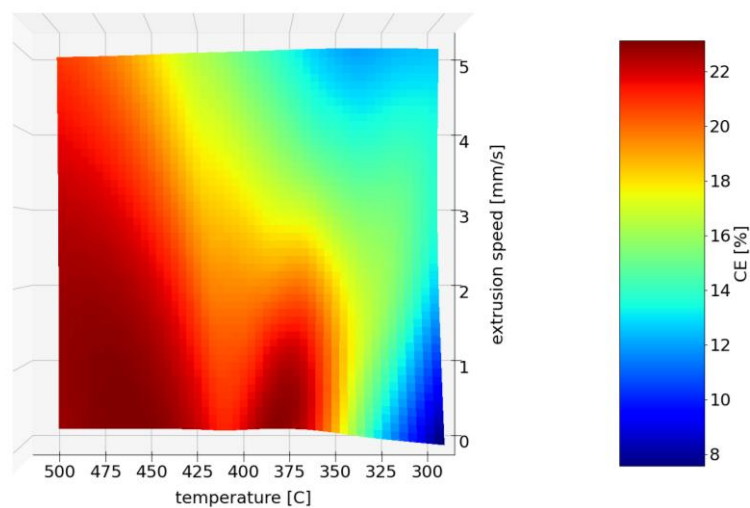


Figure 30 Map showing the process-property mapping for 1% Gd for compressible elongation.

As KPI for this Success Story the isotropicness of the material was chosen represented by the characteristic number of the ratio between the tensile yield strength and compressible yield strength with a perfect isotropic material to be assumed to have yield ratio of 1.

Based on this assumption we can now choose process properties which result in a predicted yield ratio of 1. Resulting in a map of gadolinium, extrusion speed and temperature for which this yield ratio is predicted. Figure 31 shows the results for $2\sigma < 0.03$ and $TYS/CYS=1\pm 0.025$. By limiting the variance σ in the ensemble model prediction only reliable predictions are used. As can be seen with the increasing gadolinium content the extrusion speed and temperature for isotropic behavior decreases.

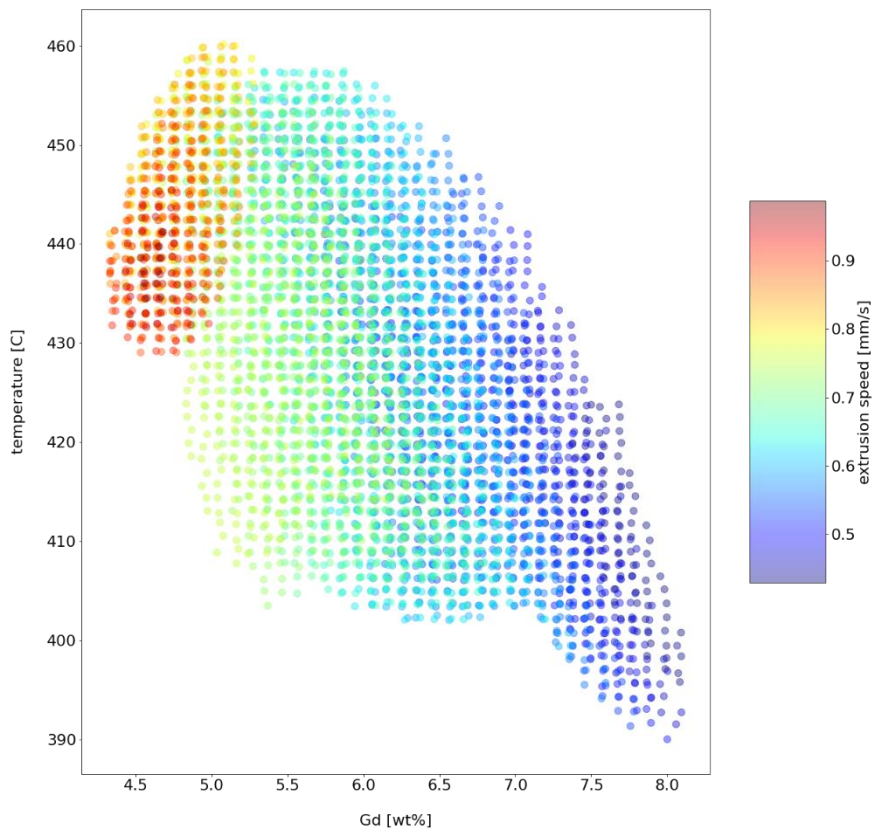


Figure 31: Map showing process parameters for which isotropic behavior ($TYS/CYS=1$) is predicted by the ML model with $2\sigma < 0.03$ and $TYS/CYS=1\pm 0.025$.

3.4.1.1 MODELS

Machine Learning Model

To perform regression tasks on the process parameter space of Gadolinium concentration, extrusion temperature and extrusion speed, a single layer feedforward network was implemented using pytorch v1.13. This network architecture consists of a linear input layer with bias, a linear hidden layer with bias, a LeakyReLU activation function, a LayerNorm normalization layer and a linear output layer with bias.

The training data set consisted of only 33 samples, so we augmented it by adding uniformly distributed noise. We optimized the noise level from 0.5% to 10% in 0.5% increments and the number of additional samples from 0 to 20 times the original size. The optimal settings were 2% noise and two extra samples per original sample, which minimized the mean squared error (MSE) for the training data. We then tuned the hyperparameters of the neural network, such as the number of epochs, the learning rate, and the hidden layer size. We used an adaptive gradient descent algorithm called AdamW and a summed absolute error as the loss function. The best performance on the training data was achieved with 2000 epochs, a learning rate of $1e-4$, and a hidden layer size of three times the input layer size. To estimate the uncertainty and improve the accuracy of our predictions, we used ensemble averaging with an ensemble size of 20. We excluded models with a loss value higher than 150% of the mean loss value for each output property from the ensemble prediction and used them only to calculate the variance.

3.4.1.2 SOFTWARE TOOLS

Pytorch

PyTorch is a deep learning framework that combines a user-friendly front-end with a powerful back-end. PyTorch enables fast, flexible experimentation and efficient production through features such as:

- Automatic differentiation: PyTorch uses a tape-based system to compute gradients for tensors and neural network layers, allowing for dynamic and customizable computation graphs.
- Distributed training: PyTorch supports data parallelism and model parallelism across multiple GPUs and CPUs, enabling scalable and efficient training of large models.
- Mobile deployment: PyTorch supports an end-to-end workflow from Python to deployment on iOS and Android devices, with tools for preprocessing and integration of machine learning models in mobile applications.
- TorchScript: PyTorch provides a seamless transition from eager mode to graph mode, where models can be optimized, serialized, and run in C++ runtime environments for speed and performance.
- Ecosystem of tools and libraries: PyTorch is compatible with a rich set of libraries and tools for computer vision, natural language processing, audio processing, reinforcement learning, and more.
- Cloud support: PyTorch is well supported on major cloud platforms such as AWS, Google Cloud Platform, Microsoft Azure, etc., providing frictionless development and easy scaling.

PyTorch is an optimized tensor library for deep learning using GPUs and CPUs. It also provides accelerated NumPy-like functionality for scientific computing. PyTorch is one of the most popular frameworks among researchers and developers due to its flexibility, simplicity, and expressiveness.

Scikit-learn

Scikit-learn is a Python module for machine learning that provides simple and efficient tools for predictive data analysis. It is built on top of NumPy, SciPy, and matplotlib, and it is open source and commercially usable under the BSD license. Scikit-learn offers various features such as classification, regression, clustering, dimensionality reduction, model selection, and preprocessing. It also has a comprehensive documentation with tutorials, examples, and user guides. Scikit-learn is one of the most popular and widely used machine learning libraries in Python.

3.4.2 INPUT/OUTPUT/BACKWARDS PROCESSES

The description of key inputs and outputs per simulation step is summarized in Table 5, also describing the backward process starting from the desired output propagating back to the required input

Table 5: Summary of input/output data for Success Story 4

	Input [IN] / Output[OUT]	Value type/ File extension	Description
Process parameter-property prediction			
OUT	ML Model	pt	Trained ml model
	KPI maps	svg/png	Maps showing the process parameter space for the chosen KPI
	Training process		
IN	Process parameter space	config	Process parameter space definition.
	Material measurements	json csv	All measurement samples that are supposed to be used for the model training.

3.4.3 CHALLENGES AND GAPS ANALYSIS

One of the limitations of the current study is the scarcity of data points that can be used to validate and refine the proposed model. The existing measurements are not sufficient to capture the full range of variability and uncertainty in the system parameters and inputs. Therefore, a more comprehensive data collection effort is underway to obtain a larger and more representative sample of experimental results. These data will enable the development and testing of a more advanced version of this application that can account for more complex phenomena and scenarios.

3.4.4 VALIDATION AGAINST EXPERIMENTAL DATA/ MEETING KPI

To ensure the reliability and accuracy of our results, we have conducted additional measurements on the samples, and we plan to perform more tests in the future. These measurements include different loading conditions, strain rates and temperatures. We also aim to develop a more advanced version of our model that can capture the nonlinear and anisotropic behavior of the material and a wider range of alloys. The key performance indicator (KPI) that we use in this first model is the ratio of the tensile and compressive yield strength. This ratio has been shown to be a good indicator of isotropic behavior.

3.4.5 BENEFITS OF OIP PLATFORM

The Open Innovation Platform (OIP) is a powerful tool that can handle diverse and heterogeneous data sources in a seamless way. By using ontology-based tools, the OIP can create a common semantic framework that can link and harmonize different data models and vocabularies from various domains and applications. This enables the OIP to execute sophisticated verification and data generation workflows that can combine both data-driven and physics-based models in an integrated manner. The OIP can then use these workflows to generate innovative solutions for complex KPIs that require multi-disciplinary approaches. For instance, the OIP can use experimental data from sensors or measurements to calibrate or validate a simulation model that represents a physical system or process. The OIP can then use this simulation model to optimize its performance and efficiency by exploring different scenarios or parameters. This way, the OIP can leverage the best of both worlds: the accuracy of physics-based models and the flexibility of data-driven models.

3.5 SUCCESS STORY [5] – DIGITAL POWDER TESTING (CMCL)

The automotive industry has been actively seeking new technologies to reduce harmful emissions and improve overall efficiency. One of the key components in achieving this goal is the development of advanced catalysts that can effectively convert harmful exhaust gases into less harmful substances. This story report highlights the successful development of an end-to-end digital solution for multi-stage catalytic powder testing in the creation of a Three-Way Catalyst (TWC). TWC is designed to convert carbon monoxide (CO), unburnt hydrocarbon (uHC) and nitrogen oxide (NO_x) in the exhaust of gasoline-fuelled engine to carbon dioxide (CO₂), water (H₂O) and nitrogen (N₂). The main goal of the preliminary execution of this Success Story is to develop an end-to-end digital solution for the multi-stage catalytic powder testing, ranging from catalyst material testing in laboratory to vehicle-level real driving conditions, as shown in Figure 32.

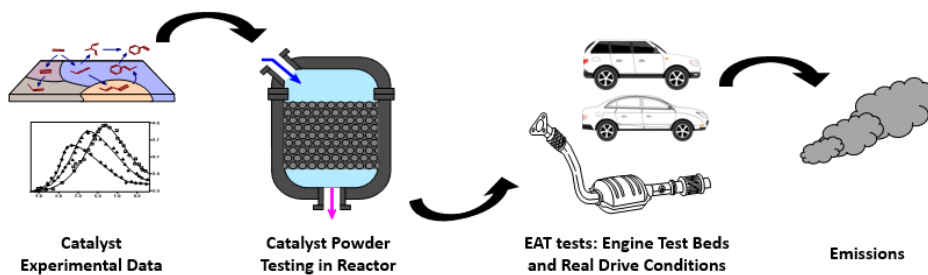


Figure 32: Use-case processes overview.

3.5.1 MODELLING AND SIMULATION WORKFLOW FOR OFF-LINE EXECUTION

The Three-Way Catalyst (TWC) is a widely used exhaust after-treatment (EAT) device in gasoline-fuelled engines that reduces harmful emissions before they are released through the vehicle's tailpipe. The performance of a TWC is largely dependent on the catalytic material used, which is characterised by its composition and micro-structural properties.

To identify the best candidates for catalyst powders, multiple testing stages are required, including laboratory characterisation, steady-state testing, and drive-cycle testing. These stages demand considerable effort, often hindering the introduction of new products to the market and increasing associated costs. The material selection process can be significantly streamlined if it is digitalised, thereby reducing the number of required experiments, and accelerating the development of more effective catalysts.

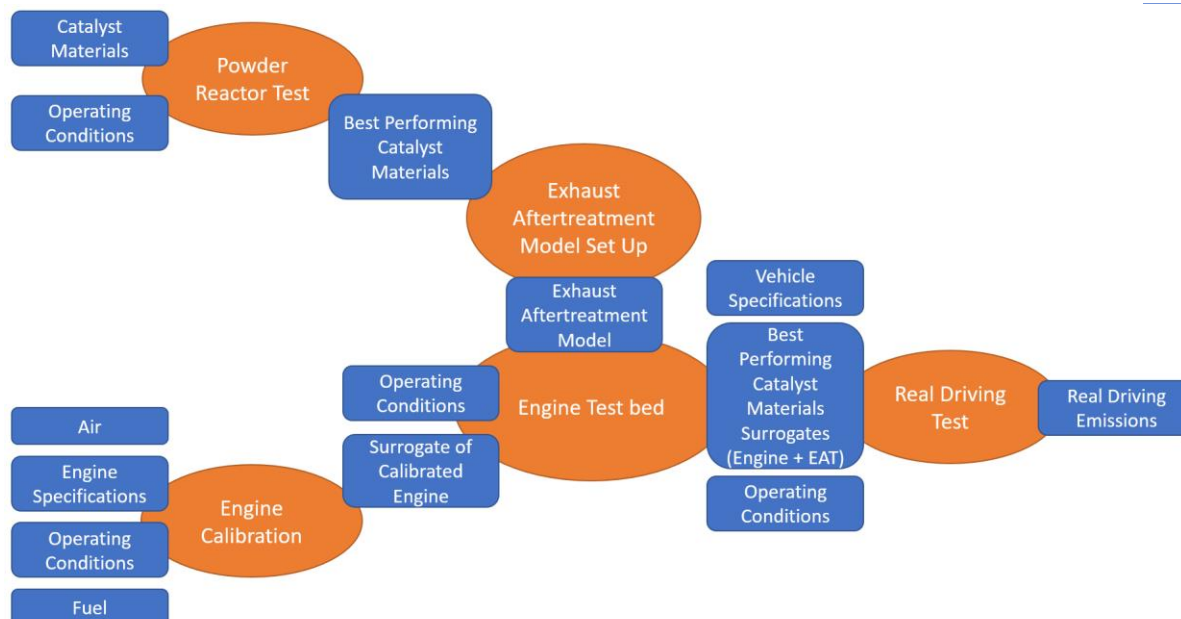


Figure 33: Catalyst powder testing process overview.

Figure 33 shows the stages and notable inputs/outputs of the catalyst powder development process. To perform the above workflow digitally, three software products offered by CMCL are used in this Success Story, including:

6. The SRM Engine Suite (**SRM**): a virtual engineering design tool for simulating the performance and exhaust gas emissions from internal combustion engines. It is applied to predict engine-out emissions in this Success Story.
7. **kinetics**: a software tool for building, designing, maintaining, and applying chemical kinetics reaction models to engineering applications in the automotive, energy, and chemical processing industries. It is applied to simulate the performance of TWCs in this Success Story.
8. The Model Development Suite (**MoDS**): an advanced software tool designed to simplify the model development process. It is used to calibrate the engine model and to produce surrogate models in this Success Story.

By leveraging these software products, the catalyst powder development process can be effectively digitalized, streamlining the workflow and accelerating the development of new and improved TWCs.

The digital workflow and software tools employed in this Success Story have been outlined, and now the focus shifts to the specific steps that constitute the catalyst powder development process. These steps include engine model calibration, engine surrogate model generation, TWC laboratory testing simulation, engine test bed simulation, TWC surrogate model generation, and drive cycle testing simulation. The following sections will discuss each of these crucial stages in detail, highlighting their importance in creating a coherent and efficient digital approach to catalyst powder development. This comprehensive examination will demonstrate how the digitalization of these steps contributes to a streamlined workflow, ultimately leading to the accelerated discovery and implementation of more effective TWCs.

Engine model calibration

A reliable engine model is necessary for testing the performance of catalyst material candidates under realistic conditions. In this work, CMCL's toolkit SRM is applied as the high-fidelity physio-chemical simulator within the digital workflow, with MoDS used to perform parameter estimation, model validation, and surrogate model generation (see Figure 34). The workflow has demonstrated its predictive capabilities in many applications of internal combustion engine modelling in real-world industrial settings.

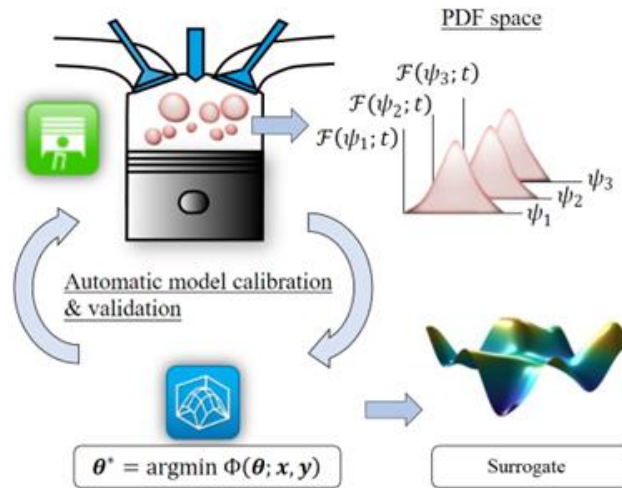


Figure 34: A schematic diagram for Digital Engineering workflow for IC engine modelling

The SRM is based on a probability density function (pdf) transport equation for turbulent combustion, which calculates random scalar variables for chemical species and temperature over time. A two-zone technique is employed for simulating spark-ignited combustion, dividing the total number of stochastic particles into unburnt and burnt zones. The ignition event initiates in the unburnt zone, and as stochastic particles transition from the unburnt to the burnt zone, flame propagation determines burn rates. The SRM's internal chemical surrogate mechanism is utilised to simulate gasoline, featuring oxidation chemistry for Toluene, n-Heptane, Ethanol, and iso-Octane (THEO) and primary emission pathways for NO_x and soot precursors. Five input sets with varying operating conditions include engine speed, load, intake temperature, inlet pressure, and spark timing (see Figure 35). The resulting outputs include in-cylinder pressure and engine-out gas phase emissions, including NO_x and uHCs.

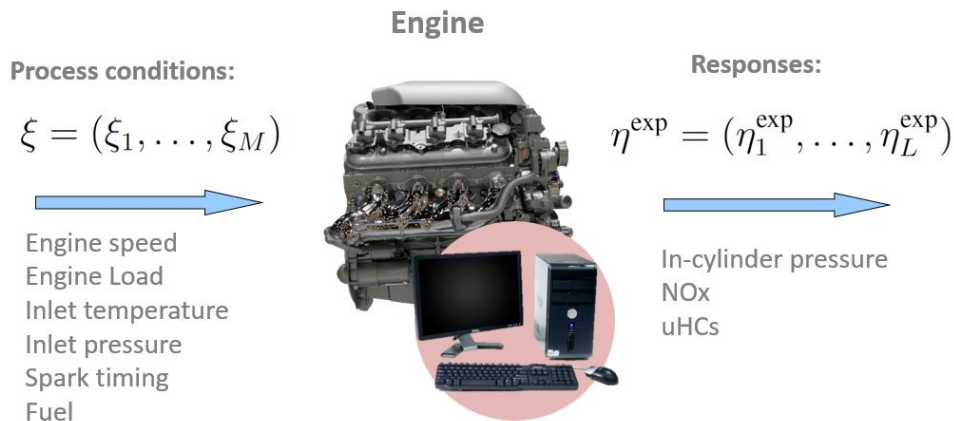


Figure 35: Inputs for the engine modelling, and the corresponding outputs.

MoDS is employed to estimate optimal values for several SRM model inputs, aligning with experimental measurements of in-cylinder pressure profiles and emissions. Four sets of parameters are calibrated: turbulent mixing, flame propagation, heat transmission, and emissions multipliers. The heat transfer model governs heat flux between the combustion chamber surface and the cylinder charge. Turbulent mixing parameters are constants in the k-turbulence transport equation, while flame propagation parameters alter the premixed flame characteristics. Emissions multipliers serve to fine-tune the measurement. MoDS independently calibrates the complete set of input values.

Each MoDS run consists of the following stages:

1. Coarsely sample the input parameters space by evaluating the SRM at $2^{N_{\text{input}}+1}$ Sobol points.
2. Identify the Sobol point with the lowest objective function to establish the initial values of model parameters.
3. Execute a local optimisation using the Hooke and Jeeves algorithm to minimise the objective function, representing the discrepancy between model predictions and experimental measurements.

Engine surrogate model generation

Whilst the calibrated physics-based engine model can simulate the behaviour of actual engines accurately, it is relatively computationally expensive. An engine surrogate model is therefore generated from results of the calibrated SRM engine model to significantly reduce simulation time with minimal loss of accuracy.

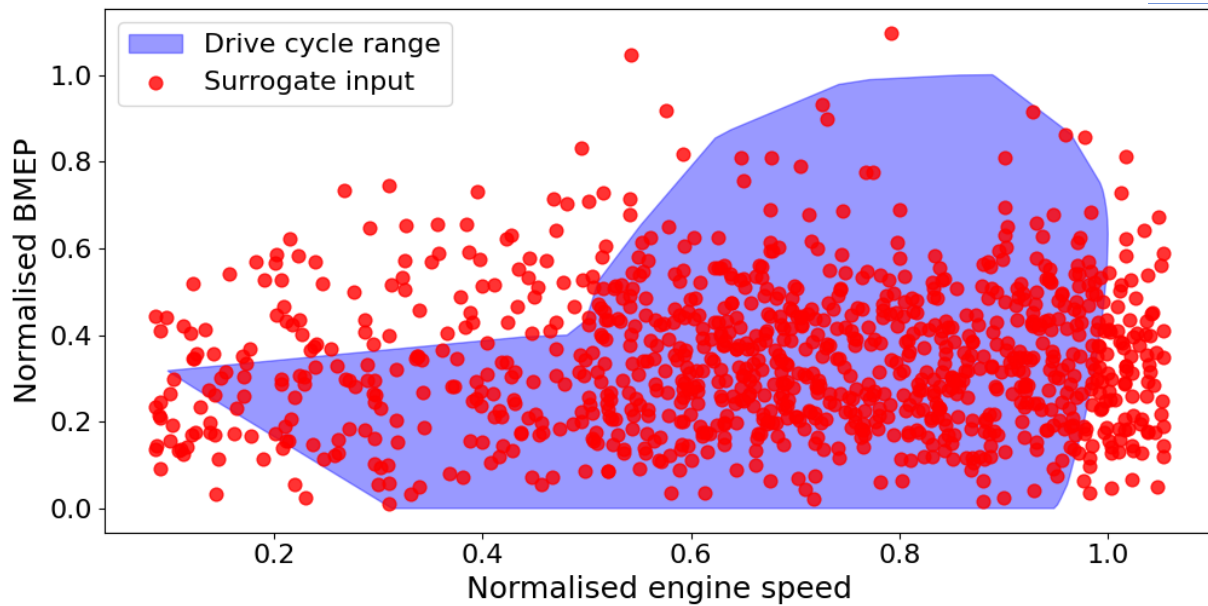


Figure 36: Inputs of the engine surrogate model need to cover the range of conditions that would occur during drive cycle testing.

An example of SRM simulations that are used to generate the engine surrogate model are shown as red circles in Figure 36. The range of operating conditions that would occur during the drive cycle test is shaded in blue. It is important to ensure that the input to the surrogate model covers the entire operating range sufficiently, otherwise the engine surrogate model would be extrapolating and that could lead to large errors.

The steps of this workflow are:

1. Randomly generate operating conditions of SRM model, which sufficiently covers the desired range.
2. Conduct simulations using the SRM and previously calibrated model parameters.
3. Post-process SRM simulation results and prepare inputs for MoDS, including inputs and outputs of the engine surrogate model.
4. Utilise MoDS to fit an engine surrogate model.

TWC laboratory testing simulation

Candidates of catalyst material are first tested in laboratory settings. In this Success Story, all candidates are tested virtually as per experiments conducted by Chatterjee et al. [18] using kinetics. The TWC is modelled by an one-dimensional flow reactor with empirical correlation to capture convective mass transfer. The reaction-diffusion phenomenon is considered by coupling the TWC model with an effectiveness factor model. The performance of the TWC with different catalyst materials are simulated for three typical inlet conditions namely “Lean”, “Stoichiometric” and “Rich” between 400 K and 900 K. The conversion efficiencies of CO, uHC (represented by C_3H_6 in the model) and NO are reported and can be used as criteria of material selection.

The steps of this workflow are:

1. Set up the TWC model with known dimensions/parameters e.g. the diameter of the TWC, the wall thickness.
2. Specify the material properties of the catalytic sample.

3. Execute kinetics with changing operating conditions i.e. different inlet compositions and temperatures
4. Post-process the outlet composition reported by kinetics and calculate the conversion efficiencies of pollutants

Engine test bed simulation

After assessing the performances of catalyst samples with the laboratory settings, they are further tested with exhausts from the engine operating at steady-states. The engine surrogate model is used to generate 50 random operating points as inlet conditions for the steady-state testing. It should be noted that the SRM engine model (and hence the surrogate model) only considers events that occur within the engine cylinders. In practice, the cylinder-out exhaust will first pass through other engine components before reaching the inlet of the TWC. The inlet temperature of the TWC is usually lower than that of the cylinder-out exhaust due to significant heat loss. In this work, the heat loss is estimated based on literature experimental data of a small-size gasoline-fuelled engine [3], where the ratio of sensible heat in the exhaust to the total fuel energy is reported as a function of engine load and engine speed and is used to estimate the inlet temperature of the TWC from the outlet temperature of the engine cylinders provided by the engine surrogate model.

The steps of this workflow are:

1. Randomly generate 50 operating points within the range of WLTC.
2. Call the engine surrogate model to predict the cylinder-out composition, flow-rate and temperature for the random operating points.
3. Estimate the inlet temperature of the TWC using literature data and surrogate model output.
4. Specify the dimensions of the TWC. These parameters will remain fixed from this point.
5. Update the operating condition inputs and execute kinetics to simulate the TWC behaviour with different catalytic material.
5. Post-process the outlet composition reported by kinetics and calculate the conversion efficiencies of pollutants.

TWC surrogate model generation

The simulation results of the engine test bed are used to generate TWC surrogate models for fast evaluation of drive cycle performance. In addition to the existing simulation results, further simulations are performed with the same composition and flow-rate of the steady-state engine exhaust, but at lower temperatures. This is necessary for the TWC surrogate models to capture the cold-start behaviour at the beginning of the drive cycle test, where the TWC have not warmed up yet.

The steps of this workflow are:

1. Change the inlet temperature of the TWC model and execute kinetics for each catalytic material.
2. Collate simulation results of kinetics and prepare the input for MoDS; the inlet conditions of the TWC will be the input of the TWC surrogate model and the outlet composition will be the output of the TWC surrogate model.
3. Use MoDS to fit one TWC surrogate model for each catalytic material.

Drive cycle testing simulation

After catalyst candidates pass the laboratory test and engine test bed, it is important to check their performance in a real world setting, hence a drive cycle test. During the drive cycle test, the temperature of the TWC will not be the same as the inlet temperature due to thermal inertia of the TWC i.e. it takes time for the TWC to reach the same temperature as the inlet, assuming no heat loss to the environment. Assuming that the heat of reaction in the TWC is negligible, the temperature evolution in the TWC would be independent of the catalyst sample. The thermal behaviour of the TWC during the drive cycle test is simulated using kinetics. Tailpipe emissions of catalyst samples are estimated by the TWC surrogate models after the inlet composition, flow-rate and temperature are supplied as inputs.

The steps of this workflow are:

1. Supply engine speed and load during the drive cycle test as functions of time to the engine surrogate model as inputs.
2. Call the engine surrogate model to estimate the cylinder-out exhaust properties.
3. Account for heat loss between the engine cylinders and the inlet of the TWC using literature data.
4. Specify the inlet flow-rate and temperature of the TWC model during the drive cycle test.
5. Execute a **non-reactive** TWC simulation in kinetics, which would report the temperature evolution within the TWC during the drive cycle test.
6. The simulated temperature is supplied to the TWC surrogate models (of catalytic materials) together with inlet composition and flow-rates.
7. Call MoDS to execute the TWC surrogate models of each catalytic materials and predict the tailpipe emission composition.
8. Post-process the result and report to user.

3.5.2 INPUT/OUTPUT/BACKWARDS PROCESSES

The data dependency of the workflow is shown in Figure 37. The desired output is the tailpipe emissions of regulated pollutants during a drive cycle test. A TWC model and inputs to the model are needed. The inputs of the TWC model can be split into the following groups:

- Dimensions: Monolith length [m], Monolith diameter [m], wall thickness [mm], cell density [$1/m^2$]
- Material properties: Catalyst coverage [-], washcoat thickness [micron], Pore diameters [nm], Washcoat porosity [-], Tortuosity [-]
- Operating condition: Inlet mass flow rate [kg/s], Inlet mixture composition [-], Temperature [K], Pressure [Pa]
- Model parameters: reaction rate constants [varies]

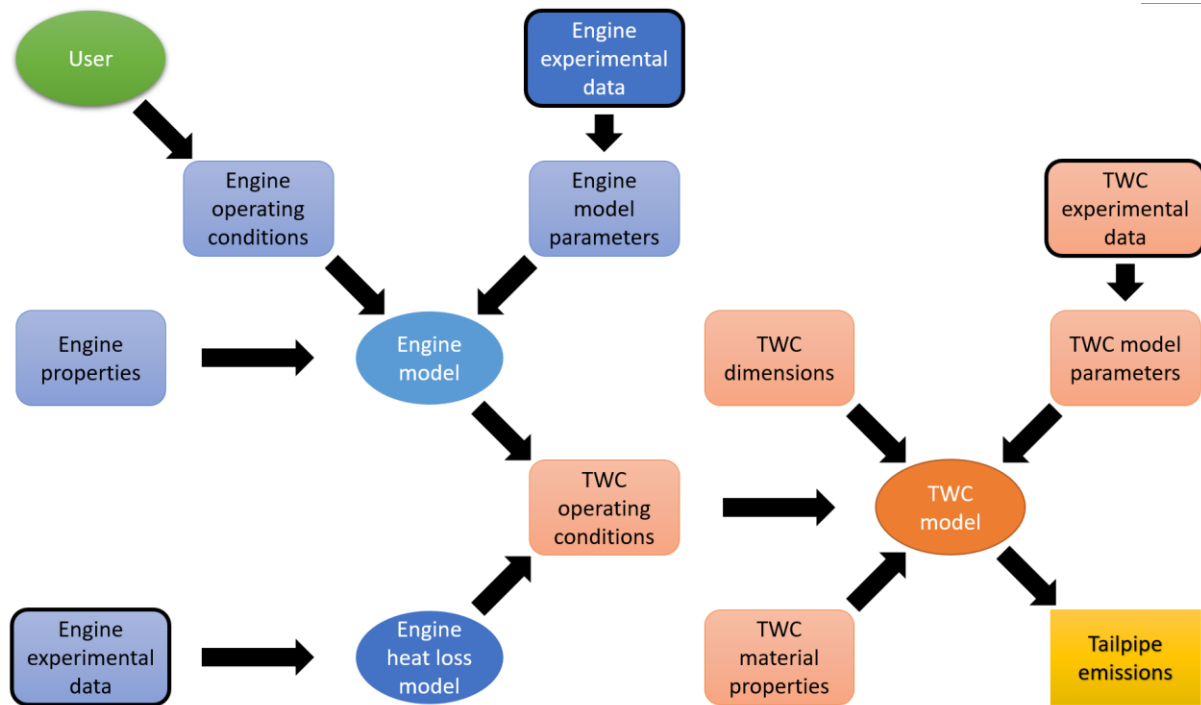


Figure 37: Data/model dependency of the workflow.

The dimensions of the TWC are either known (in the case of laboratory testing) or treated as fixed design parameters (for engine test bed & drive cycle test). The material properties are specific to each catalytic material candidate. The operating conditions are either known (in the case of laboratory testing) or provided by an upstream model parameters (for engine test bed & drive cycle test). The model parameters can be calibrated against experimental data; in this case the values reported by Chatterjee et al. [18] are used directly.

In order to enable fast simulation, TWC surrogate models are generated using MoDS from the simulation outputs of the physics-based TWC model in kinetics. Only the operating condition inputs can be changed for the TWC surrogate models; the rest of input parameters are “frozen” once a surrogate model is generated.

The operating condition of the TWC is dependent on the outlet of the engine cylinders i.e. outputs of the engine model. The input parameters of the engine cylinder model are:

- Dimensions: Cylinder volume [L], Bore length [mm], Stroke length [mm], Con Rod Length [mm], Compression Ratio [-], Wrist Pin Offset [mm], Crevice Ratio [%], Number of cylinders [#]
- Operating condition: Engine speed [RPM], Intake temperature [K], Intake pressure [bar], EGR [%], Spark timing [CAD], Injection timings [CAD], Injected fuel mass[mg], fuel composition [-]
- Model parameters: turbulent mixing parameters, flame propagation parameters, heat transmission parameters, emissions multipliers

The model parameters of the engine model are calibrated based on experimental data of engine tests using MoDS, whereas dimensions and operating conditions are known/provided by the user. Like the treatment of the TWC, an engine surrogate model is generated based on the calibrated SRM model to estimate cylinder-out emissions. The engine surrogate model can accept different operating conditions as inputs whilst other input parameters are fixed once the surrogate model is generated.

It should be noted that the physics-based engine model and the engine surrogate model have different inputs and outputs. The SRM engine model requires the timing and the amount of fuel injection as inputs, and it predicts the engine load (BMEP/Torque) as an output. On the other hand, the engine surrogate model takes the engine load as an input (it is possible since the surrogate model is purely data-driven). Furthermore, a heat loss model is needed to calculate the inlet temperature of the TWC since it should be lower than that of the outlet temperature of the engine cylinders. In this work this is estimated based on literature data of similar engine systems [19].

The user is required to provide the engine speed and engine load for the engine test bed and drive cycle test i.e., the operating conditions to the engine surrogate model.

3.5.3 CHALLENGES AND GAPS ANALYSIS

The main challenge of this Success Story is the scarcity of available data:

9. One of the difficulties that had to be overcome is the fact that most of the high-quality catalyst materials data is proprietary, thus unavailable for the Success Story execution.
10. Another complication is the fact that the proposed digital powder testing workflow requires the knowledge of the materials surface kinetics in a form of chemical mechanism.
11. The heat loss between the outlet of engine cylinders and the inlet of TWC is not simulated in the current workflow.

The challenges presented in this Success Story are addressed in the following way. The platinum-rhodium Three Way Catalyst (Pt/Rh TWC) studied by Chatterjee et al. [18] is selected for this Success Story, where a chemical mechanism of the catalyst has been calibrated and validated by Chatterjee et al. [18] against experimental data. The heat loss between the outlet of engine cylinders and the inlet of TWC is estimated based on literature experimental data of similar engine systems [19].

3.5.4 VALIDATION AGAINST EXPERIMENTAL DATA/ MEETING KPI

In this section, the performances of models included in the workflow are validated against experimental data where available. An example run is reported to demonstrate the capability of each part of the workflow.

Engine cylinder model validation

A synthetic dataset for a gasoline direct-injection spark-ignition (GDI-SI) engine is used to verify the capability of the engine model. Figure 38 illustrates the details of the 19 engine operating conditions in terms of the range of engine speeds and loads, with the IMEP normalised by a reference value. Each load-speed point includes distinct measurements of in-cylinder pressure profiles in terms of crank angle degree, as well as engine-out emissions, including NO_x and uHCs.

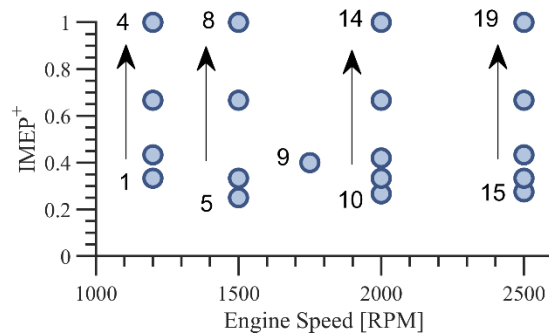


Figure 38: A representative set of 19 operating points on the engine load-speed window. The case ID is presented as the number next to the operating point. The arrows indicate the increment direction of the case ID.

Once the SRM has been calibrated for the specified cases, the input values are fixed in place (independently for each DoE dataset). The model is then tested with an additional 20 sets of synthetic data. This validation procedure helps determine the model's predictive capabilities.

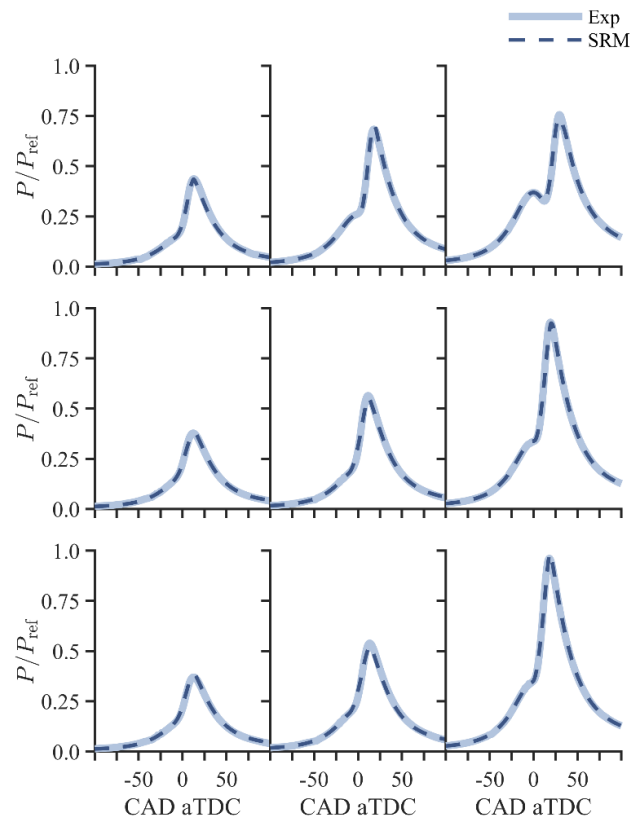


Figure 39: Calibrated pressure profiles for 9 pure gasoline load-speed points at 1200 rpm (top), 2000 rpm (mid), 2500 rpm (bottom), and increasing IMEP⁺ (in left to right direction).

Figure 39 compares the calibrated normalised in-cylinder pressure from the SRM and the measurement data at different selected load-speed points, where the pressure P is normalised by a reference pressure P_{ref} for all cases. The engine speed varies from low to high (1200, 2000, and 2500 rpm), and the corresponding IMEP ranges from low (IMEP⁺ ≤ 0.3) to medium (IMEP⁺ ≈ 0.5) to high (IMEP⁺ = 1.0). The calibration algorithm identifies the

minima in the goal function to obtain in-cylinder pressure that adequately fits the experimental data for the pressure increase, peak, and expansion stroke. Figure 39 demonstrates a satisfactory outcome achieved through the pressure calibration process.

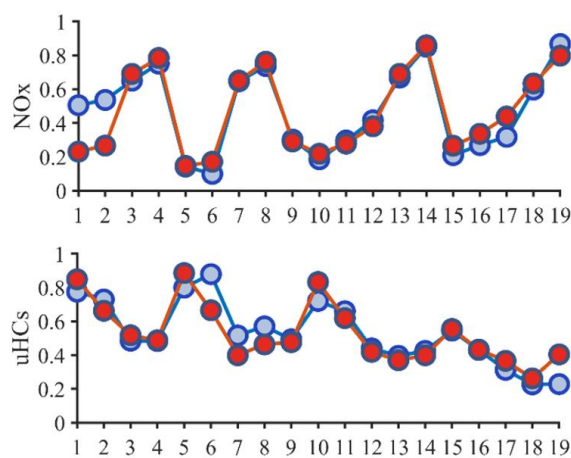


Figure 40: Experiment vs SRM Engine Suite for NO_x and uHCs.

The calibration results for the concentrations of NO_x (NO + NO₂) and uHCs can be seen in Figure 40. The maximum measurement value is used to normalise the magnitudes of the simulated and actual data. There is a comparison between the model and the experimental data based on the case ID. The calibrated results match the measured values adequately.

Nitrous oxide emissions are mostly composed of NO and NO₂ species, which are generated because of out-of-equilibrium chemical processes that are driven by the kinetics of the reactions involved. The THEO chemical kinetic mechanism integrated within the SRM Engine Suite provides the chemical species as well as a sufficiently precise description of the chemical pathway that leads to the creation of nitrous oxide emissions (i.e., thermal NO). As a result, the engine modelling approach provides a confidence in the input composition for the subsequent EAT modelling.

TWC model validation

The capability of kinetics to simulate a TWC is verified in this section. The chemical mechanism of a platinum-rhodium TWC developed by Chatterjee et al. [18] is used in this work. They calibrated the chemical mechanism against experimental data of a laboratory flat-bed reactor using a two-dimensional (cylindrical coordinate) CFD model coupled with their own chemical modelling tool. In this work, kinetics is used to simulate the flat-bed reactor with Chatterjee's mechanism. The flat-bed reactor is described by a series of control volumes in the axial direction of the TWC. The reaction-diffusion phenomenon that occurs across the catalyst washcoat is captured by the effectiveness factor model.

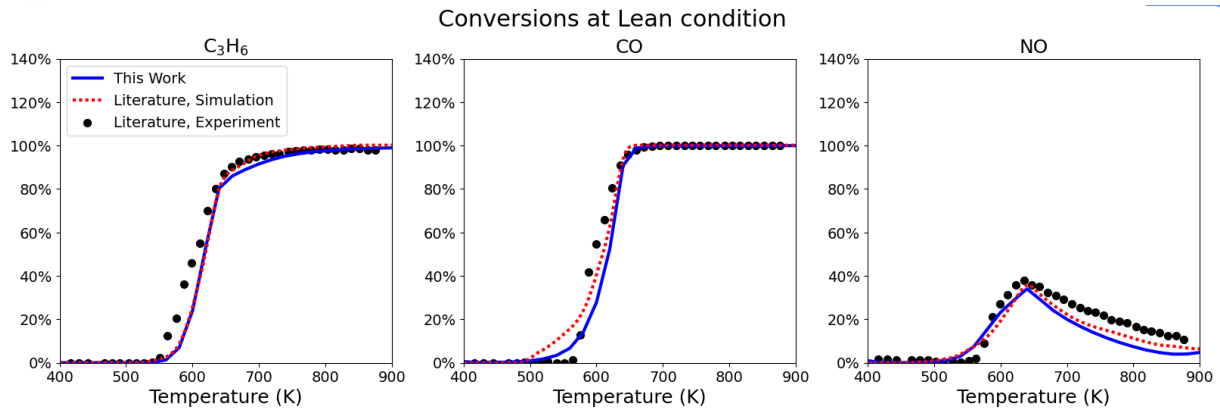


Figure 41: Experiment vs kinetics for TWC conversion at lean condition.

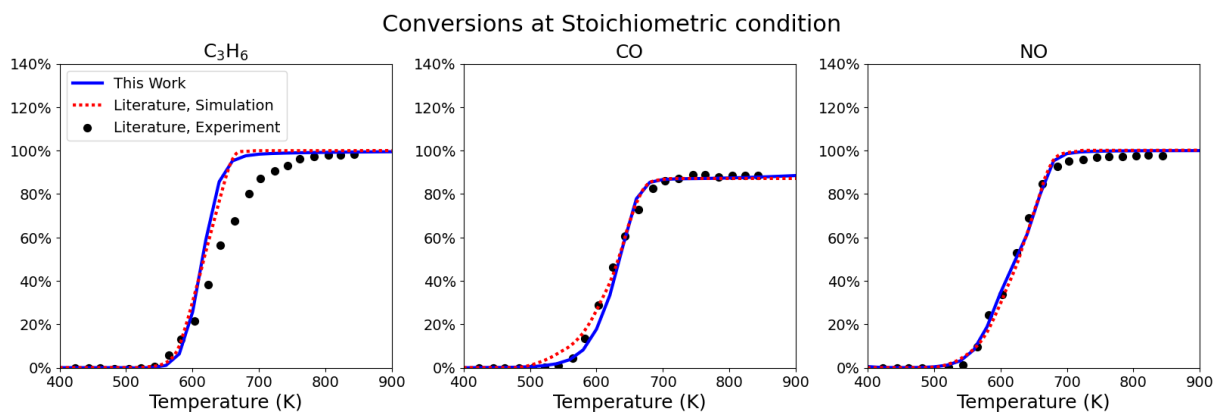


Figure 42: Experiment vs kinetics for TWC conversion at stoichiometric condition.

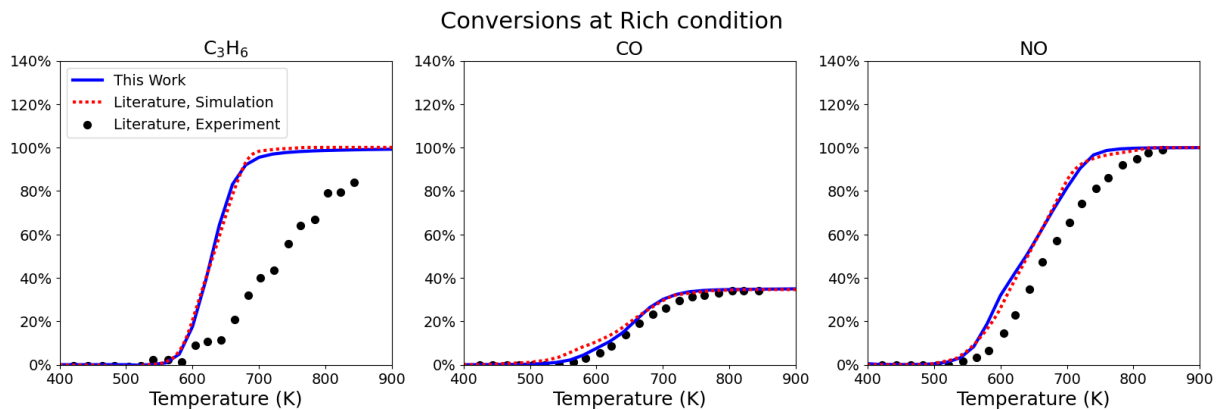


Figure 43: Experiment vs kinetics for TWC conversion at rich condition.

The comparison between literature experimental data, literature simulation data and results of kinetics are shown in Figure 41, Figure 42 and Figure 43 for three typical operating conditions, namely “Lean” (high oxygen content), “Stoichiometric” and “Rich” (low oxygen content). Good agreement between the simulation results of literature model and kinetics can be observed.

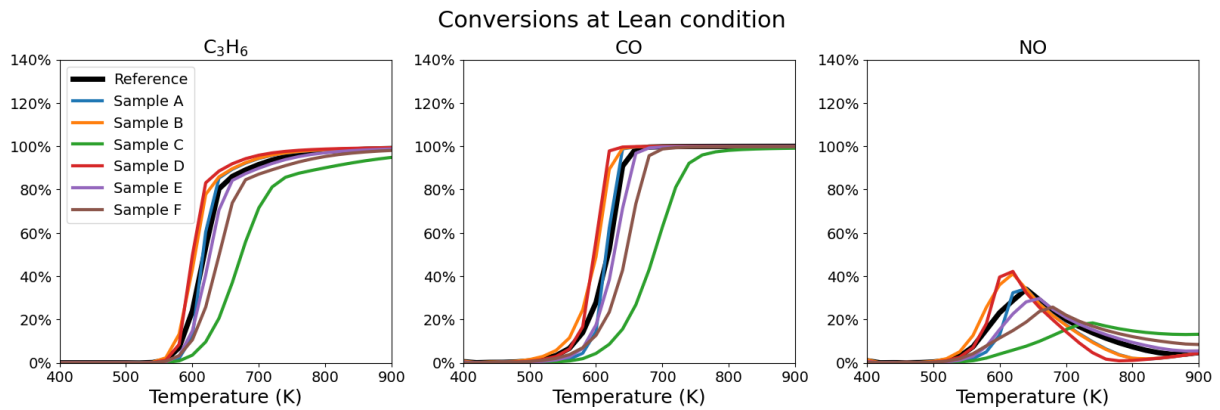
TWC laboratory testing simulation


Figure 44: Conversion of various TWC samples at lean condition, literature experimental condition [18].

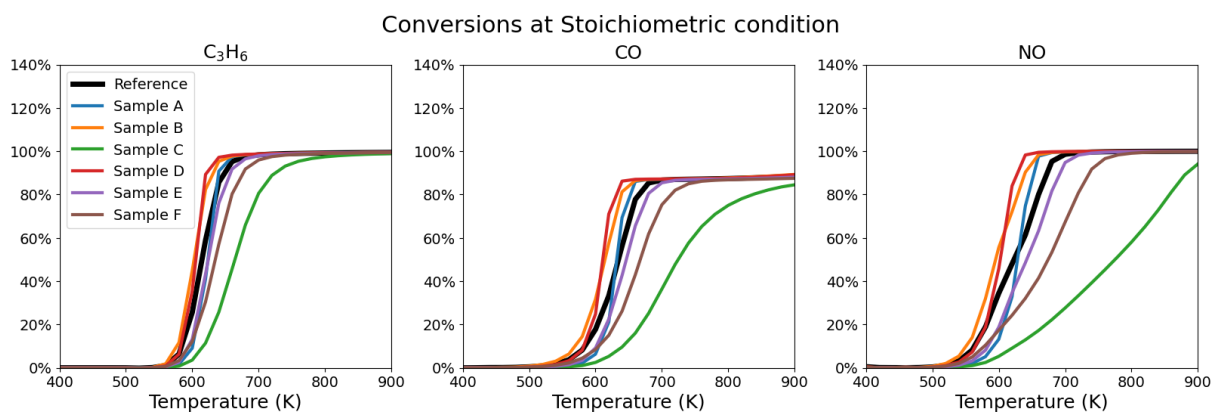


Figure 45: Conversion of various TWC samples at stoichiometric condition, literature experimental condition [18].

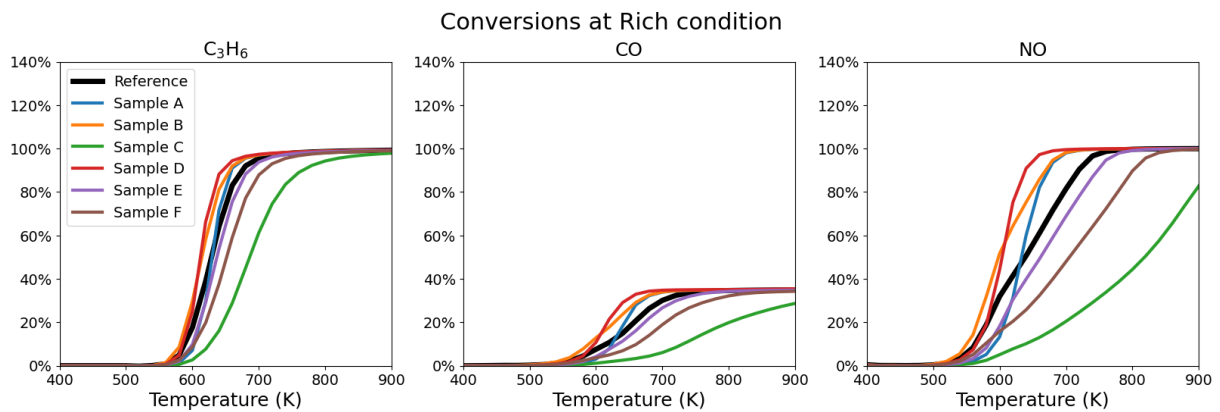


Figure 46: Conversion of various TWC samples at rich condition, literature experimental condition [18].

After both the physics-based engine model and the TWC model are validated against experimental data, six synthetic catalytic materials are tested to demonstrate the execution of the workflow. The performances of the catalyst samples in laboratory testing are shown in Figure 44, Figure 45, and Figure 46. Some general trends may be observed; sample C, E, and F are less effective than the reference catalyst under most conditions

whereas sample A, B, and D generally performs better than the reference catalyst. For demonstration purposes, no material selection is presented in this report.

Engine surrogate model generation

After testing catalyst material candidates with typical inlet conditions in laboratory settings, they should be further tested under more realistic and stringent conditions i.e. the engine test bed and drive cycle testing. These tests would require the knowledge of the engine-out emissions. These can be provided by the calibrated SRM model. In order to reduce the simulation time required to perform many simulations with the SRM model, an engine surrogate model is generated using MoDS. The predicted engine-out CO emissions are shown in Figure 47 as an example. 50 operating points are selected randomly as the inlet conditions to the TWC on the engine test bed.

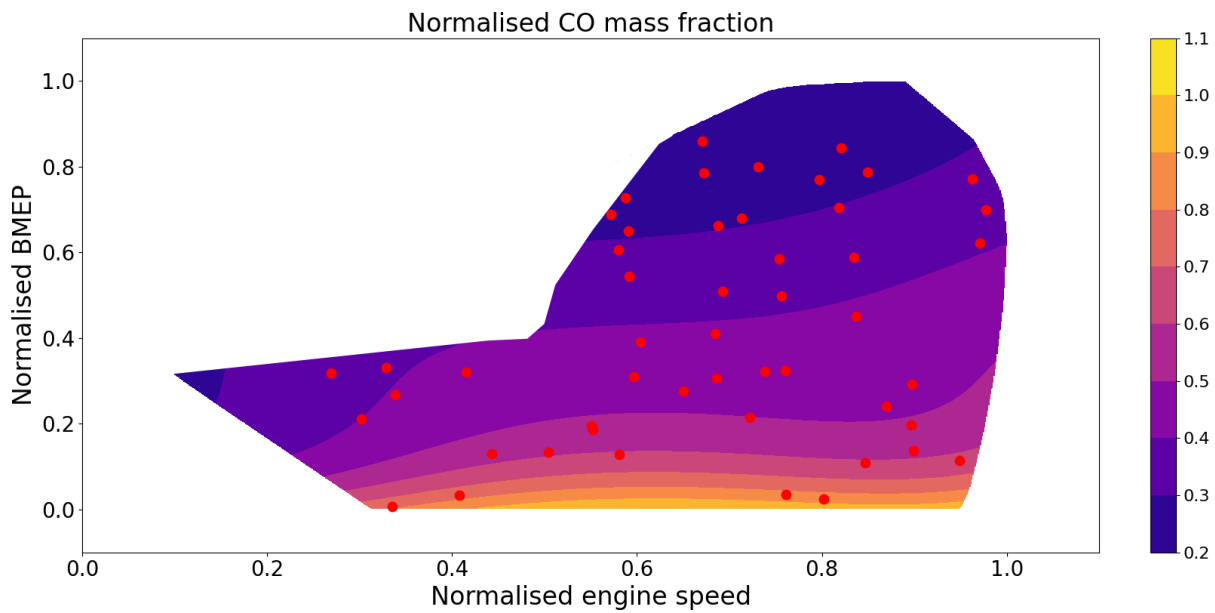


Figure 47: Inputs of the TWC steady-state testing generated by the engine surrogate model.

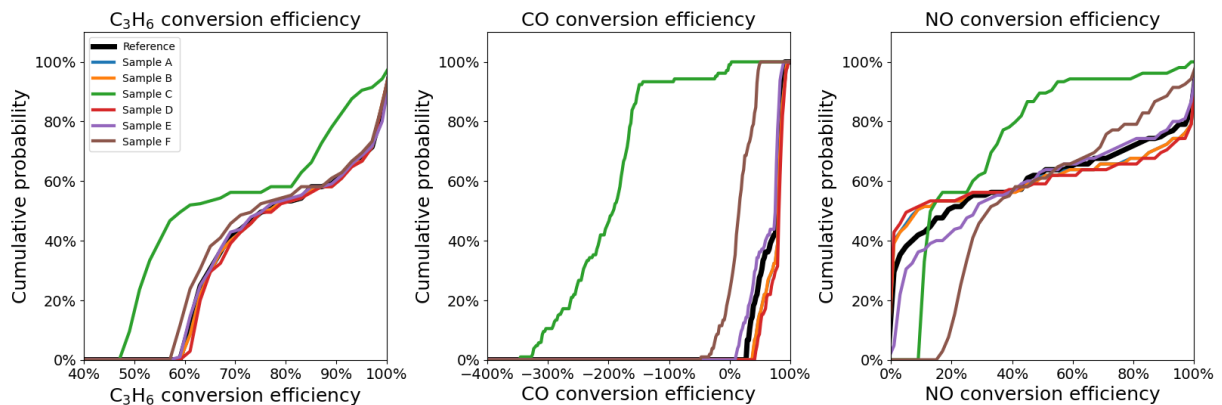


Figure 48: results of TWC testing with engine test bed.

The results of 50 cases of the engine test bed are shown as cumulative distribution functions in Figure 48. Under certain operating conditions, there is more CO at the outlets of sample C and sample F than at the inlets. This is likely to be caused by the faster, incomplete C_3H_6 oxidation and the slower CO oxidation. On the other hand, sample C has the best NO conversion performance. These outputs can be valuable to the material selection process.

Drive cycle testing simulation

The engine surrogate model is used together with the engine heat loss model to provide the inlet conditions to the TWC during the drive cycle testing. A non-reactive TWC simulation is performed with kinetics to estimate the wall temperature profile of the TWC during the drive cycle testing. The simulated TWC wall temperatures are shown in Figure 49.

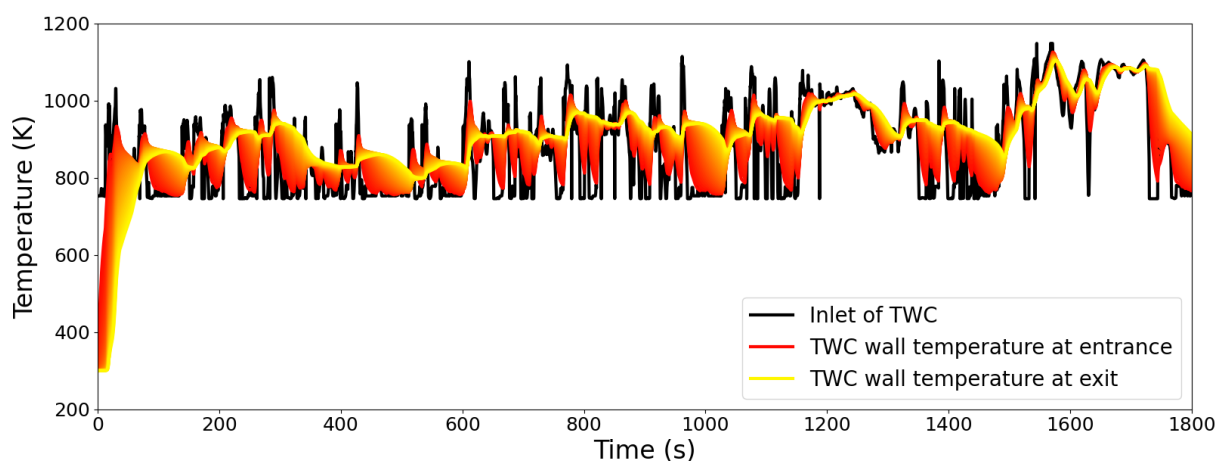


Figure 49: Simulated TWC temperature profile during drive cycle testing.

It can be observed that there is significant temperature variation along the length of the TWC. This is different to the steady-state testing simulations where the entire TWC is at the same temperature. In this case, the wall temperature of the TWC at the exit is chosen to be the input to the TWC surrogate models. Example results of the TWC surrogate models are shown in Figure 50 and Figure 51.

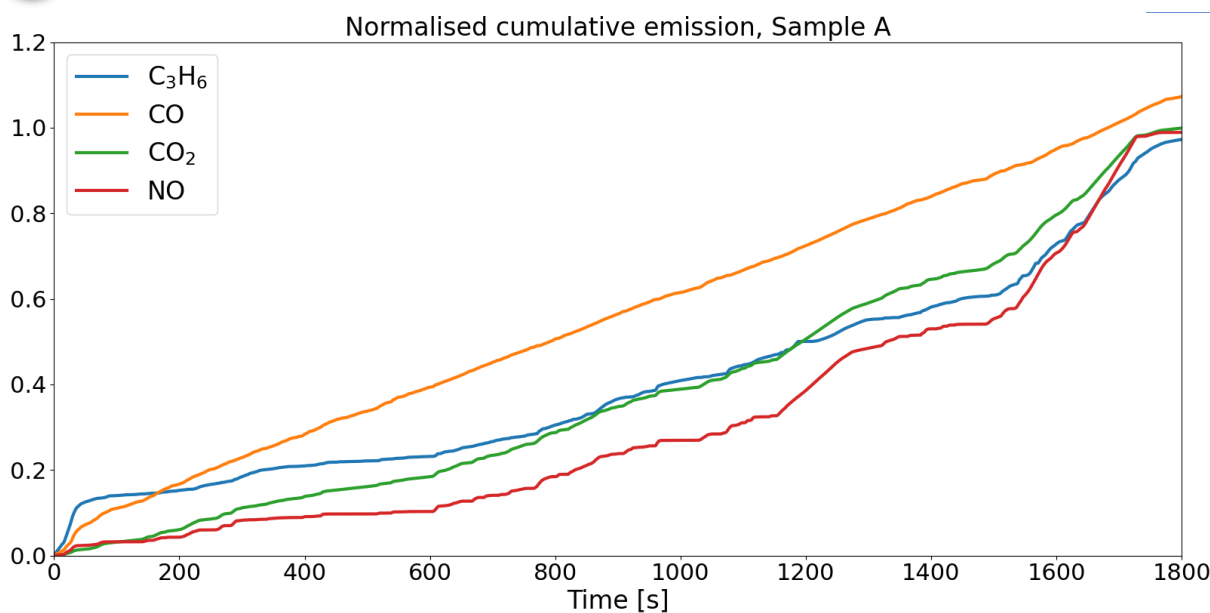


Figure 50: Cumulative emissions from TWC sample A during drive cycle test. Emissions are normalised by that of the reference catalyst.

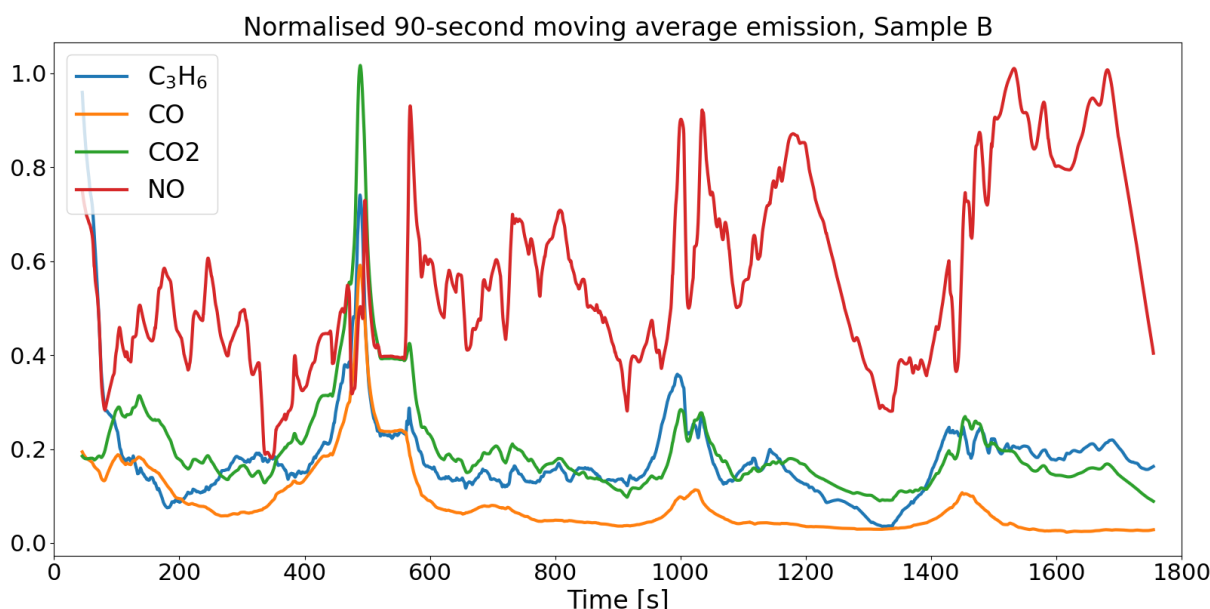


Figure 51: Smoothed “instantaneous” emissions from TWC sample B during drive cycle test. Emissions are normalised by the maximum values of “instantaneous” emission of the reference catalyst.

The overall performances of different catalyst materials are shown in Figure 52. Sample C is the only candidate that performs worse than the reference catalyst for both CO and NO emissions. Other candidates manage to out-perform the reference catalyst in at least one of the performance metric. Sample D is the only candidate that provides Pareto improvement with respect to the reference catalyst; other candidates exhibit trade-off between CO conversion and NO conversion. This is typical for TWC since complete oxidation of CO favours oxygen-rich exhaust whereas NO reduction is suppressed by high oxygen content.

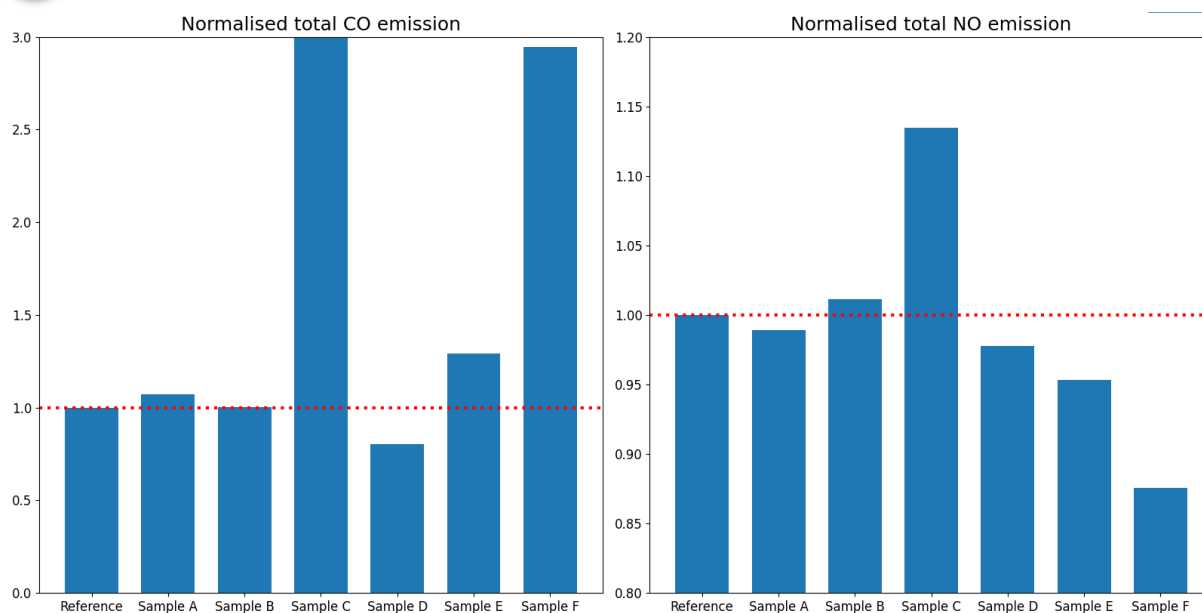


Figure 52: Total emissions from TWC samples during WLTC.

Key Performance Indicators

The workflow of digital catalyst testing can reduce the number of experiments required to be conducted, which results in **lower cost, shorter development time** and **less CO₂ emissions**. Depending on how stringent/lenient the material selection is, the saving could be between 20-80%. Furthermore, the end-to-end digital solution can create **more flexibility in design**, especially in selecting digital, physical, or combined approaches towards testing at each level of the development, leading to an increased design flexibility.

3.5.5 BENEFITS OF OIP PLATFORM

Today state-of-the-art begins with the user creating a complex workflow that combines a model of the engine with one of the catalytic converters, which predicts exhaust emissions in real driving conditions. In different stages, data on the emissions (at tailpipe, engine-out etc.) are generated based on operating conditions for a specific vehicle and engine type. The workflow generates a lot of files to analyse and data to store. There are high-fidelity models and toolkits available for different scales of the modelling. However, these exist in isolation, and in the form of bespoke simulation workflows.

Instead of managing these simulations manually (which can introduce execution errors), OpenModel offers a quick and streamlined way of completing this task: the user specifies the initial conditions (the Engine Model), a chemical space to explore (the chemical composition of the catalyst material) and sets a target (the desired emission threshold) in a semantic way (no-code approach). From this input, OntoFlow creates a high-level semantic representation of this task, which explicitly uses the basic workflow model to execute the steps above. The semantic representation is then converted into machine-executable scripts, including software parameters, input files, docker images, data schema, and so on. The data generated is analysed by the MCO, which in turn will correlate the desired output with a particular point in the chemical space investigated. The OIP facilitates such integration via introduction of easy-to-use wrappers and interfaces in an effective way while also accounting for semantics, thus enabling higher interoperability between these tools.

3.6 SUCCESS STORY [6] – FUEL CELL TECHNOLOGY (DCS, TOYOTA, HEREON)

Success Story 6 focus on the modelling of hydrogen fuel cells. Fuel cells are electrochemical cells, generating electrical energy via the redox reactions of a fuel and an oxidizer. Hydrogen fuel cells use hydrogen as fuel and oxygen from the air as the oxidizer with the reaction generating electricity, heat and water. Hydrogen flows through one side of the fuel cell and oxygen from the other. Hydrogen gets dissociated into protons and electrons in the catalyst layer. These electrons generate the electrical current between the porous media, while the protons go through a membrane to react with the oxygen, generating water and heat. This water is then expelled through the hydrophobic coating of the porous media, competing with the oxygen flow. Both hydrogen and oxygen are supplied via channels, permeating a porous gas diffusion layer on top of the catalyst. The generated water is removed through the gas diffusion layer and discarded on the oxygen channel. A schematic of this process, and the fuel cell components, is shown in Figure 53.

There are numerous potential applications for fuel cells, as they can be theoretically applied to any situation in which a battery would be suitable. Of particular interest to this use case is the application in vehicles to enable emission free transport. However, efficiency improvements are essential for fuel cells to be able to compete against established technologies, which requires a better understanding of the underlying processes. Hence the need for better models that can contribute to research and project iteration with lower cost than a purely experimental approach.

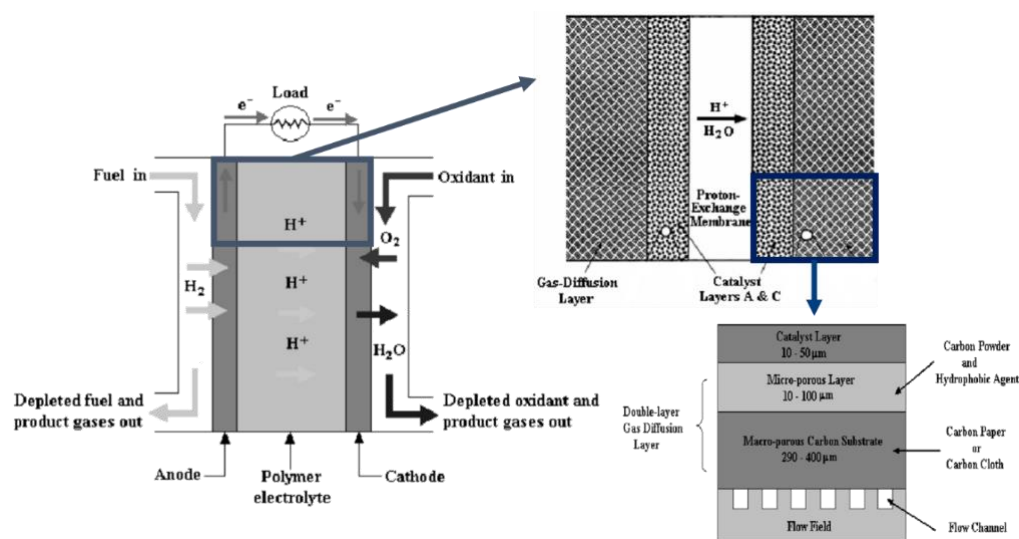


Figure 53: Schematic of a fuel cell.

Modelling a complete fuel cell is no trivial task since the responsible processes result in a multiphase flow over porous media of different sizes and characteristics. The porous media conducts heat and electricity, which in turn affect the surrounding flow. If there is enough heat, water can evaporate, requiring modelling the phase change. Moreover, the reaction between hydrogen and oxygen in the catalyst layer must be modelled as well.

Due to this complexity, it was agreed at the start of the project that modelling for the Success Story should focus on the micro-porous layer (MPL). The MPL is a layer of fine carbon powder (approximately 40-nm diameter)

with PTFE coating to make it hydrophobic. It is applied on top of the macro-porous substrate (MPS), through which oxygen is taken into the cell. Its main function is to improve water removal, but its presence and properties also affect electric current and heat exchange. Therefore, although it is physically only a small part of the fuel cell, its correct design is essential to guarantee the overall fuel cell efficiency.

The modelling objectives are set by the KPI defined for the Success Story: increased oxygen flow and water removal, increased electric conductivity and increased heat removal through the porous media. The detailed modelling approach is described in the next section.

3.6.1 MODELLING AND SIMULATION WORKFLOW FOR OFF-LINE EXECUTION

Energy generation in a fuel cell is a multiscale process involving fluid mechanics, chemical reactions, heat and electrical conduction. Even though both hydrogen and oxygen enter the fuel cell simultaneously from both ends, the process will be described in the following starting from the left side of the fuel cell in Figure 53, with the flow of hydrogen.

Hydrogen is supplied to the fuel cell via the gas flow channel, permeating the porous media which is comprised of the microporous substrate, microporous layer, and catalyst layer with length scales varying by around two orders of magnitude. In the catalyst layer (CL), hydrogen will dissociate into protons and electrons. The latter will conduct through the porous media and through a circuit to the other side (the oxygen side), while the protons will permeate through the central membrane to react with the oxygen. As with the hydrogen, oxygen is supplied to its side via gas flow channels, permeating the porous media. The reaction produces water in the catalyst layer on this side of the fuel cell, which begins filling the porous media. The MPL, sandwiched between the CL and MPS, is coated in a hydrophobic material, which helps expel the water from the porous media and through the gas flow channel. This reaction also generates heat, which needs to be conducted through the porous media in this process heating up the fluids. If the reaction is too intense and generates too much heat, it can lead to water evaporating.

To model all processes, both a discrete element method (DEM) and a computational fluid dynamics (CFD) simulation need to be performed. The former to generate the porous media which can be used to define the control volume for the CFD simulation as well as to simulate the electrical and heat conduction through the porous media. While the latter is used to simulate the fluid flow through the MPL.

The DEM, calculates the interaction between particles through a balance of the contact forces, in simple terms, essentially using Newton's laws of motion. DEM can be used to simulate large systems with numerous particles. This makes it very suitable for generating porous media through the simulation of random particle packings. The resulting particle arrangement can then be extracted and used to generate a mesh for CFD simulations, as exemplified in Figure 54.

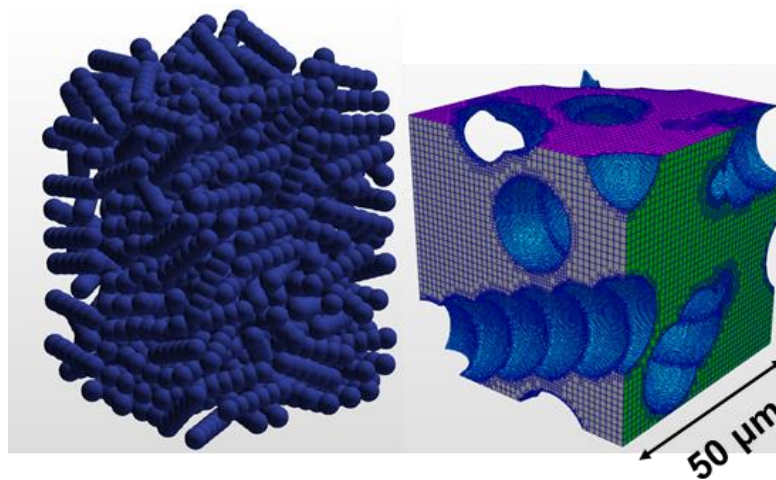


Figure 54: Example of a DEM-generated random particle packing and a CFD mesh generated from a region of the particle arrangement.

Aspherix a software developed by DCS Computing can use its DEM implementation to perform electrical conduction simulations. It calculates the contact network between particles, and determines current and electric heating when the particles are subject to a certain potential. Figure 55a shows an example of a conductivity case, where a potential was applied between the top and bottom plates enclosing the particles. The tubes in the image visualize the contact network between particles and walls. The tubes are colored by current, which shows the path of least resistance through the particle bed.

With the mesh generated for the porous media as shown in Figure 54, CFD simulations of the multiphase flow can be performed. Figure 55b shows an example of a reduced multiphase simulation. Water is entering from the left side, with air entering from the right. The shown simulation uses a Volume of Fluid method to capture the interface between liquid and gas phases, with a high contact angle between water and the porous media to simulate the hydrophobicity of the material. However, during development of the model, the industrial partner Toyota decided to focus on fuel cells operating at higher temperatures above the waters saturation temperature. Which simplifies the case to situations in which only water vapour is present. Therefore, modelling was focused on cases in which no liquid water is present and VoF is not required. This approach is discussed below.

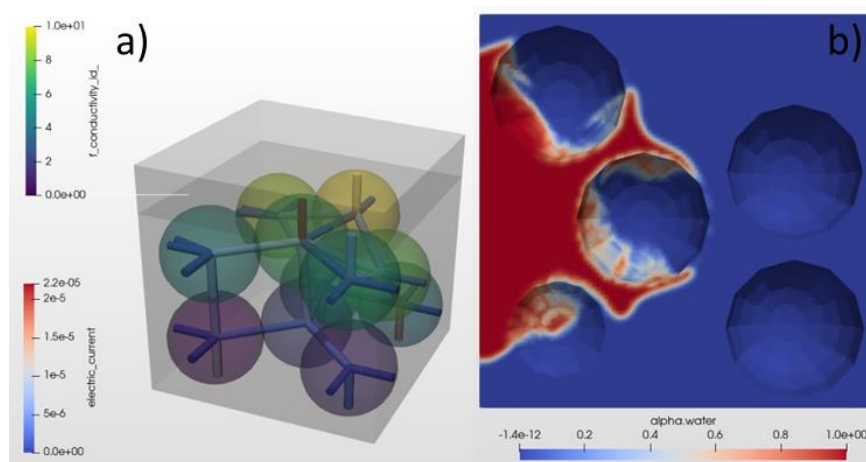


Figure 55: (a) Example of electric conductivity DEM simulation and (b) multiphase CFD simulation of water and air through porous media.

A simulation of an isolated MPL requires knowledge of the boundary conditions (BC) at the boundary between the catalyst layer (CL) and the carbon substrate (CS). The modelling choices for the fuel cell are schematically reported in Figure 56. In this project, we impose an inflow condition on the water/steam and an outflow condition for the oxygen, at the CL/MPL boundary. On the opposite side, in order to define the oxygen inlet condition at the CS/MPL boundary, we decided to simulate the oxygen flow through the gas channel and the carbon substrate, which expanded the initial scope of the modelling task to also include the CS.

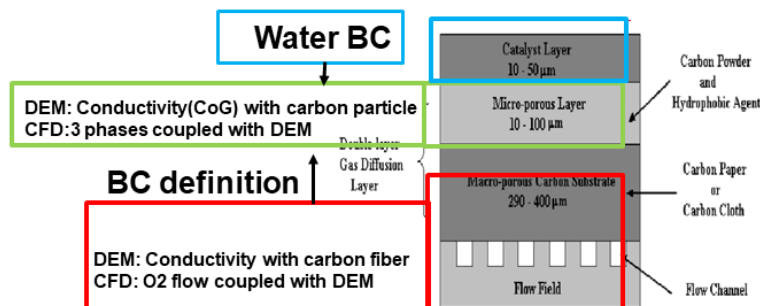


Figure 56: Fuel cell model schematic sum up.

As explained in Figure 56, the model is based on two modelling approaches: DEM and CFD. We used two different approaches for the CS and MPL.

In the gas channel/carbon substrate simulation, CFD and DEM are one-way coupled, i.e. the numerical information only flows from DEM to CFD and not vice versa. This coupling is done via a Python scripts. On the DEM side, an overall potential difference is imposed on the system (porous structure), and the resulting current heats up the particles due to the Joule effect. The particles, in turn, heat up the surrounding fluid resulting in a buoyancy force acting on the flow, which is simulated using the OpenFOAM solver bouyantPimpleFoam. Figure 57 shows an example of the resulting temperature field for both particle and fluid on the left, and the resulting velocity field on the right.

In the MPL an approach as described cannot be used due to the large number of particles and their small dimension which would require increasingly fine meshes therefore demanding an increase in the number of cells and the computational time. For this reason we decided to use a fully coupled approach, between CFD and DEM, which is the most complex form of coupling, with forces and velocities exchanged between the two simulations at every time step. In particular we used an unresolved CFD-DEM simulation, in which the CFD cells are much larger than the particles. This method unlocks the simulation of large problems with millions of particles. Fluid flow is solved on a scale that is much larger than the individual particles and information about the flow around these particles is lost. The fluid velocity is averaged in the CFD cell and the fluid forces are evenly distributed to the particles located in a cell.

Component	Simulation	Model
Microporous layer	DEM	Aspherix conductivity module
	CFD	CFDEMcoupling solver: cfdemSolverMultiphaseEuler
Gas channel	DEM	Aspherix conductivity module
+		Mesh: Aspherix + Python + OF app
Carbon substrate	CFD	Simulation: bouyantPimpleFoam

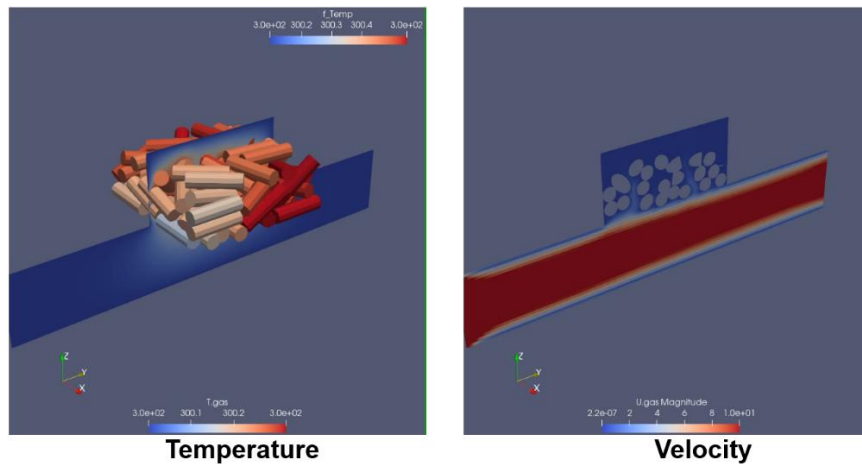


Figure 57: Gas channel and macroporous substrate simulation. Left: Temperature field for particle and fluid. Right: Velocity magnitude contours on the middle plane of the simulation domain.

Figure 58 shows results from a microporous layer simulation. In this example there is steam entering from the top part interacting with the oxygen flowing from the bottom. The top left of Figure 58 shows the steam phase fraction in red, in blue the oxygen. On the lower left we can see the fluid temperature field, on the top right we show the current flowing through the particles contact networks, and in the lower right the particles temperature.

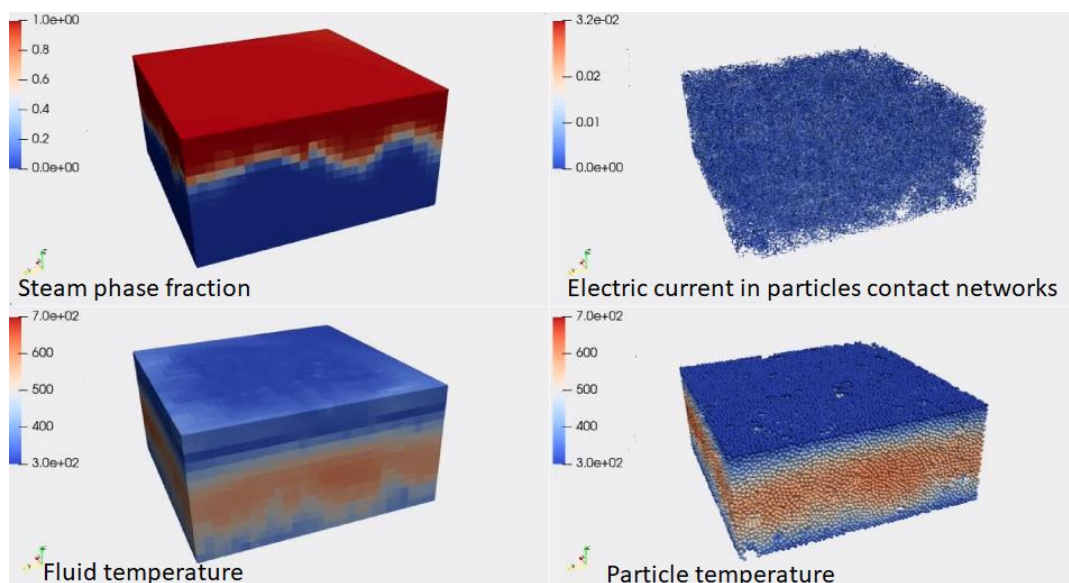


Figure 58: Microporous layer simulation.

Calibration

The fuel cell model has five parameters: electrical resistance and thermal conductivity of the particles, in both the micro- and macroporous layers, and the overall potential difference, all of which must be calibrated against experimentally measured values in order to obtain accurate simulation results.

An example of the calibration algorithm, dedicated to the electrical conductivity, is depicted in Figure 59. At first, a simplification is made, associating the complex fuel cell structure to a simple circuit with two resistances, corresponding to the two porous layers. Aspherix, together with an optimization routine, is used to find the α values (α is a dimensionless factor used to compute electrical resistance), for both layers and to compute the overall resistance of both layers, which should correspond to the overall resistivity measured in the experiment. A similar process is performed for the other two quantities thermal conductivity and potential difference.

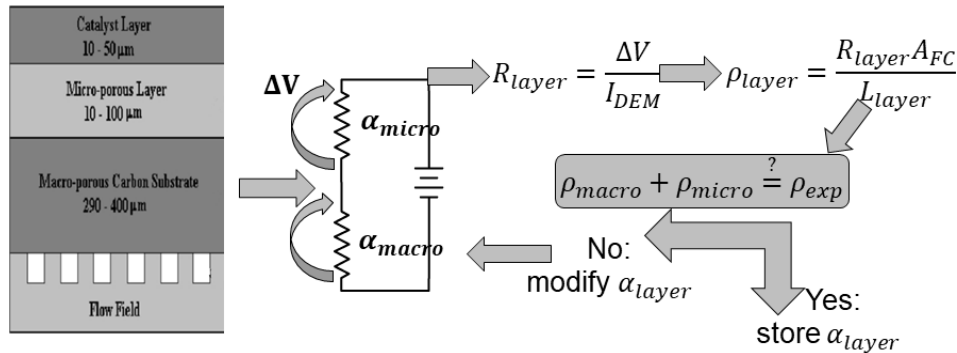


Figure 59: example of calibration of electrical conductivity.

Models Exploration

One of the questions in every simulation-related work is the tradeoff between simulation cost and precision. In parallel to the model described in the previous paragraph, we have explored two alternative solutions, which have lower computational cost but are less precise.

One possible alternative to a 3D multiphase Euler-Euler approach is a Volume of Fluid approach, which is an incompressible fluid model, with no interphase exchange and no interaction with the temperature field. It is simpler and less accurate, but on the other hand, requires fewer computational resources by solving for five equations instead of ten.

Another alternative that we have explored is the representative volume element (RVE) approach. Using this approach, instead of simulating the whole domain, which is quite computationally expensive, we use 3D simulations of smaller, representative domains and extrapolate between regions with 1D transfer functions, drastically reducing the computational cost due to the reduction of the computational domain. The downside is most geometrical information related to particle distribution is lost.

Figure 13 presents a comparison of three approaches. The left-hand side of the figure displays the simulation domain with steam, water, and oxygen inlets. The red squares indicate the positions of the RVEs with respect to the full domain, while the green rectangle represents the portion of the simulation domain used to compute average quantities, such as water phase fractions, shown on the right-hand plot. In this example, the three approaches yield similar results in the upper part of the domain (i.e., for $z > 0.3$), while the RVE approach slightly diverges from the other two approaches for $z < 0.3$. This divergence is due to the one-dimensional approximation, which reaches a steady state faster than the Euler-Euler and Volume of Fluid approaches, resulting in an overestimation of the water phase fraction in the lower part of the domain

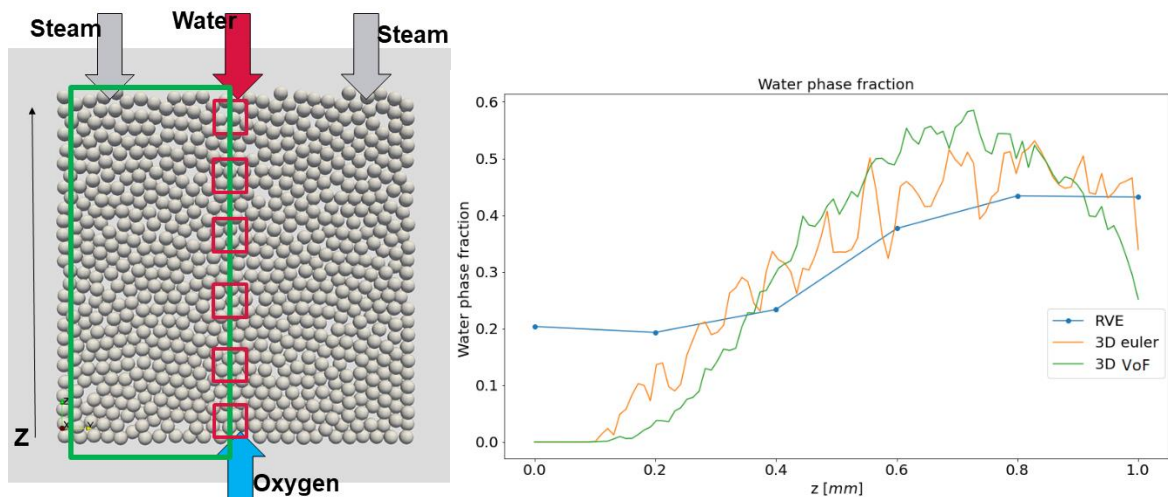


Figure 60: Comparison of the three methods. Left: Simulation domain used in the comparison. Green square: domain used to average the results. Red squares: RVE distribution along the domain.

Example of application

After careful consideration, we decided to proceed with model development using only the Euler-Euler approach. And in this section, we briefly discuss a simple case of a MPL with steam flow from the top and oxygen entering from the bottom. One of the KPIs in this Success Story is to increase the oxygen flux at the MPL/CL boundary. In this example, we compute this quantity for three cases having different microporous layer porosities. In

Figure 61, we show the structure of the MPL and the particle temperature after 0.1 s of simulation.

In Figure 62 we plot the oxygen flux at the domain upper boundary. The plotted results demonstrate that a highly porous MPL leads to a high oxygen flux at the upper boundary. This result is only an example of what is possible to achieve using the developed fuel cell model.

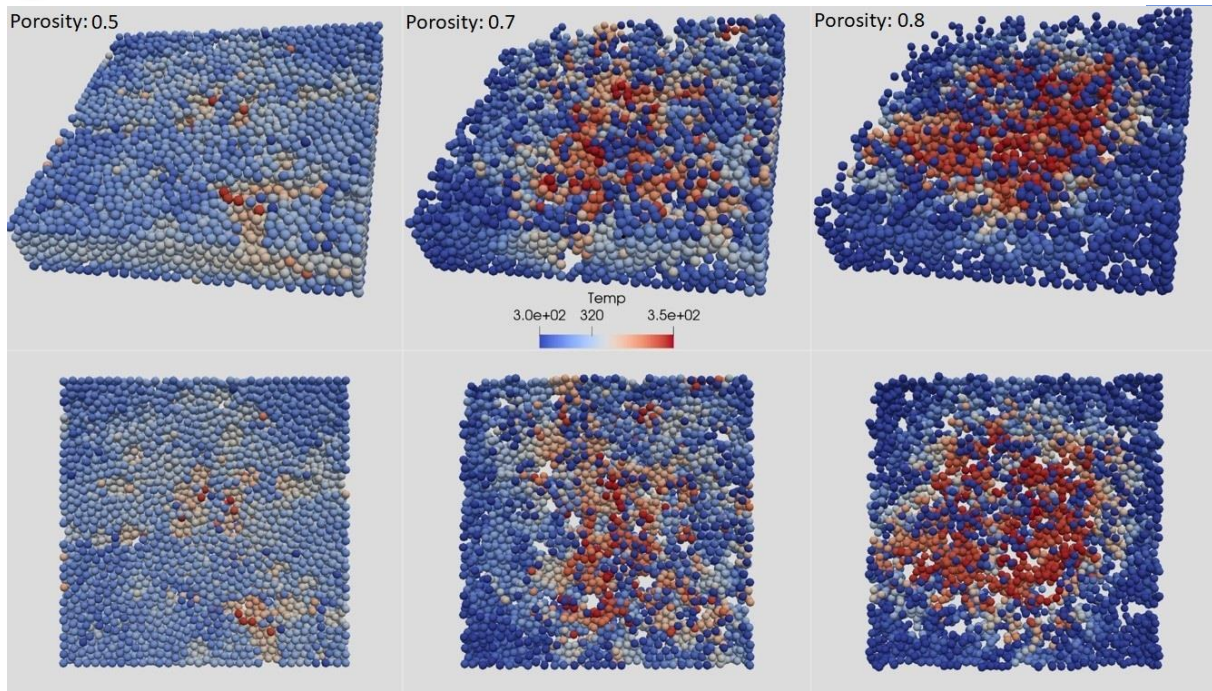


Figure 61: Example of application. Left: particle mesh with arrow indicating the inlet for steam and oxygen.

Aspherix

Aspherix is a DEM software that enables users to model the behaviour of granular materials. It offers particle modelling and contact modelling capabilities, allowing users to define particles of various shapes, sizes, and materials and simulate their interactions. Aspherix is commonly used in industries such as chemical, pharmaceutical, and food processing to model and analyse granular materials.

OpenFoam

OpenFOAM is a widely-used open-source Computational Fluid Dynamics (CFD) software package. It includes a range of solvers for modelling various fluid flow problems, such as laminar and turbulent flows, incompressible and compressible flows, and multiphase flows. OpenFOAM uses a finite volume method to discretize the governing equations, and it provides a flexible and customizable framework for users to modify or develop their own solvers and models. The software also includes a range of pre-processing and post-processing tools, including meshing tools and case set-up tools

CFDEMcoupling

CFDEMcoupling is an open-source software package that combines the Discrete Element Method (DEM) and Computational Fluid Dynamics (CFD) to model the behaviour of complex multiphase systems. It provides a flexible and customizable framework for simulating the interactions between particles and fluid flows. CFDEMcoupling uses the Aspherix for DEM and uses customized CFD solvers.

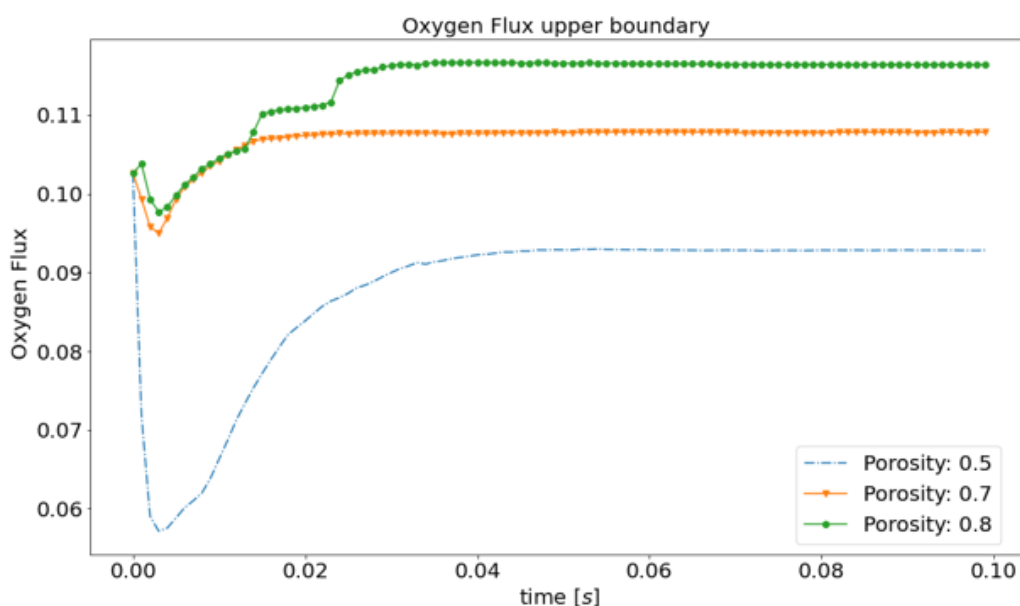


Figure 62: Comparison of oxygen flux at the upper boundary of the domain. The three cases differ for the microporous layer porosity.

3.6.2 INPUT/OUTPUT/BACKWARDS PROCESSES

Here are described the inputs and outputs for each step in the simulation, which can be found in Table 6. The DEM simulation requires the material properties and particle sizes to generate the particle bed which will comprise the porous media for the fluid flow. The full material properties are defined through an iterative calibration, as described in the previous section. The output is the structure of the porous media (defined by particle sizes and positions), the current distribution and the temperature conducted through it.

The CFD simulations uses the temperature and porous media output from DEM as input, along with the gas flow parameters for oxygen and steam. The output of interest is the outflow conditions for both gases.

The backwards process is as such: the important measure is the throughput of oxygen to the catalyst layer (oxygen outflow), as the supply of oxygen dictates the reaction rate. Oxygen flow competes with the opposing steam flow, which must also be calculated and requires the steam inflow condition. Both flow through the porous media, structured in a certain way and under a certain temperature – this is obtained from the DEM simulations. Heat is determined by the electric current flowing through the media, which is itself defined by the arrangement of particles obtained in the simulation. For this, the material properties and fuel cell current are required as input.

Table 6: Summary of input/output data for Success Story 6

	Input [IN] / Output[OUT]	Value type/ File extension	Description
Coupled CFD-DEM simulation			
OUT	Oxygen outflow	Real scalar	The oxygen throughput to the catalyst layer
	Temperature of MPL	VTM file	DEM-calculated temperature of the porous material due to electrical heating
	Electric current	VTM file	Electrical current distribution over the porous media obtained with DEM simulation
↓	To perform fuel cell fluid simulations		
IN	Operational temperature	Real scalar	Operating temperature of the fuel cell
	Oxygen massflow	Real scalar	Inlet massflow of oxygen
	Steam massflow	Real scalar	Inlet massflow of steam
	Porous media	VTM file	The porous material structure obtained from the DEM simulations and used as boundary condition for the fluid flow
DEM simulation of particle packing			
OUT	Structure of the porous media	VTM	Results of the inserted and settled particle bed containing the location and size of all spheres
↓	To perform particle packing simulations		
IN	Material properties	Real scalars	Needed material properties for DEM simulation, such as density and Young's Modulus
	Particle size	Real scalar	The radius of the spheres of the discrete material
DEM calibration of material properties			
OUT	Material electrical and thermal conductivity	Real scalars	The value for the porous media
↓	To perform the calibration		
IN	Fuel cell resistivity and current	Real scalars	The current and resistivity of the entire fuel cell

3.6.3 CHALLENGES AND GAPS ANALYSIS

The current gap in the model is it is currently incapable of properly solving the hydrophobicity of the MPL coating, meaning its usefulness in liquid water applications is limited. Improving the available models in OpenFOAM requires development effort that is outside the scope of this project and not a requirement since the industrial partner is interested in higher-temperature conditions, in which water is fully evaporated.

3.6.4 VALIDATION AGAINST EXPERIMENTAL DATA/ MEETING KPI

The model is currently not validated. It is difficult to obtain experimental results for only the MPL, with results for the entire fuel cell being more readily available. For this reason, the calibration step was developed. Besides this, the operating conditions chosen by the industrial partner are not common in literature, with temperature high enough to fully evaporate the water. The partner is currently in the process of onboarding the required software to run the case, after which a validation will be possible internally by the partner, and shared, if possible.

The main KPI under investigation with the model is the increase in throughput of oxygen to the catalyst layer, that is, the outflow of oxygen in the simulation. The available oxygen dictates the reaction rate and the generated current in the fuel cell, hence its importance. This KPI is properly addressed by the model, which can provide results for different operating conditions of the fuel cell.

3.6.5 BENEFITS OF OIP PLATFORM

The current workflow is considerably streamlined, leveraging the designed compatibility between DCS software, namely Aspherix and CFDEMcoupling, to perform the simulations. This makes it well suited, with proper wrappers, to be plugged fully into the OIP, without requiring user intervention in the intermediary steps.

The wrappers, based on the OpenModel wrapper SDK, should in the future provide a semantic interface between the software used in the workflow, allowing for ontology-based generation of the workflow, and potentially in combination with other workflows available in the platform.

4 SUMMARY AND CONCLUSIONS

An overview of the status of the workflows, main challenges/gaps identified, project execution outlook, and business outlook/deployment per Success Story is presented in *Deployment and Business Outlook* covers the deployment and business outlook for the Success Story. It includes its potential impact on the market, and any necessary steps for successful deployment

Table 7 .

Status & Workflow covers the current status of the Success Story and its workflow. It provides an overview of the progress made so far.

Main Challenges & Gaps Identified summarized the main challenges and gaps identified during the preliminary execution. It also outlines any ongoing challenges that still need to be overcome.

Project Execution Outlook focuses on the Success Story execution outlook, which includes a high level description of the upcoming tasks.

Deployment and Business Outlook covers the deployment and business outlook for the Success Story. It includes its potential impact on the market, and any necessary steps for successful deployment

Table 7 Summary of all Success Stories

	Status & Workflow	Main Challenges & Gaps Identified	Project Execution Outlook	Deployment & Business Outlook
Success Story 1 (CNR, AMAT)	Primary offline case completed – advanced solutions ongoing in line with plan.	Main challenges and gaps identified. No blocking points – green light to continue.	Test of advanced functionalities and implementation of further workflows.	Multiscale extension through inclusion of software for disorder system analysis. Time to market projected by 2028.
Success Story 2 (SISW)	Primary offline case completed – advanced solutions ongoing in line with the plan.	Main challenges and gaps identified. No blocking points – green light to continue.	R&D of wrappers ongoing, towards future Online workflows	Multiplication of the value proposition and impact of the OIP through a wider range of software deployment and services. Time to market projected by 2026
Success Story 3 (HYDRO, SINTEF, HEREON)	Not completed	Missing data for calibration and validation, missing physical properties from measurements.	Example workflow will be executable	This Success Story is part of a bigger effort on developing aluminium-reinforced concrete with possibilities to revolutionise the construction industry, by reduced use of resources and CO ₂ Footprint as well as improved corrosion

				resistance and life-time.
Success Story 4 (HEREON)	Offline case completed and published. Working on extension outside of the scope of this project.	More experimental data – in progress.	Integration is straight forward no special wrapper needed.	Will be deployed as part of Helmholtz Metadata project.
Success Story 5 (CMCL)	Not completed	Missing data for calibration and validation, missing physical properties from measurements.	Example workflow will be executable	The end-to-end digital solution for catalytic powder testing offers a streamlined, cost-effective approach for automotive OEMs, and upon completion of the project, this exploitation route could be pursued further. Execution of the Success Story on OpenModel platform also helps further uptake of CMCL toolkits and further reach to potential users.
Success Story 6 (DCS, TOYOTA, HEREON)	Offline case completed; full workflow can be run with AiiDa plugin	Validation remains a challenge as experimental data for the MPL is hard to source.	Wrappers will be developed for the workflow based on the AiiDa plugin.	While process IP for electrode design vests in the industrial partner (Toyota), models (e.g. for electrical conductivity paths, gas diffusion) are transferable to other application such as modelling of battery components or catalytic processes which require modelling of gas diffusion. Results will be exploited via the

				product suite of DCS (Aspherix and CFDEMcoupling)
--	--	--	--	---

5 DISSEMINATION

A list of complete dissemination activities and a plan for future dissemination per Success Story is summarized in Table 8

Table 8 Summary of dissemination activities

	Dissemination
Success Story 1 (CNR, AMAT)	<p>Publications</p> <ul style="list-style-type: none"> Slassi, L.-S. Medondjio, A. Padovani, F. Tavanti, X. He, S. Clima, D. Garbin, B. Kaczer, L. Larcher, P. Ordejón, and A. Calzolari, "Device-to-materials pathway for electron traps detection in amorphous GeSe-based selectors", <i>Adv. Electr. Mater. Adv. Electr. Mater.</i> 2201224 (2023). F. Tavanti and A. Calzolari, "A multi-technique approach to unravel the (dis)order in amorphous materials", <i>ACS Omega</i> 7, 23255 (2022). <p>Oral presentations</p> <ul style="list-style-type: none"> A. Calzolari, "Plasmonic by design" at SPIE Photonic West, San Francisco CA, USA. Feb 28th- March 3rd 2023. A. Calzolari, "The role of disorder on the structural-electronic interplay in amorphous GeSe: a microscopic investigation" at CIMTEC22, 9th forum on new materials Session FH F - 4th International Conference Emerging Materials, Technologies and Applications for Non-volatile Memory and Memristive Devices. 25-29 June 2022. A. Calzolari, "The role of disorder on the structural-electronic interplay in amorphous GeSe: a microscopic investigation" at "MUSICODE summer school on Multiscale Modelling and Open Innovation Platforms" (14-22 July 2022). <p>Poster presentations</p> <ul style="list-style-type: none"> F. Tavanti "Understanding the structure of amorphous chalcogenides for improving their electrical performances" at 21st International Workshop on Computational Physics and Materials Science: Total Energy and Force Methods, Trieste IT 11-13 Jan 2023. L. Bursi "First principles characterization of defect states in emerging materials for next-generation technology" at 21st International Workshop on Computational Physics and Materials Science: Total Energy and Force Methods, Trieste IT 11-13 Jan 2023. A. Calzolari "Plasmonic by design" at 21st International Workshop on Computational Physics and Materials Science: Total Energy and Force Methods, Trieste IT 11-13 Jan 2023.

	<ul style="list-style-type: none"> A. Slassi “Theoretical characterization of the trap states in quasi-stoichiometric amorphous GexSe(1-x)-based chalcogenides with different chemical doping” at 21st International Workshop on Computational Physics and Materials Science: Total Energy and Force Methods, Trieste IT 11-13 Jan 2023.
Success Story 2 (SISW)	<ul style="list-style-type: none"> Stijn Donders, presentation at 3rd EMMC International Workshop 2021, 02-04 March 2021. <p>Planned dissemination:</p> <ul style="list-style-type: none"> E. Marques. Experimental modal analysis of a composite B-Pillar car component measured with optical techniques. Planned presentation at the conference “<i>Measuring by light. International meeting on optical measurement techniques and industrial applications</i>”. Delft, Netherlands, 28-30 March 2023; https://measuringbylight.com/ Master Thesis. Effect of curing on the part performance of a composite B-Pillar. Joao Viera, Instituto Superior Tecnico, 2023. Ongoing Master Thesis. Experimental and numerical modal analysis of a composite B-Pillar. Eduardo Marques, Instituto Superior Tecnico, 2023. Ongoing
Success Story 3 (HYDRO, SINTEF, HEREON)	<ul style="list-style-type: none"> S. Berger et al., Simulation workflows for enhanced corrosion prediction and protection Advanced modelling-based surface engineering against materials degradation and damage, Virtual Materials Design, 2021 S. Berger et al., Simulation workflow for the optimization of protective interface layer formation in novel aluminium reinforced concrete, EuroCorr, 2022 S. Berger et al., Simulation workflow for the optimization of protective interface layer formation in novel aluminium reinforced concrete, Materials Science and Engineering Conference, 2022 S. Berger et al., Hereon’s activities in OpenModel, Material Systems Engineering Conference, 2022
Success Story 4 (HEREON)	<ul style="list-style-type: none"> S. Berger et al., Hereon’s activities in OpenModel, Material Systems Engineering Conference, 2022 <p>Submitted:</p> <ul style="list-style-type: none"> B. Wiese, S. Berger et al., Property prediction by machine learning on extruded magnesium-gadolinium alloys, Magnesium and Alloys Journal, 2023 <p>Planned:</p> <ul style="list-style-type: none"> B. Wiese, S. Berger et al., Machine-learning for property prediction of extruded Magnesium alloys, Magnesium and Alloys Journal, 2024
Success Story 5 (CMCL)	<ul style="list-style-type: none"> Y. R. Tan, Q. Zhu, Y. Zong, J. Lai, M. Salamanca, J. Akroyd, W. Yang, and M. Kraft, “The influence of alcohol, carbonate and polyethers as oxygenated

	fuels on the soot characteristics from a CI engine,” <i>Fuel</i> , vol. 338, p. 127296, 2023.[20]
Success Story 6 (DCS, TOYOTA, HEREON)	<ul style="list-style-type: none"> S. Berger et al., Hereon’s activities in OpenModel, Material Systems Engineering Conference, 2022 Planned: <ul style="list-style-type: none"> A. Moura, S. Berger et al., Model for the optimization of MPL, <i>Journal</i>, 2024

6 BIBLIOGRAPHY

- [1] “Closing the loop on composites. Using the digital twin to virtually predict and optimize product performance.,” *Siemens Digital Industries Software*, 2019.
- [2] “Siemens Digital Industries Software Simcenter 3D product webpage. <https://plm.sw.siemens.com/en-US/simcenter/mechanical-simulation/3d-simulation/>.” .
- [3] “Siemens Simcenter 3D Materials Engineering product webpage. <https://www.plm.automation.siemens.com/global/en/products/simulation-test/materials-engineering.html>.” .
- [4] “Structural analysis using Simcenter 3D Laminate Composites,” *Siemens Digital Industries Software Tutorial*.
- [5] “Simcenter Samcef product page. https://docs.plm.automation.siemens.com/data_services/resources/nx/1899/nx_help/custom/en_US/samcef_solver_documentation/m001/gets-gen-m001.html.” .
- [6] “Siemens Simcenter HEEDS product webpage. <https://plm.sw.siemens.com/en-US/simcenter/integration-solutions/heeds/>.” .
- [7] “Siemens Digital Industries Software Simcenter STAR-CCM+ product webpage. <https://plm.sw.siemens.com/en-US/simcenter/fluids-thermal-simulation/star-ccm/>.” .
- [8] C. Holt, “Achieving lighter vehicles with the use of composites,” *Simcenter blog*, <https://blogs.sw.siemens.com/simcenter/Achieving-lighter-vehicles-with-the-use-of-composites/>, 2019.
- [9] O. Shishkina, M. Wevers, S. V. Lomov, and F. L, “Simcenter 3D Virtual Material Characterization ToolKit for realistic composite materials modeling using micro-CT-based voxel approach,” *Image-Based Finite Element Method for Industry (IBFEM-4i)*, Swansea, UK, 2019.
- [10] C. Demaría, E. Ruiz, and F. Trochu, “In-plane anisotropic permeability characterization of deformed woven fabrics by unidirectional injection. Part II: Prediction model and numerical simulations,” *Polymer Composites*, vol. 28, no. 6, pp. 812–827, 2007.
- [11] “Simcenter Testlab Software product webpage. <https://plm.sw.siemens.com/en-US/simcenter/physical-testing/testlab/>.” .

- [12] F. Shishkina; Martine Wevers; Stepan V. Lomov; Laszlo Oxana, “Micro-CT-based numerical validation of the local permeability map for the B-Pillar infusion simulation,” in *Composites Meet Sustainability – Proceedings of the 20th European Conference on Composite Materials, ECCM20. 26-30 June, 2022, Lausanne, Switzerland*.
- [13] H. Justnes. et al, “Aluminium Reinforced Concrete Enabled by Calcined Clay,” *Proceedings of fib International Congress, 2022*.
- [14] H. Justnes and T. Danner, “Microstructure of Cement/Clay paste with Aluminum bar after 1 year storage in Fresh Water and in 6% NaCl,” *ACI Symposium Publication*, vol. 355, pp. 151–164, 2021.
- [15] O. R. Myhr and Ø. Grong, “Modelling of non-isothermal transformations in alloys containing a particle distribution,” *Acta mater*, vol. 48, pp. 1605–1615, 2000.
- [16] O. R. Myhr, Ø. Grong, and K. O. Pedersen, “A Combined Precipitation, Yield Strength, and Work Hardening Model for Al-Mg-Si Alloys,” *Metallurgical and Materials Transactions A*, vol. 41, pp. 2276–2289, 2010.
- [17] O. R. Myhr, Ø. Grong, and C. Schäfer, “An extended age-hardening model for Al-Mg-Si alloys incorporating the room-temperature storage and cold deformation process stages,” *Metallurgical and Materials Transactions A*, vol. 46, pp. 6018–6039, 2015.
- [18] D. Chatterjee, O. Deutschmann, and J. Warnatz, “Detailed surface reaction mechanism in a three-way catalyst,” *Faraday Discuss.*, vol. 119, no. 0, pp. 371–384, 2002.
- [19] T. Wang, Y. Zhang, J. Zhang, G. Shu, and Z. Peng, “Analysis of recoverable exhaust energy from a light-duty gasoline engine,” *Applied Thermal Engineering*, vol. 53, no. 2, pp. 414–419, 2013.
- [20] Y. R. Tan, Q. Zhu, Y. Zong, J. Lai, M. Salamanca, J. Akroyd, W. Yang, and M. Kraft, “The influence of alcohol, carbonate and polyethers as oxygenated fuels on the soot characteristics from a CI engine,” *Fuel*, vol. 338, p. 127296, 2023.

7 ACKNOWLEDGMENT



This project has received funding from the European Union's Horizon 2020 research and innovation programme under grant agreement No 953167.

This document and all information contained herein is the sole property of the OpenModel Consortium. It may contain information subject to intellectual property rights. No intellectual property rights are granted by the delivery of this document or the disclosure of its content.

Reproduction or circulation of this document to any third party is prohibited without the consent of the author(s).

The content of this document does not reflect the official opinion of the European Union. Responsibility for the information and views expressed herein lies entirely with the author(s).

All rights reserved.